Combustion Efficiency, Flameout Operability Limits and General Design Optimization for Integrated Ramjet-Scramjet Hypersonic Vehicles

by

Chukwuka Chijindu Mbagwu

A dissertation submitted in partial fulfillment
of the requirements for the degree of
Doctor of Philosophy
(Aerospace Engineering)
in The University of Michigan
2017

Doctoral Committee:

Professor James F. Driscoll, Chair
Assistant Professor Eric Johnsen
Professor Joaquim R. R. A. Martins
Professor Venkat Raman

Chukwuka C. Mbagwu

cmbagwu@umich.edu

ORCID iD: 0000-0003-3025-9307

© Chukwuka C. Mbagwu 2017

All Rights Reserved

For my parents,

their unwavering love and support is the ground upon which these efforts rest.

TABLE OF CONTENTS

DEDICATION ii

LIST OF FIGURES v

LIST OF TABLES x

LIST OF APPENDICES xi

ABSTRACT xii

CHAPTER

I. Introduction and MASIV Overview 1

1.1 The MASIV Model and the MAX-1 Waverider 3

II. Methods and Application for Flamelet Table Reduction . . . 7

2.1 Introduction 7
2.2 Artificial Neural Network 8
2.2.1 Training 9
2.2.2 Network Topology: Trade Study 10
2.2.3 Results of the Artificial Neural Network Interpolation 12
2.3 The Proper Orthogonal Decomposition 14
2.3.1 POD On Flamelet Chemistry Data 16
2.3.2 Additional Input Dimensions to the POD Approximation 19
2.3.3 Accuracy of the POD Interpolation and Conclusion 21

III. Combustion Efficiency and Flameout Limits from Empirical Damköhler Numbers 23

3.1 Introduction 23
3.2 Defining the Operability Limits 26

3.2.1 The jet spreading and mixing model for N jets in a crossflow . . . 29
3.3 New Additions to the MASIV model to Improve the Finite-Rate Chemistry . . . 33
3.4 Results . . . 39
3.4.1 Assessment Case: Parameters Varied Independently 39
3.4.2 Ascent Case: Combustor Flow Conditions . . . 43
3.4.3 Ascent Case: Combustion Efficiency and Flameout Limit . . . 47
3.4.4 Ascent Case: Operability Limits on a Flight Corridor Map . . . 49
3.5 Discussion of Uncertainty . . . 50
3.6 Conclusions . . . 53

IV. Design Optimization Approach to Waverider Vehicles . . . 55

4.1 Introduction . . . 55
4.2 Background: Importance of L/D and T/D for Waveriders . . . 58
4.3 Previous Propulsion-Oriented Design Rules . . . 64
4.4 Development of Vehicle-Integration Design Rules . . . 68
4.4.1 The 84 Waverider Geometries Considered . . . 69
4.4.2 Computed Effects of Geometry on L/D and T/D During Cruise . . . 72
4.4.3 Effects of Acceleration on L/D and T/D . . . 80
4.4.4 Extension to Trajectory Operating Maps . . . 85
4.4.5 Specific Impulse and T/D for Hypersonic Vehicles . 90
4.5 Trajectory Optimization for Total Fuel Usage and T/D . . . 92
4.5.1 Minimizing Fuel Usage, m_f . . . 93
4.5.2 Maximizing Thrust-to-Drag Ratio, T/D . . . 97
4.6 Conclusions . . . 101

V. Conclusions and Future Work . . . 105

APPENDICES . . . 108

BIBLIOGRAPHY . . . 131

LIST OF FIGURES

Figure

1.1 Shock and temperature (Kelvin) contours of the MAX-1 vehicle trimmed at Mach 8, computed in reference [1]. 3
1.2 Dual-mode ramjet-scramjet internal flow path of the MAX-1 waverider. 4
2.1 Schematic of a neuron, i. 8
2.2 Optimized Artificial Neural Network Topology, Γ. 10
2.3 Objective (Cost) Function and Reaction Rate Percent Error for Various Topologies. 11
2.4 Reaction Rate Percent Error Map of Optimal ANN Approximation (3-D function). 12
2.5 Reaction Rates given by (a) the 3-D lookup table and (b) neural network approximation. 13
2.6 Contours of Reaction Rate for H2O at p = 2.61 bar, T = 1280 K, and $\chi = 312.3$ [1/s]. 18
2.7 Contours of Reaction Rate Error for H2O at p = 2.61 bar, T = 1280 K, and $\chi = 312.3$ [1/s]. 19
3.1 The MAX-1 hypersonic waverider vehicle. Engine width is 2.143 m. For details, see references [2, 3]. 24
3.2 Schematic of the flight corridor map with three possible ascent trajectories of constant dynamic pressure. Unstart limit and ram-scram transition curves were previously computed in reference [1]. The following sections describe how the low and high ambient pressure limits depend on combustion efficiency and flameout. 25
3.3 Atmospheric conditions for pressure p_∞ (blue, left) and temperature T_∞ (red, right) as a function of altitude. 25
3.4 Detailed schematics of the spreading profile for a jet in crossflow by (a) Hasselbrink [4] and (b) Torrez [3]. 30
3.5 Schematic of three of the N = 19 fuel ports that are located across the span of the combustor; above each port is a fuel jet in an air crossflow. Also marked is the height (H) of the flame holder cavity. 34

3.6 (a) 2-D slices of the 3-D contours of hydrogen reaction rates within one of the fuel jets sketched in Figure 3.5, at two pressure conditions. (b) The 1-D profiles of volumetric hydrogen reaction rate ($\overline{\dot{\omega}_{H2}}$) determined by integrating the contours in (a).i or (a).ii over the y-z plane. Fuel port is at x = 16.4 m. T3 = 900 K, U3 = 2,000 m/s, ER = 0.30. 35
3.7 (a) Contours of hydrogen reaction rate ($\bar{\omega}_{H2}/\rho$) computed by the FLAMEMASTER code and stored in the matrix **S**, for one flamelet that corresponds to dissipation rate $\chi = 882\ \mathrm{s}^{-1}$ and $p_3 = 3.16$ bar, T_3 = 1300 K. (b) Truncation error of the POD approximation, showing errors of less than 1% by keeping only the four largest POD modes. 40
3.8 Assessment case, no ascent: hydrogen mass fraction profiles for different combustor entrance pressures p_3. $T_3 = 900$ K, $U_3 = 2{,}000$ m/s, $ER = 0.3$. 41
3.9 Assessment case, no ascent: combustion efficiencies for (a) $ER = 0.3$ and (b) $ER = 0.9$. $U_3 = 2{,}000$ m/s. 42
3.10 Assessment case, no ascent: flameout occurs below the horizontal line $Da_H = 1$, as defined by equation 3.2. (a) $ER = 0.30$ and (b) $ER = 0.90$. Mach number $M_3 = 2$. 44
3.11 Ascent case: for a dynamic pressure (a) combustor entrance static pressure p_3, (b) static temperature T_3, (c) air velocity U_3, and (d) combustor Mach number M_3 versus flight Mach number M_∞. . . . 45
3.12 Ascent Case: fuel-air equivalence ratio ER versus flight Mach number, for different trajectories of constant dynamic pressure q_∞. . . . 46
3.13 Ascent Case: combustion efficiency versus flight Mach number, for different trajectories of constant dynamic pressure q_∞. 47
3.14 Damköhler number computed by MASIV as the MAX-1 vehicle ascends and accelerates along each of the ascent trajectories plotted in Figure 3.2. Dynamic pressure $q_\infty = 30$ kPa is the highest altitude trajectory, while $q_\infty = 300$ kPa is the lowest altitude trajectory. Cavity height varies from (a) H = 0.0058 m and (b) H = 0.0120 m. 48
3.15 Operability limits due to Flameout (thick curved, red lines) and combustion efficiency exceeding 0.90 (solid, blue line). Cavity flameholder height H is: (a) 0.0058 m and (b) 0.0120 m. The thin solid lines are ascent trajectories of constant q_∞. Vehicle acceleration = 2 m/s^2. . 50
4.1 Close integration of vehicle components is required for hypersonic lifting body configurations. 57
4.2 Variation of $C_{D,0}$ and $(L/D)_{\max}$ with Mach number for three variants of a NASA Hypersonic Research Aircraft concept, from [5]. 60
4.3 Increased Lift-to-Drag ratio provided by a waverider geometry (upper curve) compared to conventional configurations (lower curve), as Mach number is increased [6]. 61
4.4 Trend in maximum lift-to-drag ratio with one measure of configuration fineness ratio, found in [7]. 63

4.5 (a) Bow shock intersecting engine lip at maximum flight Mach number M^*. (b) Lower speed operation with air spillage. 65
4.6 (a) Reference MAX-1 vehicle and flow path dimensions. Engine width is 2.143 m. (b) Schematic top-view of the independent variable vehicle parameters examined. 69
4.7 Altitude-Mach number plot of various constant-q ascent trajectories. Circle indicates the location of the 3 studied flight conditions. . . . 70
4.8 (a) Azimuthal and top views of the waverider Design 3 "airplane-like", with $b/b_{ref} = 1$ and $c/c_{ref} = 3$ and $W_e/W_{e,ref} = 1$. 71
4.9 (a) Azimuthal and top views of the waverider Design 7 "rocket-like", with $b/b_{ref} = 0.5$ and $c/c_{ref} = 1$ and $W_e/W_{e,ref} = 1$. 73
4.10 Cruise case ($\mathbf{a} = 0$): L/D ratio for a trimmed MAX-1 waverider at Mach 8 and 26 km altitude computed using MASIV. Effect of varying root chord (c), aspect ratio (b/c), engine width (W_e). 74
4.11 Cruise case ($\mathbf{a} = 0$): Angle of attack α for a trimmed MAX-1 waverider at Mach 8 and 26 km altitude computed using MASIV. Effect of varying root chord (c), aspect ratio (b/c), engine width (W_e). . . 76
4.12 Cruise case ($\mathbf{a} = 0$): Elevon deflection δ for a trimmed MAX-1 waverider at Mach 8 and 26 km altitude computed using MASIV. Effect of varying root chord (c), aspect ratio (b/c), engine width (W_e). . . 77
4.13 Cruise case ($\mathbf{a} = 0$): Equivalence ratio ϕ for a trimmed MAX-1 waverider at Mach 8 and 26 km altitude computed using MASIV. Effect of varying root chord (c), aspect ratio (b/c), engine width (W_e). . . 79
4.14 Accelerating case ($\mathbf{a} = 2$): L/D ratio for a trimmed MAX-1 waverider at Mach 8 and $q_\infty = 90$ kPa computed using MASIV. Effect of varying root chord (c), aspect ratio (b/c), engine width (W_e). 81
4.15 Accelerating case ($\mathbf{a} = 2$): T/D ratio for a trimmed MAX-1 waverider at Mach 8 and $q_\infty = 90$ kPa computed using MASIV. Effect of varying root chord (c), aspect ratio (b/c), engine width (W_e). 82
4.16 Accelerating case ($\mathbf{a} = 2$): Equivalence ratio ϕ for a trimmed MAX-1 waverider at Mach 8 and $q_\infty = 90$ kPa computed using MASIV. Effect of varying root chord (c), aspect ratio (b/c), engine width (W_e). 84
4.17 Ascent trajectory and MAX-1 vehicle geometry; showing (a) T/D ratio, (b) L/D ratio, (c) equivalence ratio ϕ, (d) elevon deflection angle δ. (Ascent is for constant dynamic pressure of 90 kPa and accelerations from zero to 8 m/s^2). 86
4.18 Ascent trajectory map of L/D ratio for constant q_∞ of 90 kPa; showing the (a) "rocket-like" limit, (b) "airplane-like" limit. Accelerations range from zero to 8 m/s^2. 87
4.19 Ascent trajectory map of equivalence ratio ϕ for constant q_∞ of 90 kPa; showing the (a) "rocket-like" limit, (b) "airplane-like" limit. Accelerations range from zero to 8 m/s^2. 88
4.20 Ascent trajectory map of angle of attack α for constant q_∞ of 90 kPa; showing the (a) "rocket-like" limit, (b) "airplane-like" limit. Accelerations range from zero to 8 m/s^2. 89

4.21 Ascent trajectory map of T/D ratio and $I_{sp,\text{eff}}$ for constant q_∞ of 90 kPa; showing the (a),(c) "rocket-like" limit, and (b),(d) "airplane-like" limit. Accelerations range from zero to 8 m/s^2. 91
4.22 Similar starting intervals result in different solutions using GSS on an arbitrary function. 96
4.23 Minimum-fuel ascent trajectories for MAX-1, GSS (black) and FMINCON (red) optimizations compared. Two initial fuel fractions (d). Showing trajectories for (a) $q_\infty = 70$ kPa, $d = 1.0$, (b) $q_\infty = 70$ kPa, $d = 0.5$, (c) $q_\infty = 100$ kPa, $d = 1.0$, (d) $q_\infty = 100$ kPa, $d = 0.5$, (e) $q_\infty = 140$ kPa, $d = 1.0$, and (f) $q_\infty = 140$ kPa, $d = 0.5$. 98
4.24 Computed metrics for the minimum-fuel ascent trajectories for MAX-1. Blue plots correspond to the Left axis, and Red plots to the Right. Solid lines are for initial fuel fraction $d = 1.0$, dashed lines for $d = 0.5$. (a), (b), and (c) represent constant dynamic pressure trajectories for $q_\infty = 70$ kPa; (d), (e), and (f) for $q_\infty = 100$ kPa; (g), (h), and (i) for $q_\infty = 140$ kPa. Computed metrics include T/D, L/D, angle of attack α, elevon deflection δ, equivalence ratio ϕ, and combustion efficiency η_C. 99
4.25 Damkohler number and Flameout limits computed along four minimum-fuel ascent trajectories. The MAX-1 waverider is used, and all vehicles start with full tanks ($d = 1.0$). Flameout regions along the ascent path are marked with an 'x'. (a) Dynamic pressure of $q_\infty = 70$ kPa, cavity step height $H = 0.012$ m, (b) $q_\infty = 70$ kPa, $H = 0.014$ m, (c) $q_\infty = 100$ kPa, $H = 0.0095$ m, and (d) $q_\infty = 100$ kPa, $H = 0.012$ m. 100
4.26 Maximum T/D (black) and minimum-fuel (red) ascent trajectories for MAX-1, superimposed. Two initial fuel fractions (d). Showing trajectories for (a) $q_\infty = 70$ kPa, $d = 1.0$, (b) $q_\infty = 70$ kPa, $d = 0.5$, (c) $q_\infty = 100$ kPa, $d = 1.0$, (d) $q_\infty = 100$ kPa, $d = 0.5$, (e) $q_\infty = 140$ kPa, $d = 1.0$, and (f) $q_\infty = 140$ kPa, $d = 0.5$. 102
4.27 Computed metrics for the maximum T/D (solid lines) and the minimum-fuel (dashed lines) ascent trajectories for MAX-1. Blue plots correspond to the Left axis, and Red plots to the Right. All trajectories are plotted for an initial fuel fraction $d = 1.0$. (a), (b), and (c) represent constant dynamic pressure trajectories for $q_\infty = 70$ kPa; (d), (e), and (f) for $q_\infty = 100$ kPa; (g), (h), and (i) for $q_\infty = 140$ kPa. Computed metrics include T/D, L/D, angle of attack α, elevon deflection δ, equivalence ratio ϕ, and combustion efficiency η_C. 103
B.1 Resultant forces *along the engine flowpath* for $M_\infty = 7$, $h = 26km$, $ER = 0.5$. Forces are in the body axes, such that Thrust points to $-$x-direction. 113
B.2 Thrust, drag, lift and gravitational forces for the case of a horizontal flight path that is parallel to the relative wind and no engine cant. . 115

C.1 Accelerating case ($\mathbf{a} = 1$): L/D ratio for a trimmed MAX-1 waverider at Mach 8 and $q_\infty = 90$ kPa computed using MASIV. Effect of varying root chord (c), aspect ratio (b/c), engine width (W_e). 117
C.2 Accelerating case ($\mathbf{a} = 1$): T/D ratio for a trimmed MAX-1 waverider at Mach 8 and $q_\infty = 90$ kPa computed using MASIV. Effect of varying root chord (c), aspect ratio (b/c), engine width (W_e). 118
C.3 Accelerating case ($\mathbf{a} = 1$): Equivalence ratio ϕ for a trimmed MAX-1 waverider at Mach 8 and $q_\infty = 90$ kPa computed using MASIV. Effect of varying root chord (c), aspect ratio (b/c), engine width (W_e). 119
C.4 Accelerating case ($\mathbf{a} = 1$): Angle of attack α for a trimmed MAX-1 waverider at Mach 8 and $q_\infty = 90$ kPa computed using MASIV. Effect of varying root chord (c), aspect ratio (b/c), engine width (W_e). 120
C.5 Accelerating case ($\mathbf{a} = 1$): Elevon deflection δ for a trimmed MAX-1 waverider at Mach 8 and $q_\infty = 90$ kPa computed using MASIV. Effect of varying root chord (c), aspect ratio (b/c), engine width (W_e). 121
C.6 Cruise case ($\mathbf{a} = 0$): T/D ratio for a trimmed MAX-1 waverider at Mach 8 and 26 km altitude computed using MASIV. Effect of varying root chord (c), aspect ratio (b/c), engine width (W_e). 123
C.7 Accelerating case ($\mathbf{a} = 2$): Angle of attack α for a trimmed MAX-1 waverider at Mach 8 and $q_\infty = 90$ kPa computed using MASIV. Effect of varying root chord (c), aspect ratio (b/c), engine width (W_e). 125
C.8 Accelerating case ($\mathbf{a} = 2$): Elevon deflection δ for a trimmed MAX-1 waverider at Mach 8 and $q_\infty = 90$ kPa computed using MASIV. Effect of varying root chord (c), aspect ratio (b/c), engine width (W_e). 126
D.1 Ascent trajectory and MAX-1 vehicle geometry; showing (a) T/D ratio, (b) L/D ratio, (c) angle of attack α, (d) elevon deflection angle δ, and (e) equivalence ratio ϕ. (Ascent is for constant dynamic pressure of 70 kPa and accelerations from zero to 8 m/s^2). 128
D.2 Ascent trajectory and MAX-1 vehicle geometry; showing (a) T/D ratio, (b) L/D ratio, (c) angle of attack α, (d) elevon deflection angle δ, and (e) equivalence ratio ϕ. (Ascent is for constant dynamic pressure of 100 kPa and accelerations from zero to 8 m/s^2). 129
D.3 Ascent trajectory and MAX-1 vehicle geometry; showing (a) T/D ratio, (b) L/D ratio, (c) angle of attack α, (d) elevon deflection angle δ, and (e) equivalence ratio ϕ. (Ascent is for constant dynamic pressure of 140 kPa and accelerations from zero to 8 m/s^2). 130

LIST OF TABLES

Table

2.1 Scaling POD to Higher Dimensional Data Sets 20
2.2 Mean, Variance, and Standard Deviation Error 21
3.1 Measured critical air velocity (U_3^*) and computed Damköhler numbers (Da_{crit}^*) and reaction rates (ω_τ^*) at flameout for several cavity-stabilized hydrogen-air scramjet experiments. 28
3.2 Combustor entrance conditions for the cavity-stabilized hydrogen-air scramjet experiments. 29
3.3 Experimental constants for jet mixing model, tabulated in [3]. . . . 33
4.1 Parameters varied in the MASIV computations of the MAX-1 vehicle. 70
4.2 Flight trim conditions selected for cruise/acceleration on Trajectory 1. 70
4.3 MASIV vehicle parameters for the MAX-1 vehicle and three different design cases. 72
4.4 Comparison of optimization performance for the GSS to MATLAB FMINCON methods. 96
4.5 Fuel usage for several trajectories at three dynamic pressures. 97
A.1 Full list of MASIV external vehicle body design parameters. Highlighted parameters are those investigated or constrained in this study. 110
A.2 Full list of MASIV external vehicle body design parameters. Highlighted parameters are those investigated or constrained in this study. 111
A.3 Full list of MASIV external vehicle body design parameters. Highlighted parameters are those investigated or constrained in this study. 112

LIST OF APPENDICES

Appendix

A. MASIV External Vehicle Design Parameters 109

B. Details of the Flight Dynamics and Vehicle Forces 113

C. Additional Computed Metrics for 0, 1, and 2 m/s^2 Acceleration Cases 116

D. Trajectory Operating Maps for q_∞ = 70, 100, and 140 kPa 127

ABSTRACT

Combustion Efficiency, Flameout Operability Limits and General Design Optimization for Integrated Ramjet-Scramjet Hypersonic Vehicles

by

Chukwuka C. Mbagwu

Chair: Professor James F. Driscoll

High speed, air-breathing hypersonic vehicles encounter a varied range of engine and operating conditions traveling along cruise/ascent missions at high altitudes and dynamic pressures. Variations of ambient pressure, temperature, Mach number, and dynamic pressure can affect the combustion conditions in conflicting ways. Computations were performed to understand propulsion tradeoffs that occur when a hypersonic vehicle travels along an ascent trajectory. Proper Orthogonal Decomposition methods were applied for the reduction of flamelet chemistry data in an improved combustor model. Two operability limits are set by requirements that combustion efficiency exceed selected minima and flameout be avoided. A method for flameout prediction based on empirical Damkohler number measurements is presented. Operability limits are plotted that define allowable flight corridors on an altitude versus flight Mach number performance map; fixed-acceleration ascent trajectories were considered for this study.

Several design rules are also presented for a hypersonic waverider with a dual-mode scramjet engine. Focus is placed on "vehicle integration" design, differing from

previous "propulsion-oriented" design optimization. The well-designed waverider falls between that of an aircraft (high lift-to-drag ratio) and a rocket (high thrust-to-drag ratio). 84 variations of an X-43-like vehicle were run using the MASIV scramjet reduced order model to examine performance tradeoffs. Informed by the vehicle design study, variable-acceleration trajectory optimization was performed for three constant dynamic pressures ascents. Computed flameout operability limits were implemented as additional constraints to the optimization problem.

The Michigan-AFRL Scramjet In-Vehicle (MASIV) waverider model includes finite-rate chemistry, applied scaling laws for 3-D turbulent mixing, ram-scram transition and an empirical value of the flameout Damkohler number. A reduced-order modeling approach is justified (in lieu of higher-fidelity computational simulations) because all vehicle forces are computed multiple thousands of times to generate multi-dimensional performance maps.

The findings of this thesis work present a number of compelling conclusions. It is found that the ideal operating conditions of a scramjet engine are heavily dependent on the ambient and combustor pressure (and less strongly on temperature). Combustor pressures of approximately 1.0 bar or greater achieve the highest combustion efficiency, in line with industry standards of more than 0.5 bar. Ascent trajectory analysis of combustion efficiency and lean-limit flameout dictate best operation at higher dynamic pressures and lower altitudes, but these goals are traded off by current structural limitations whereby dynamic pressures must remain below 100 kPa. Hypersonic waverider designs varied between an "airplane" and a "rocket" are found to have better performance with the latter design, with controllability and minimum elevon/rudder surface area as a stability constraint for the vehicle trim.

Ultimately, these findings are beneficial and contribute to the overall understanding of dynamically stable waverider vehicles at hypersonic speeds. These types of vehicles have a range of applications from technology demonstration, to earth-to-low

orbit payload transit, to most compellingly another step in the development and realization of viable supersonic commercial transport.

CHAPTER I

Introduction and MASIV Overview

The study of hypersonic vehicles poses unique challenges in that the engine is tightly coupled with the vehicle, so it is not possible to analyze the engine by itself. Combustor pressure should not be allowed to drop too low, so the oblique shock pattern in the inlet and isolator must be strong enough to provide sufficient compression. The inlet shock strength depends on the vehicle angle of attack. This angle is determined by the trim condition that thrust, drag and acceleration be properly balanced. However, the thrust depends on the combustor pressure, temperature and other engine conditions, so these parameters are interrelated. As such, solutions can only be found through an iterative process. A second obstacle is that to create the necessary trajectory surface maps, more than 1,800 "runs" or full-vehicle computations, including the engine, had to be made. Each run computes the vehicle forces and moments as well as the axial profiles of static pressure and temperature in the engine - across the inlet shocks, the isolator, the combustor and the exhaust nozzle. One approach might be to perform high-fidelity, CFD simulations of the entire hypersonic vehicle, including the engine flow path, for the more than 1,800 run conditions. However, this requires excessive computational cost and time. Another approach is to gain an approximate understanding of the solution through a Reduced-Order Model (ROM) that provides a "first look" at a large multi-dimensional parameter space.

Previously, the advantages of ROMs have been pointed out by AFRL researchers Bolender et al. [8], by Lewis and colleagues [9, 10], by Bowcutt [11] at Boeing, by Driscoll and co-workers [1–3, 12–17] and by others [18]. The Bolender-Doman AFRL ROM was developed in 2006 [8] to simulate the flight dynamics, poles and zeros of a hypersonic vehicle. This early ROM relied on additional assumptions. Forces on each surface panel were computed using a hypersonic panel method that assumes small angle deflections, no flow separation and no detached bow shock wave. Viscous forces were estimated using hypersonic flat-plate approximations. Compression by the bow shock was computed but internal shock waves were ignored. The combustor was a constant area duct with effective heat addition due to combustion and the combustion was assumed to be fast and 100% completed within the available combustor length.

To improve on the Bolender-Doman AFRL analysis, a second-generation model, called MASIV (Michigan-AFRL scramjet in vehicle) was developed during a joint collaboration between the University of Michigan and AFRL [1–3, 12–17], some details of which are summarized in Section 1.1. Items that were added include multiple interacting shock waves in the 2-D inlet (and the exhaust nozzle) using a technique similar to the Method of Characteristics. In the combustor, 3-D fuel-air mixing was added by assuming that a wall jet issues from N wall ports. Empirical formulas were obtained from experimental data that describe the fuel concentration profiles within each fuel jet [4]. Finite-rate chemistry was added by including a strained flamelet chemistry lookup table computed from the Stanford FLAMEMASTER code.

Using the MASIV model, one run requires less than a minute of computational time on a single processor. ROMs have proven useful in this regard when the goal is to optimize the geometry, the trajectory or the control of the vehicle system. The shorter computational time also allows ROMs to quickly generate solutions over a wide parameter space, and identify areas of interest which then guide the judicious use of CFD for a smaller subset of conditions where higher accuracy is desired. Thus,

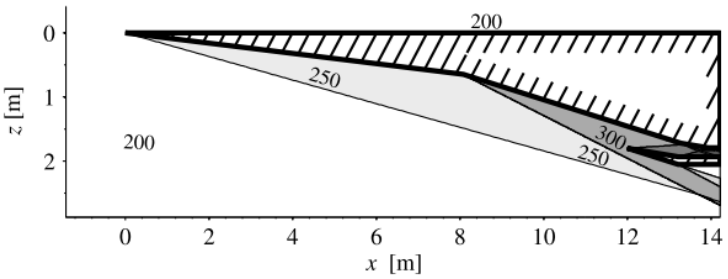

Figure 1.1: Shock and temperature (Kelvin) contours of the MAX-1 vehicle trimmed at Mach 8, computed in reference [1].

ROMs do not compete with high-fidelity CFD, but rather can be used alongside CFD to efficiently characterize and analyze large, multi-dimensional parameter spaces. The performance of MASIV has previously been validated against commercial CFD codes [1, 3].

1.1 The MASIV Model and the MAX-1 Waverider

This section details the reduced order model for the MAX-1 waverider vehicle that is drawn in Figure 3.1, with emphasis on the combustor and jet-in-crossflow formulation. The vehicle is similar to the generic aircraft that was first considered at AFRL by Bolender and Doman [8]. It has a length of 29.1 m (95.4 ft) and the width of the dual mode ramjet-scramjet engine is 2.143 m. The inlet is rectangular with a sufficiently large aspect ratio of 15.3 such that it can be considered to be two-dimensional. The isolator is 1.38 m long and is followed by the constant area portion of the combustor that is 0.90 m long; both have a cross section of 0.14 m by 2.143 m. The second part of the combustor is 0.62 m long and its upper wall diverges at 4 degrees.

Forces on each surface panel are computed using a small-angle panel method and the method to trim the vehicle is described in references [1, 12]. The engine inlet is drawn in Figure 1.1 and it contains multiple shock waves that interact. The inlet code is similar to the Method of Characteristics and it computes the static pressure

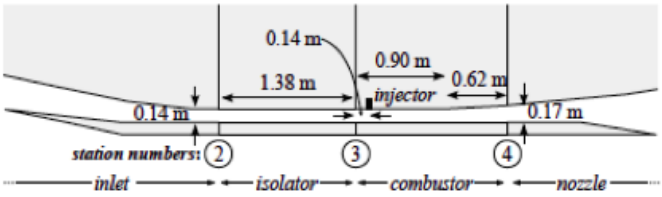

Figure 1.2: Dual-mode ramjet-scramjet internal flow path of the MAX-1 waverider.

rise and the stagnation pressure loss in the inlet. It assumes that the flow is 2-D, wall deflection angles are small, no flow separation occurs, and that the supersonic inlet Mach number is small enough that strong shock/boundary layer interactions do not occur.

The MASIV combustor sub-model was described in detail in references [1–3, 12–17] so only a summary is provided here. The code includes finite-rate chemistry, real gas properties, a three-dimensional jet mixing model, a separated boundary layer model and gas dissociation. The air stream is modeled as the 1-D flow in the duct that is drawn in Figure 1.2. It has variable area, friction, wall heat transfer and heat addition due to combustion. Fuel is injected from $N = 19$ ports that are located at one x-location that is 0.14 m downstream of station 3, as shown in Figure 1.2. The 19 fuel jets are located at different span-wise locations across the 2.143 m width; each port is 3.45 cm in diameter. Each port is choked and the hydrogen fuel enters at 300 K and at the sonic speed of 1,295 m/s.

MASIV solves the following seven ordinary differential equations, which include the conservation of mass (equation 1.1), momentum (equation 1.2), energy (equation 1.6) and species (equation 1.7). The equations are derived in references [3, 9] to be:

$$\frac{1}{\rho}\frac{d\rho}{dx} = \frac{1}{\dot{m}}\frac{d\dot{m}}{dx} - \frac{1}{u}\frac{du}{dx} - \frac{1}{A}\frac{dA}{dx} \tag{1.1}$$

$$\frac{1}{u}\frac{du}{dx} = -\frac{1}{\rho u^2}\frac{dp}{dx} - \frac{2c_f}{D} + (1 - \frac{u_F}{u})\frac{1}{\dot{m}}\frac{d\dot{m}}{dx} \tag{1.2}$$

$$\frac{1}{p}\frac{dp}{dx} = \frac{1}{\rho}\frac{d\rho}{dx} + \frac{1}{T}\frac{dT}{dx} - \frac{1}{W}\frac{dW}{dx} \tag{1.3}$$

$$\frac{1}{W}\frac{dW}{dx} = -\sum_{i=1}^{n_{sp}} \frac{W}{W_i}\frac{dY_i}{dx} \tag{1.4}$$

$$\frac{d\dot{m}}{dx} = \sum_{i=1}^{n_{sp}} \frac{d\dot{m}_{i,F}}{dx} \tag{1.5}$$

$$c_p\frac{dT}{dx} = \frac{h_{0,F} - h_0}{\dot{m}}\frac{d\dot{m}}{dx} - \frac{2c_f c_p(T_{aw} - T_w)}{\mathrm{Pr}^{2/3}D} - u\frac{du}{dx} - \sum_{i=1}^{n_{sp}} h_i\frac{dY_i}{dx} \tag{1.6}$$

Here, W is the molecular weight of the gas mixture and A is the cross sectional area. Gas properties (u, ρ, T, h) are the velocity, density, static temperature and static enthalpy, respectively. C_f is the friction coefficient, Pr is the Prandtl number and D is the hydraulic diameter of the engine. Equations 1.3 and 1.4 define the equation of state and the molecular weight (W) of the gas mixture, respectively. Equation 1.5 states that the total mass flow rate is that of the component species of the oxidizer (air), fuel (hydrogen), and other intermediate species. Note that the fuel is injected at a single x-location, downstream of the combustor entrance. MASIV also employs the following conservation equation for the species mass fraction Y_i:

$$\frac{dY_i}{dx} = \frac{\bar{\omega}_i W_i A}{\dot{m}} + \frac{1}{\dot{m}}\frac{d\dot{m}_{i,F}}{dx} - \frac{Y_i}{\dot{m}}\frac{d\dot{m}}{dx} \tag{1.7}$$

The first term on the right contains $\bar{\omega}_i$, which is the chemical reaction rate of species i. The 3-D mixing and combustion in each fuel jet is computed using empirical scaling formulas showing that the fuel jet penetration distance varies with distance as

$x^{1/3}$ and that the fuel mass fraction decays along the curved jet centerline as $x^{-2/3}$. These formulas provide the jet mixture fraction (Z) as a function of (x, y, z) for each jet. Mixture fraction fluctuations and scalar dissipation rates at each (x, y, z) location are assumed to be proportional to mean scalar gradients. Strained flamelet lookup tables similar are created assuming a Beta function pdf and solutions to the counter flow flamelet equation, to include finite rate chemistry effects. Reaction rates then are integrated over the y and z directions to yield 1-D profiles that are inserted into the first term on the right side of 1.7. Results in [19] showed that the finite-rate chemistry in the MASIV code prevents all the fuel from burning if the combustor gas velocity becomes too large or the combustor static pressure is too low.

CHAPTER II

Methods and Application for Flamelet Table Reduction

2.1 Introduction

The combustion flamelet data used in MASIV are stored in large, multi-dimensional matrices. The model is based on laminar diffusion flamelet theory. In particular, the gas reaction rates are found in 3-D lookup tables for each gas species that contain the rate data for discrete permutations of mixture fraction f, mixedness s, and scalar dissipation χ. Currently, data is retrieved through an interpolation of the function along the table near the given dimensions. It was necessary to speed up the interpolation process as additional dimensions were added. A program called FlameMaster was used to compute chemical kinetics, solve the flamelet equations and generate the numerous lookup tables. The chemistry lookup tables have many millions of values, but more than 90% of these values are nearly zero. Two methods were tried to reduce the lookup tables and speed up the interpolation: Artificial Neural Networks and Proper Orthogonal Decomposition. They are described in the following sections.

2.2 Artificial Neural Network

Artificial neural networks (ANNs) are adaptive computational models often used for data classification, function approximation, and signal processing. ANNs can represent complex functions with multiple inputs and outputs, are highly generalizable, and are efficient in the storage of this information. The network topology consists of one or more layers of interconnected neurons (excluding the input/output layers), and each neuron is a mathematical function given by a weighted sum of its inputs applied to a nonlinear transfer function.

A feedforward neural network architecture is used for the analysis, meaning that information is only propagated in one direction, from the inputs to the outputs, and there are no feedback loops. It is comprised of an input layer with N_I input channels and an output layer with N_O output channels. The neural network explored in this work contains additional inner layers and interior nodes (or neurons) between the input and output layer. Figure 2.1 shows the structure of a neuron, and an example of a multi-layered network is given in Figure 2.2.

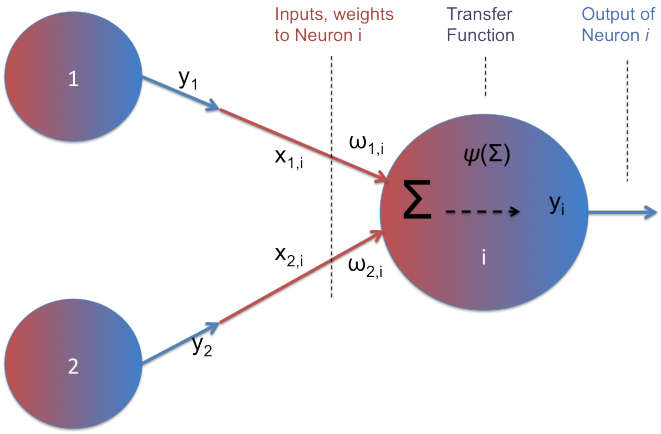

Figure 2.1: Schematic of a neuron, i.

Following the formulation given in Ihme [20], the neuron outputs are given by

$$y_i = \psi_i \left(\sum_{j \neq i}^{N_{neurons}} C_{ij} \omega_{ij} x_{ij} \right) \tag{2.1}$$

where

$$C_{ij} = \begin{cases} 1 & \text{if } i \text{ and } j \text{ are linked} \\ 0 & \text{otherwise} \end{cases}$$

The weights of the connecting links are ω_{ij}, and x_{ij} represents the inputs to the neuron. A common choice of the nonlinear transfer function ψ_{ij}, and used here, is the hyperbolic tangent

$$\psi_i(s) = \tanh\left(a_i + s\right) \tag{2.2}$$

where a_i is a scalar offset value for the ith neuron.

In the present work, the artificial neural network contains an input layer with 3 input channels (f, s, χ): the mixture fraction and mixedness (range: 0 to 1), and the scalar dissipation (range: 0^+ to 300) of the observed gas. The output layer contains a single output channel, the reaction rate of the gas. For simplicity and illustration, the analysis is limited to the study of a single gas specie, H_2O, which reduces the problem dimensionality. The network, shown in Figure 2.2, contains four inner layers with varying numbers of neurons. The selection of this network topology is examined in a trade study.

2.2.1 Training

Neural networks must undergo an iterative training process whereby the connecting link weights (ω_{ij}) and offsets (a_i) are optimally selected to approximate the known function, given a certain network topology Γ. In this case the approximated function is the reaction rate table data. The cost function is a least squares approach to the approximation error, and the network training process minimizes this function. The

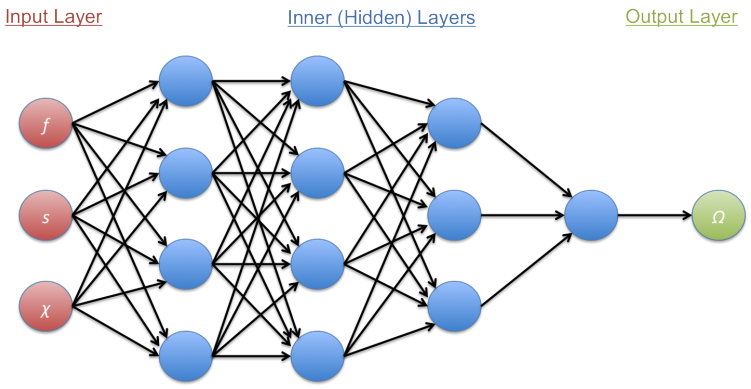

Figure 2.2: Optimized Artificial Neural Network Topology, Γ.

cost function is given by

$$J_{cost}(\Gamma) = log\left(\sqrt{\frac{1}{N_S}\sum^{N_S}\left(Y^A(j) - Y^{NN}(j)\right)^2}\right) \tag{2.3}$$

where Y^A is the actual reaction rate at the test points, Y^{NN} is the neural network output, and N_S is the number of test samples (in this work all table values were used as samples, though only a representative portion is required). The logarithmic form of the cost function amplifies the gradients near zero, for use with a numerical solver.

2.2.2 Network Topology: Trade Study

The optimization problem of artificial neural network topology remains complex due to, in the most general case, its unbounded parameter space (unlimited number of input/output channels, layers, and neurons). Various solution methods have been developed, including the generalized pattern search (GPS) method employed by Ihme [20] and a genetic algorithm is used by Fiszelew et. al. [21]. For the current work, the topology was determined ad hoc with bounds imposed on the problem: the number of layers was fixed at 6 (2 input/output, 4 inner), and the maximum number of neurons in each inner layer was constrained to 6. These bounds were primarily motivated by training and computational time, as well as simplicity for demonstration. As a result,

the optimal network topology could be found through a trade study, and other formal optimization techniques were foregone.

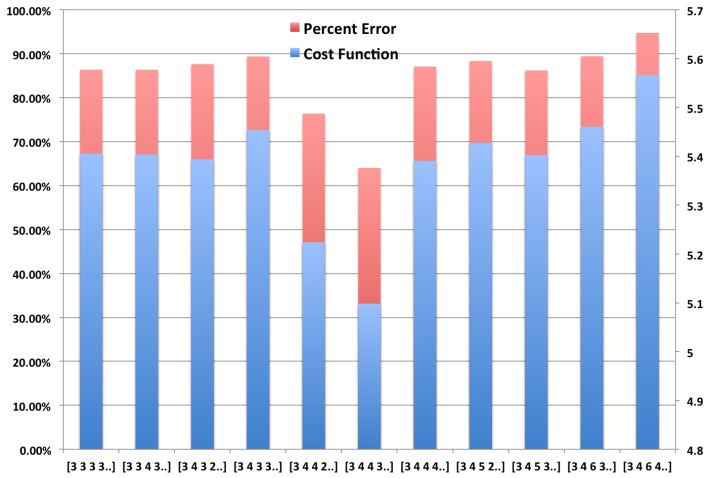

Figure 2.3: Objective (Cost) Function and Reaction Rate Percent Error for Various Topologies.

In the trade study, the number of neurons in each inner layer was varied. By design in Ihme [20], the last inner layer was constrained to a single neuron with its transfer function is given by

$$\psi_i(s) = s \tag{2.4}$$

In Figure 2.3, the results of the trade study are shown. The variation of neurons in each layer is shown on the x-axis, omitting the last inner and output layer which are common to all topologies. The maximum reaction rate percent error is viewed on the left axis and the right axis displays the final cost function value after training. The optimal topology, [3 4 4 3 1 1], was such that the maximum percent error across all sample points was minimized.

The corresponding error map is visualized in the Figure 2.4, sliced at the incremental scalar dissipation values. The color represents the error magnitude of the ANN output, and the range of the colorbar is the total range of the reaction rates from the function table. It was found that scalar dissipation had the strongest proportional

effect on the absolute error. The optimal artificial neural network topology resulting in this error map is found in Figure 2.2. Other network topologies confirmed a similar surface map, but with larger error magnitudes. Figure 2.5 compares the reaction rates given by the lookup table and those approximated by the neural network.

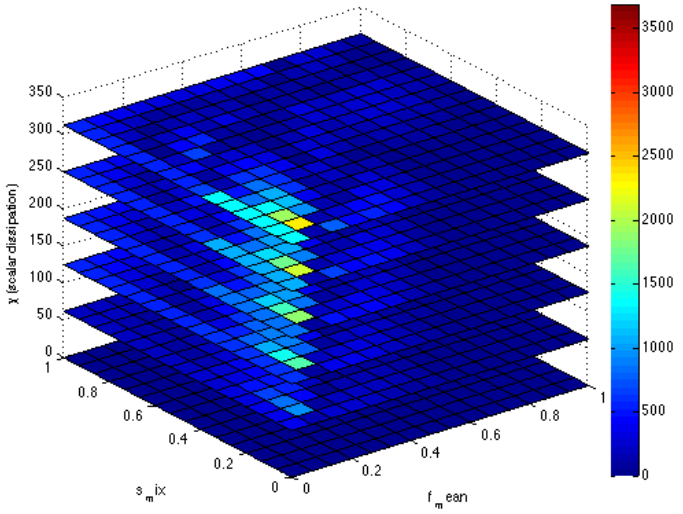

Figure 2.4: Reaction Rate Percent Error Map of Optimal ANN Approximation (3-D function).

2.2.3 Results of the Artificial Neural Network Interpolation

The ad hoc trade study did not produce observable trends or give insight into the effect of incremental modifications to the network topology. The topologies in Figure 2.3 are ordered by increasing number of neurons, and it is not clear that the addition or removal of neurons to a network inherently provides better results.

The application of the artificial neural networks to the system did not perform as well as expected. The approximation error of the reaction rate in many regions of the 3-D parameter space is too large to overlook. Prior research and literature has shown ANNs to be capable of similar function approximations, so it is believed the present complications lie in the implementation. The most likely source of error is the cost function minimization during training, where the numerical solver may become

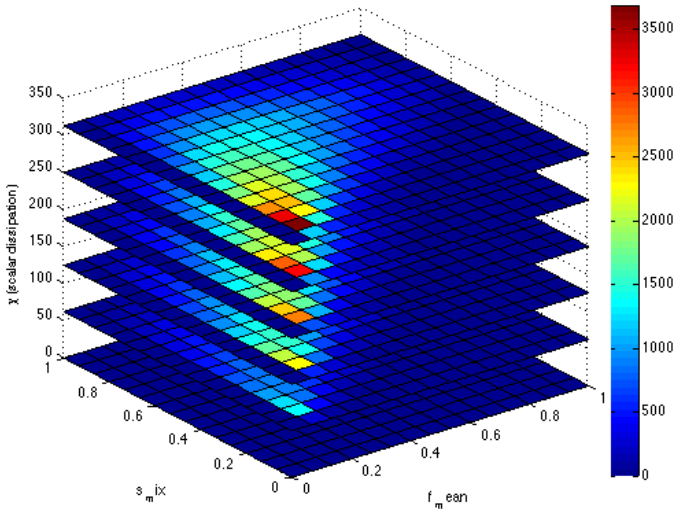

(a)

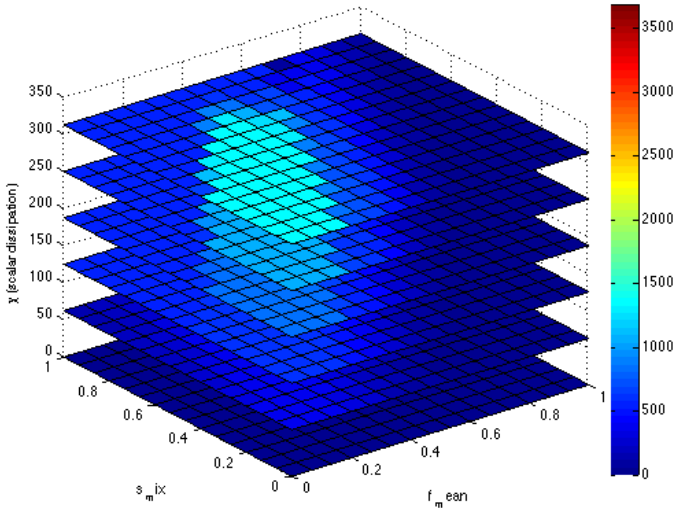

(b)

Figure 2.5: Reaction Rates given by (a) the 3-D lookup table and (b) neural network approximation.

entrenched in local minima and never reach the global minimum. Additionally, the initial guess to the solver may cause it to converge to less-than-optimal connecting link weight and offset values for the network. Reducing the resolution of the parameter space for an initial solve may raise the probability of converging in the region of the

true global minima. Global optimization toolboxes also exist to achieve similar goals. These approaches may be considered to improve the approximation results, if the ANN approach is to be used. Another possible source of error is that the weighting system of the neural network architecture is not well suited to model each of the gas species together as a function. In the flamelet reaction, some species are generated and others consumed/depleted at varying rates. It is likely that approximating the chemistry tables individually, separated by species, would be better suited and well-formed for the Artificial Neural Network method.

Future work includes expanding the neural network architecture across all gas species and repeating the analysis. When fully integrated, a storage/memory, timing, and thermodynamic analysis will be performed on a nominal MASIV simulation, comparing the results with and without the artificial neural network architecture.

2.3 The Proper Orthogonal Decomposition

The proper orthogonal decomposition (POD) is a well-defined method of producing reduced-order, but very accurate, models of large or complex data sets. It has been used in computational fluid dynamics (CFD) analysis to examine correlations of the structure of turbulent flowfields in time[22–24]. Other time-domain applications include constructing reduced-order models (ROM) of cylinder vortex shedding[25] and an aeroelastic model of a two-dimensional airfoil[26]. Analogous frequency-domain POD techniques have been explored by Kim[27], applied to a spring damper system and three-dimensional vortex lattice model. ROMs constructed using POD have been combined with structural dynamic models and applied to aeroelastic systems[28, 29]; it has also been found effective for flutter analysis[27, 30]. It has also been used for reduced-order models of atmospheric and oceanographic data, where the control space is high-dimensional[31].

Here we discuss the application of POD techniques to reduce multidimensional

flamelet chemistry data used in a model for the mixing and combustion of turbulent jets in crossflow. A brief overview of POD theory is given, and those methods are applied to the flamelet data in the turbulent reacting flow. The advantages and scalability of this technique is explored, and the outputs of the full, non-reduced flamelet model to that of the results of the POD analysis are compared.

Consider a model where a vector $\mathbf{u}_j$ is calculated at J discrete points within some domain for $j = 1, 2, \ldots, J$. The $\mathbf{u}_j$ vector may consist of P quantities of interest as shown in equation (2.5).

For a two-dimensional inviscid flow problem, one might choose a vector $\mathbf{u}_j$ where $P = 4$ and the states are density, x-momentum, y-momentum, and energy. But in general, $\mathbf{u}_j$ may contain any type of information for points P. In this work $\mathbf{u}_j = \dot{\omega}_j$, the reaction rate for a single species as a function of several flamelet reference variables, as described in Section 2.3.1.

Combining the solution vectors $\mathbf{u}_j$ over the domain of J points, we end up with a column vector of the form

$$\mathbf{u}_j = \begin{pmatrix} u_{j,1} \\ \vdots \\ u_{j,P} \end{pmatrix}, \qquad \mathbf{q}^m = \begin{pmatrix} \mathbf{u}_1 \\ \vdots \\ \mathbf{u}_J \end{pmatrix} \tag{2.5}$$

where $\mathbf{q}^m$ is a snapshot of the configuration for $m = 1, 2, \ldots, M$. Continuing the example of the inviscid CFD problem, m can be chosen to be snapshots in time. However, m may generally be any parameter or configuration affecting the solutions at each of the J points.

The goal of POD is to represent all of the data approximately using a linear combination of $K \leq M$ basis vectors ϕ_k. These vectors are much like snapshots, but are not in general equal to any individual snapshots. Linearly combining the M snapshots yields

$$\phi_k = \sum_{m=1}^{M} \mathbf{q}^m v_k^m = \mathbf{S}\mathbf{v}_k \iff \Phi = \mathbf{S}\mathbf{V} \tag{2.6}$$

where $\mathbf{v}_k = \left(v_k^1, v_k^2, \cdots, v_k^M \right)^T$ and each entry is the contribution of the mth snapshot to the kth basis vector. Φ is a matrix of dimension $J \times K$ such that each colum is a basis vector ϕ_k. $\mathbf{S}$ is a matrix of dimension $J \times M$ such that each column is a snapshot $\mathbf{q}^m$. $\mathbf{V}$ is a matrix of dimension $M \times K$ such that each column is $\mathbf{v}_k$.

Hall et al.[32] shows that this result reduces to an eigenvalue problem of the form

$$\mathbf{S}\mathbf{S}^H\mathbf{S}\mathbf{v}_k = \lambda_k \mathbf{S}\mathbf{v}_k \tag{2.7}$$

where $\mathbf{S}^H$ is the Hermitian or conjugate transpose of $\mathbf{S}$. Solving for the eigenvalues λ_k provides a correlation between the eigenvectors $\mathbf{v}_k$ and the basis vectors ϕ_k. The eigenvectors with the largest values of λ_k contribute the most to the values of ϕ_k.

Rathinam and Petzold[33] explore the corollary for representing data sets in a general real space $\mathbb{R}^n$, using a subspace $\mathbb{S} \subset \mathbb{R}^n$. Here, POD minimizes the total square distance of the former data set to the projected data on $\mathbb{S}$, and $\mathbb{S}$ corresponds to the subspace determined by largest eigenvalues of the system.

2.3.1 POD On Flamelet Chemistry Data

The reduced-order mixing model examined in this work is part of the MASIV architecture, which is a complete flow model developed at the University of Michigan for a hypersonic vehicle with specified geometry and gas properties. It is further described in Torrez et al.[3] The mixing ROM incorporates the pressure, temperature, mean mixture fraction f, mixture fraction variance s, and the scalar dissipation rate χ of various gas species to determine the reaction rates throughout the combustion process and subsequently solve the 1D conservation equations. The reaction rate of each species varies with the aforementioned parameters, and those parameters are

functions of the spatial variables in the vehicle combustor and isolator. As a result, multiple chemistry tables must be generated and stored to capture the reaction rate behavior for the wide range of pressures, temperatures, scalar dissipation rates, and species. The chemistry tables are then interpolated to find the particular reaction rate at a given location and condition.

Following the formulation described in Section 2.3, the solution vector, or quantity of interest, $\mathbf{u}_j$ is set to be the reaction rate at the jth value of the lookup variables. The mean mixture fraction and variance parameters are bounded between 0 and 1, so the j-values are chosen to be discrete combinations of f and s, respectively. The data sets contain $n_1 = 201$ discrete mean mixture fraction points and $n_2 = 25$ mixture fraction variance points, creating $J = n_1 n_2 = 5025$ combinations of the aforementioned lookup variables. Therefore, one snapshot of the solution $\mathbf{q}^m$ in configuration m is defined as

$$\mathbf{u}_j = u_j = \dot{\omega}_j, \qquad \mathbf{q}^m = \begin{pmatrix} \dot{\omega}_1 \\ \vdots \\ \dot{\omega}_{5025} \end{pmatrix}, \qquad \mathbf{S} = \left(\mathbf{q}^1, \cdots, \mathbf{q}^M \right) \tag{2.8}$$

This snapshot is graphically shown in Figure 2.6, for a given configuration. $\mathbf{S}$ is then a row vector of the M snapshots. For the simplest case in this work, these snapshots are chosen to be $M = 46$ scalar dissipation rates at a fixed temperature and pressure for one species.

Discrete methods of POD are analogous to a matrix decomposition called singular value decomposition[34], which is a common mathematical tool implemented on many computational platforms, and is used for this analysis. Any matrix $\mathbf{S}$ can be written as the product

$$\mathbf{S} = \mathbf{U}\Sigma\mathbf{W}^H \tag{2.9}$$

where $\mathbf{U}, \mathbf{W}$ are unitary matrices of size J and M, respectively. Σ is a $J \times M$ matrix

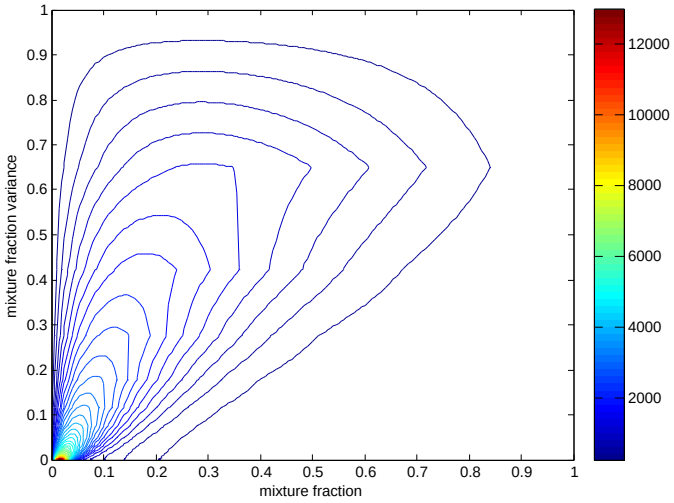

Figure 2.6: Contours of Reaction Rate for H2O at p = 2.61 bar, T = 1280 K, and χ = 312.3 [1/s].

where the diagonal entries $\sigma_m = \sqrt{\lambda_m}$ are the square roots of the eigenvalues of $\mathbf{S}^H\mathbf{S}$, and are the only nonzero entries. For discrete POD analysis, we propose choosing a correlation quantity $0 < \Gamma \leq 1$ and setting K as the smallest integer such that

$$\sum_{k=1}^{K}\sigma_k / \sum_{m=1}^{M}\sigma_m \geq \Gamma, \qquad K \leq M \tag{2.10}$$

for the Σ matrix. The determination of a satisfying K value subsequently yields the basis functions for the approximation as described in Section 2.3. An analogous approach for the general real space example in [33] defines a *correlation matrix* from which the eigenvalues are determined. A similar procedure is followed in [31] for producing this matrix to compute the eigenvalues.

For this application, we look to the simplest case of taking the snapshots $\mathbf{q}^m$ of the $\mathbf{S}$ matrix in equation (2.8) to be a range of $M = 46$ scalar dissipation rates for a single species, H_2O, at a fixed pressure and temperature. The correlation quantity is set to be $(1 - \Gamma) = 10^{-3}$. Decomposing $\mathbf{S}$ and satisfying the condition in equation (2.10) for Σ, one finds that $K = 4$.

We create three new matrices: $\tilde{\Sigma} = diag\left(\sigma_1, \cdots, \sigma_{K=4}\right)$, with all other entries

being zero, and $\tilde{\mathbf{U}}, \tilde{\mathbf{W}}$ as the $(J \times 4)$ and $(M \times 4)$ parts of the $\mathbf{U}$ and $\mathbf{W}$ matrices, respectively. These three matrices approximate the function of the entire table with only a fraction of the data and storage. By multiplying $\tilde{\mathbf{U}}, \tilde{\Sigma}$, and $\tilde{\mathbf{W}}$ according to equation (2.9) we can recover a new data set $\tilde{\mathbf{S}}$, which is an accurate approximation of $\mathbf{S}$. A comparison of $\mathbf{S}$ and $\tilde{\mathbf{S}}$ for the same snapshot is shown in Figure 2.7.

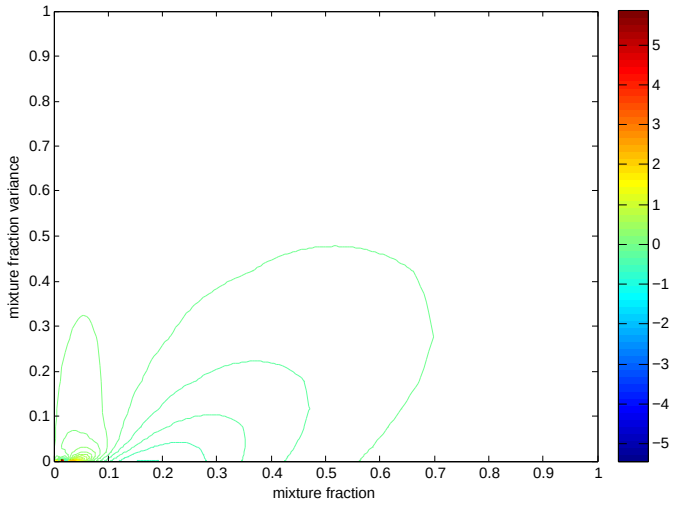

Figure 2.7: Contours of Reaction Rate Error for H2O at p = 2.61 bar, T = 1280 K, and $\chi = 312.3$ [1/s].

The fractional savings can be measured by comparing the number of data points in the decomposition to that of the full set:

$$\delta = \frac{(J \times K) + (K \times K) + (K \times M)}{(J \times M)} \times 100\% \tag{2.11}$$

For this example of H_2O at $p = 2.61$ bar and $T = 1280$ K, we find that $\delta = 8.78\%$. This shows that a small percentage of the data can be retained, while still capturing nearly all of characteristics of the reaction rate behavior over the domain.

2.3.2 Additional Input Dimensions to the POD Approximation

The POD analysis may be extended to account for additional parameters on which the reaction rate depends. In Section 2.3.1, the gas species, pressure, and temperature

were specified such that the only variable parameter outside of the J points of mixture fraction/variance was the scalar dissipation rate. The range of the scalar dissipation rates made up the M snapshots. Say that we are now interested in the reaction rates for N number of species. We must then obtain tabulated data for the matrix $\mathbf{S}^n$ given in equation (2.8) for each of the N species. Defining a new matrix $\mathbf{S}_{total}$, a concatentation of the $\mathbf{S}$ matrices, we get

$$\mathbf{S}_{total} = \left(\mathbf{S}^1, \cdots, \mathbf{S}^N\right) \tag{2.12}$$

Introducing additional dimensions to the data follows the same procedure. Allowing pressure as a variable will require the result in equation (2.12) to be tabulated at each pressure. Accounting for temperature variation again multiplies the size of the resulting matrix by the number of temperature points, and so on. Thus, the general $\mathbf{S}_{total}$ matrix will be of the form:

$$\mathbf{S}_{total} = \Bigg[\underbrace{\overbrace{\underbrace{\mathbf{q}^1, \cdots, \mathbf{q}^M}_{\mathbf{S}^1}, \cdots, \mathbf{S}^N}^{\mathbf{S}_N^1}, \cdots, \mathbf{S}_N^R}_{\mathbf{S}_{N,R}^1}, \cdots, \mathbf{S}_{N,R}^V, \cdots\Bigg] \tag{2.13}$$

for additional dimensions with number of points M, N, R, V, . . . , respectively. Note that while the total number of snapshots $\mathbf{q}^{M\times N\times R\times V\times\cdots}$ increases with the added dimensions, the number of $J = 5025$ points remains the same.

Table 1 compares the results of POD for increasing numbers of snapshots and dimensions, for the same correlation quantity $(1 - \Gamma) = 10^{-3}$.

Table 2.1: Scaling POD to Higher Dimensional Data Sets

Varying Parameters	# Data Points	# Basis	Fraction δ
None (1) - no reduction	5025	1	100%
× Scalar Dissipation (46)	231150	4	8.78%
× Species (8)	1849200	8	2.34%
× Pressures (4)	7396800	10	0.75%

The information here shows that POD is highly effective in approximating multidimensional data sets, while only adding few eigenvalues/basis functions for each new parameter and using a smaller fraction of the total data.

2.3.3 Accuracy of the POD Interpolation and Conclusion

To determine the accuracy of the POD approximation, we compare the original data set $\mathbf{S}$ to the recovered data set $\tilde{\mathbf{S}} = \tilde{\mathbf{U}}\tilde{\Sigma}\tilde{\mathbf{W}}^H$ after the matrix decomposition and eigenvalue analysis. Integrating the absolute error of the reaction rate at each point in the matrices is an insufficient approach, as larger data sets will inevitably sum to larger total errors. Instead, we look to match the aggregate properties of both data sets, the mean, variance, and standard deviation, and infer the accuracy of the approximation from their likeness. Table 2 shows the percent difference of the root-mean-square $(\tilde{\mu}, \mu)$, variance $(\tilde{\nu}, \nu)$, and standard deviation $(\tilde{\sigma}, \sigma)$ of the approximated data set $\tilde{\mathbf{S}}$ with respect to $\mathbf{S}$, for each case discussed in Section 2.3.2.

Table 2.2: Mean, Variance, and Standard Deviation Error

Varying Parameters	$(\tilde{\mu}/\mu - 1)$	$(\tilde{\nu}/\nu - 1)$	$(\tilde{\sigma}/\sigma - 1)$
None (1) - no reduction	-3.8×10^{-8}	5.8×10^{-5}	2.9×10^{-5}
$\times$ Scalar Dissipation (46)	-8.8×10^{-8}	8.0×10^{-6}	4.0×10^{-6}
$\times$ Species (8)	-9.2×10^{-8}	-1.8×10^{-7}	-9.2×10^{-8}
$\times$ Pressures (4)	-8.5×10^{-8}	-1.7×10^{-7}	-8.5×10^{-8}

The results show that even while the size of the data increases significantly with each added dimension, the aggregate behavior of the reaction rate for both the original data set and the POD approximation remain strongly correlated. It is important, however, to recognize that this is not necessarily true for the general case. It is possible to construct data sets such that the matrix $\mathbf{S}$ becomes ill-conditioned and the eigenvalue analysis produces less accurate basis vectors. In such cases, POD is not sufficient and other methods must be used for a better approximation.

We can see that for this application, using POD to reduce and approximate large

flamelet chemistry data sets proves to be very effective and accurate. Where the multidimensionality of the reaction rate requires numerous chemistry tables to be generated, POD is most useful in reducing the storage and memory footprint, while maintaining the integrity of the data with low error margins. This allows those computational resources to be allocated elsewhere in the reduced-order model. If not all of the data is needed, the relevant portions can be recovered by combining only parts of the decomposition, eliminating the wasted storage of keeping the full chemistry tables. Recovering the full data set is easily done by multiplying the full matrices from the decomposition.

CHAPTER III

Combustion Efficiency and Flameout Limits from Empirical Damköhler Numbers

3.1 Introduction

There are several interesting tradeoffs that occur when a hypersonic waverider ascends along a trajectory of constant dynamic pressure ($q = 1/2\rho_\infty U_\infty^2$). Figure 3.1 shows the geometry of the MAX-1 waverider that the authors have analyzed [1–3, 12–17] using their reduced order model called MASIV (Michigan-AFRL Scramjet In-Vehicle). A constant-q trajectory might be selected from one of the three solid curves in Figure 3.2, which is a flight corridor map of altitude versus flight Mach number. The unstart limit that is shown was computed in reference [1]; it occurs when the combustor applies an excessively high back pressure on the shock train in the engine isolator, forcing the shocks to move upstream and creating unwanted spillage. The low and high ambient pressure operability limits are described in Section 3.4. Two operability limits of interest are the flame instability or flameout limit, a hard constraint, and the loose requirement of maintaining a high combustion efficiency $> 90\%$. The second requirement is flexible in that operating at lower efficiency is feasible, but leads to excess fuel burn and reduced range. A desired trajectory is one that avoids crossing these two limits. Computations of these operability limits have

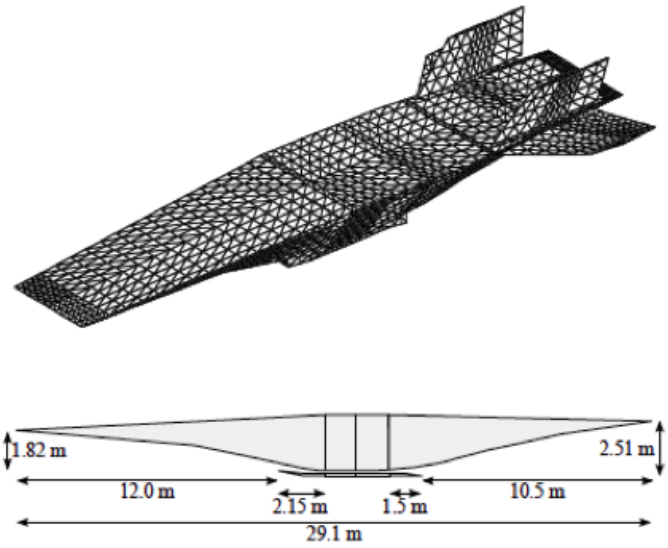

Figure 3.1: The MAX-1 hypersonic waverider vehicle. Engine width is 2.143 m. For details, see references [2, 3].

not been reported previously; to do so, our reduced order model [1–3, 12–17] had to be improved using the approach described in Section 3.3.

During the vehicle ascent, the ambient static pressure drops, creating low pressure conditions that reduce the chemical reaction rates in the combustor, despite the initial inlet compression. Ambient static temperature does not vary as significantly by comparison. Another undesirable effect is that the air flow velocity in the combustor increases, reducing the residence time available to complete combustion. However, the vehicle accelerates along the ascent trajectory, increasing the flight Mach number and oblique shock strength. Since ambient static temperature remains relatively constant (small relative rise), this then increases the static temperature entering the combustor after the shock train and tends to speed up the finite-rate chemistry. Figure 3.3 illustrates the inverse trends of static pressure and temperature with increasing altitude.

Another complication is that the fuel-air equivalence ratio (ER) varies in a different way along each trajectory, and it cannot be specified a priori. ER is determined by two factors: the thrust that is required to "trim" the vehicle, and the entrained

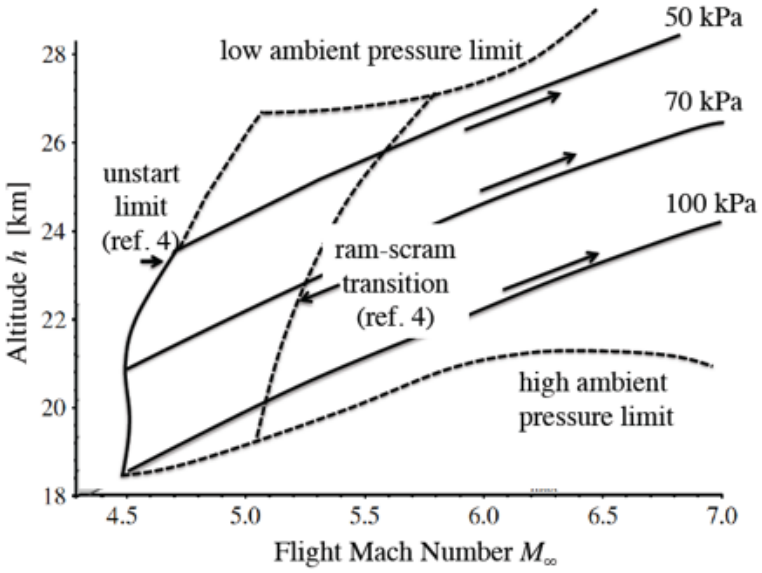

Figure 3.2: Schematic of the flight corridor map with three possible ascent trajectories of constant dynamic pressure. Unstart limit and ram-scram transition curves were previously computed in reference [1]. The following sections describe how the low and high ambient pressure limits depend on combustion efficiency and flameout.

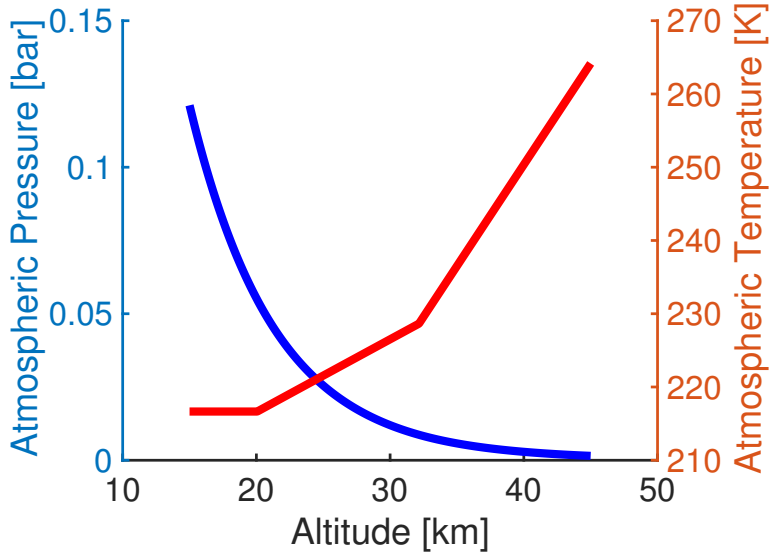

Figure 3.3: Atmospheric conditions for pressure p_∞ (blue, left) and temperature T_∞ (red, right) as a function of altitude.

air mass flow rate. Trimming the vehicle is an iterative process by which a vehicle configuration is computed that balances the aerodynamic and propulsive forces such that a given flight condition (Mach number, acceleration, and altitude) is met. The equivalence ratio ER, angle-of-attack, and control surface deflections are independent parameters that constitute the vehicle configuration; they are varied until the flight condition is matched within tolerance. Thrust depends on the vehicle drag and angle of attack, which in turn depends on the vehicle weight. The engine air mass flow rate is $\rho_\infty U_\infty A_c$ and this can be rewritten as $(2q\rho_\infty)^{1/2}A_c$, where A_c is the capture area. Selecting a large dynamic pressure q trajectory will tend to increase the air mass flow rate and reduce the required equivalence ratio ER for trim. However, this relation shows that during ascent, the air mass flow rate drops due to the low gas density at high altitudes, which tends to increase the ER necessary to meet the target flight condition, including the target acceleration. Due to these complex tradeoffs, a model can help to understand how ER, pressure, temperature and gas velocity in the combustor can affect the combustion efficiency and the flameout limit.

3.2 Defining the Operability Limits

One of the operability limits of interest corresponds to the requirement that combustion efficiency (η_C) exceeds 0.90. Heiser and Pratt [35] define η_C to be:

$$\eta_C = \frac{\dot{m}_{H2,burned}}{\dot{m}_{H2,inj}} = \frac{\dot{m}_{H2,inj} - \dot{m}_{H2,4}}{\dot{m}_{H2,inj}} \tag{3.1}$$

where $\dot{m}_{H2,inj}$ is the mass flow rate of the hydrogen fuel that is injected from wall ports. The quantity $\dot{m}_{H2,4}$ is the mass flow rate of unburned hydrogen that passes through the combustor exit. Stations 3 and 4 are defined to be the entrance and exit of the combustor, respectively, as drawn in Figure 3.1.

The second operability limit of interest is the flameout limit [35–40]. Flameout occurs when the air velocity at the entrance to the combustor (U_3) exceeds the critical air velocity (U_3^*) that is determined by setting the normalized Damköhler number Da_H equal to one. The Damköhler number criterion was pioneered by Ozawa [38] and has been validated in many studies, including recent advances by Lieuwen [39] and Driscoll [37]. Damköhler number Da is defined as the ratio of the fluid mechanical time to a chemical time τ:

$$Da = \frac{S_L^2/\alpha}{U/H} \approx \frac{\textit{reaction rate } \omega_\tau}{\textit{diffusion rate}} \tag{3.2}$$

where S_L is the laminar burning velocity and α is the thermal diffusivity. The inverse of the numerator in equation 3.2 is the chemical time τ, which is correlated to a maximum fuel reaction rate $\omega_\tau \approx 1/\tau$. For $Da \gg 1$, the reaction rate is much greater than diffusion and the steady solution is said to be diffusion limited. For $Da \ll 1$, diffusion occurs much faster than the reaction.

Da is computed for a number of experiments with cavity flameholders in a high-speed crossflow. These experiments [41–45] measured flame stability under various flow conditions and cavity configurations, at or immediately prior to flame blowout. Critical Damköhler number and reaction rate, Da^*_{crit} and ω^*_τ, are computed in the MASIV combustor ROM from the given experimental conditions.

We define the normalized Damköhler number Da_H to be:

$$Da_H = \frac{\omega_\tau/(U_3/H)}{[\omega^*_\tau/(U^*/H)]_{flameout}} = \frac{\omega_\tau/(U_3/H)}{Da^*_{\text{crit}}} \tag{3.3}$$

such that $Da_H = 1$ at a critical or flameout Damköhler number. Above this value, Da_H represents a stable flame while $Da_H < 1$ signals flameout.

ω_τ is the maximum reaction rate of the fuel (in 1/seconds), defined in equation 3.16 and illustrated by the starred points in Figure 3.6(b). It depends on the equivalence

ratio (ER), static pressure (p_3) and static temperature (T_3) at the combustor entrance. Similarly to previous studies [41–50], it is assumed that a wall-cavity flame holder is used so the characteristic length scale is the height (H) of the wall-cavity. The recirculating flow in the wall-cavity is not explicitly modeled in MASIV. Equation 3.3 is rearranged to state that the critical air velocity U_3 at the flameout limit ($Da_H = 1$) is:

$$U_3^* = k_1 H \omega_\tau \tag{3.4}$$

The constant k_1 in equation 3.4 is another way of representing the denominator of equation 3.3. Constant k_1 must be determined from experimental data because CFD computations cannot reliably compute a flameout limit. Fortunately, there are many measured values of flameout limits for cavity flame holders that provide values of k_1. Measurements of Takahashi et al. [41] were selected because their flameout limit was recorded for a scramjet experiment that was operated on hydrogen fuel with a cavity flame holder. They measured a flameout velocity (U_3^*) at 1336 m/s for a cavity height (H) of 0.36 cm. Their static temperature (T_3) and pressure (p_3) were 1,111 K and 0.47 bar, respectively. From these values, their reaction rate ω_τ^* is computed by the MASIV code. The resulting value of constant $k_1 = 2893$ for Takahashi et al.[41], and this was used in our analysis. Table 3.1 lists other experiments with reported values of U_3^* and Da_{crit}^* that could be used instead of those of Takahashi et al.

Table 3.1: Measured critical air velocity (U_3^*) and computed Damköhler numbers (Da_{crit}^*) and reaction rates (ω_τ^*) at flameout for several cavity-stabilized hydrogen-air scramjet experiments.

Author	Fuel	Critical Velocity U_3^* (m/s)	$Da_{crit}^*(\times 100)$	ω_τ^* (1/s)
Takahashi et al. [41]	H_2	1336	0.03456	128.29
Sun et al. [42]	H_2	991	0.13757	170.48
Micka, Driscoll [43]	H_2	487	3.9066	1498.03
Kang et al. [44]	H_2	1707	0.15051	856.63
Retaureau et al. [45]	H_2	1100	0.13855	60.002

Table 3.2: Combustor entrance conditions for the cavity-stabilized hydrogen-air scramjet experiments.

Author	Fuel	Temperature T_3 (K)	Pressure p_3 (bar)	Cavity step height H (m)	Equivalence ratio (ER)
Takahashi et al. [41]	H_2	1111	0.47	0.0036	0.30
Sun et al. [42]	H_2	823	1.01	0.0080	0.40
Micka, Driscoll [43]	H_2	1390	0.50	0.0127	0.30
Kang et al. [44]	H_2	1570	1.32	0.0030	0.18
Retaureau et al. [45]	H_2	410	0.65	0.0254	0.25

There are several goals of the present study. Two cases were defined; the first is called the assessment case and the second is the ascent case. For the assessment case the vehicle does not ascend and three of the four parameters [p_3, T_3, U_3, and ER] are fixed. Initially, p_3 is varied alone and later T_3 is varied alone, and two quantities are computed: combustion efficiency and Damköhler number. The results help to understand the relative role of pressure and temperature. In contrast, for the ascent case, all four of these parameters vary as the vehicle ascends along a constant dynamic pressure trajectory, with a fixed vehicle acceleration. Trim conditions are imposed at several different altitudes along each of the nine trajectories (i.e., values of dynamic pressure). At each altitude the forces and moments are computed at multiple angles of attack to determine the angle and fuel-air ratio that trims the vehicle. Along each trajectory, the altitude is recorded where flameout occurs and where η_C drops below 0.90. Results are stored in a multi-dimensional matrix used to plot operability limits and determine a trajectory that maximizes combustion efficiency while avoiding the aforementioned limits.

3.2.1 The jet spreading and mixing model for N jets in a crossflow

An important quantity is the volumetric reaction rate of each species ($\bar{\omega}_i$) that appears in equation 1.7 within the first term on the right side. This reaction rate controls how the mass fraction of each species (Y_i) varies in the x-direction. The overbar denotes that $\bar{\omega}_i$ has been averaged over the y and z directions, so it is only

a function of the streamwise coordinate (x). The reaction rate depends on two sub-models: an empirical model for the 3-D fuel-air mixing of a jet in crossflow and a sub-model of the finite-rate chemical reactions. Both are described in detail in Torrez et al. [3]. A spatial representation of the spreading profile for a jet in crossflow is shown in Figure 3.4.

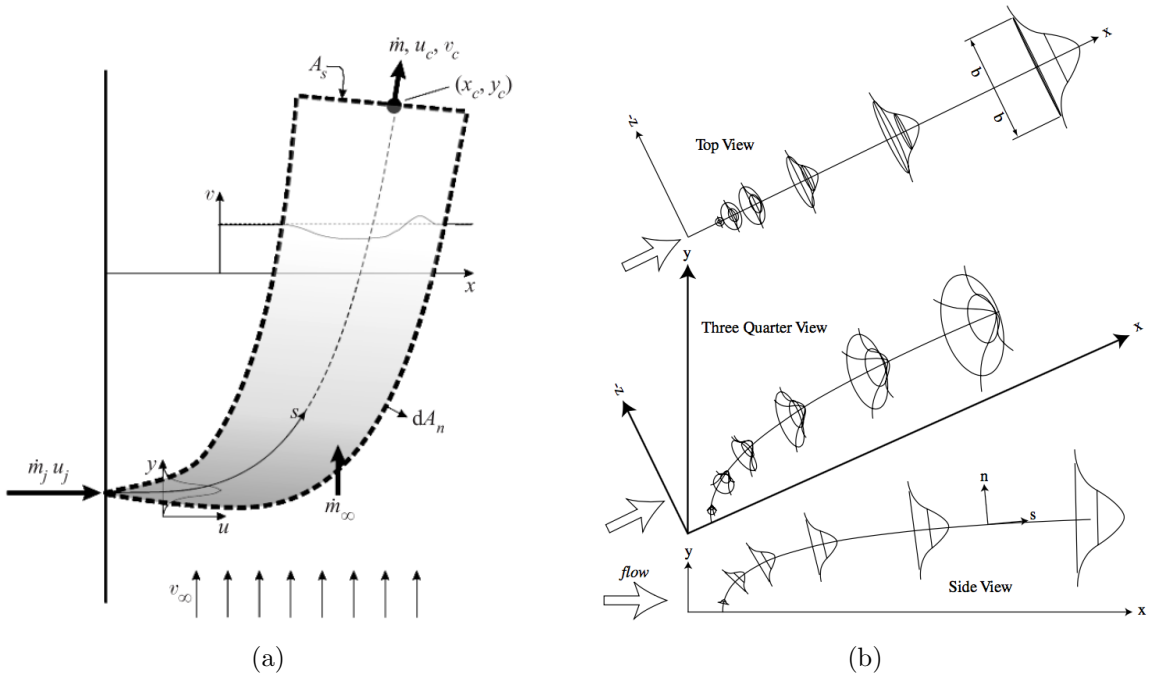

(a) (b)

Figure 3.4: Detailed schematics of the spreading profile for a jet in crossflow by (a) Hasselbrink [4] and (b) Torrez [3].

The model geometry is limited to one specific configuration: that of N independent fuel jets at a single axial location injected into a crossflow of air. Empirical formulas (equations 3.5–3.12) that define the fuel jet spreading and mixing were validated by the experiments of Mungal et al. [4, 51, 52]. The centerline of each fuel jet bends over such that its y-coordinate (y_C) is related to its x-coordinate (x_C) according to [4, 52]:

$$r_u = \left[\frac{\rho_F}{\rho_A} \left(\frac{U_F}{U_A} \right)^2 \right]^{1/2}$$

$$\frac{y_C}{d_F} = c_1 \left(\frac{x_C}{d_F}\right)^{c_2} r_u^{2/3} \tag{3.5}$$

where d_F is the fuel jet diameter and r_u is the fuel jet momentum ratio. The decay of the time-averaged, normalized fuel mass concentration ξ_C along the centerline is given by the far-field scaling law [51, 52]:

$$\xi_C = c_3 \left[\frac{\rho_F}{\rho_A}\left(\frac{U_F}{U_A}\right)^{-1}\left(\frac{x_C}{d_F}\right)^{-2}\right]^{1/3} \tag{3.6}$$

The mean mixture fraction along the centerline $\tilde{f}_C$ is then correlated to the concentration ξ_C, and assumed to be unity in the injected fuel stream and zero in the upstream crossflow:

$$\tilde{f}_C = \frac{\xi_C \frac{W_F}{W_A}}{1 + (\frac{W_F}{W_A} - 1)\xi_C} \tag{3.7}$$

where W is the molecular weight of the fuel or oxidizer. The mixture fraction at any point in the flow field $\tilde{f}$ can be computed by mapping the shortest distance from that point to the jet centerline. Smith et al. [52] showed that the resultant mixture fraction $\tilde{f}(s,n)$ has a Gaussian profile in the direction normal to the curved jet centerline, and is dependent on the radial jet spreading distance (b), a function of the distance along the centerline (s), and the perpendicular distance from the centerline (n):

$$n^2 = (x - x_C)^2 + (y - y_C)^2 + z^2$$

$$\frac{b}{d_F} = c_4 r_u^{2/3} \left(\frac{x_C}{d_F}\right)^{c_2}$$

$$\tilde{f}(s,n) = \tilde{f}_C \exp\left(\frac{-n^2}{2b^2}\right) \tag{3.8}$$

The variance of the mixture fraction $\widetilde{f''^2}$ is a function of the gradient of the mean mixture fraction, according to the Prandtl mixing length relation:

$$\sqrt{\widetilde{f''^2}} = \frac{c_5}{c_4} b |\nabla \tilde{f}| \tag{3.9}$$

Following this, the mean scalar dissipation rate $\tilde{\chi}$ is given by the following formula, where D_T is the turbulent scalar diffusion coeficient, modeled by a relation of the turbulent kinematic viscosity ν_T and the turbulent Schmidt number ($Sc_T = 0.7$):

$$\tilde{\chi} = 2 D_T |\nabla \tilde{f}|^2 \tag{3.10}$$

$$D_T = \frac{\nu_T}{Sc_T} \tag{3.11}$$

$$U_F d_F / \nu_T = c_6 \tag{3.12}$$

These relations determine how the flow mixture properties vary spatially in a three-dimensional field where a fuel jet progresses along its centerline. In particular, the flow field mixture fraction $\tilde{f}$, variance $\widetilde{f''^2}$, and the scalar dissipation rate $\tilde{\chi}$ from equations 3.8–3.10, along with local combustor pressure and temperature conditions derived from equations 1.1–1.7, are necessary to compute the volumetric reaction rate $\bar{\omega_i}$ from the chemical kinetic flamelet tables. Using a flamelet model, the reaction rate of each species is then

$$\dot{\omega}(x, y, z) = \dot{\omega}(\tilde{f}, \widetilde{f''^2}, \tilde{\chi}(f), p, T) \tag{3.13}$$

The profiles of the mixture properties are matched empirically to low-speed experiments, giving rise to the values of constants c_1 to c_5, which are used in this study. Recent investigations [13, 53] have found similar scaling relations for transonic and

supersonic flows, so their use here is appropriate. The quantity $U_F d_F/\nu_T$ is taken as a tunable parameter in the model, and c_6 chosen to correlate with additional mixing suppression due to the high speed flow.

Table 3.3: Experimental constants for jet mixing model, tabulated in [3].

Constant	Experimental Range	MASIV value
c_1	1.2 – 2.6 [51]	1.6
c_2	0.28 – 0.34 [51]	$\frac{1}{3}$
c_3	0.68 – 0.95 [52]	1.3
c_4	0.76 [51]	0.76
c_5	0.0084 – 0.0093 [52]	0.009
c_6		15

3.3 New Additions to the MASIV model to Improve the Finite-Rate Chemistry

To achieve the current goals of computing combustion efficiency and flameout limits, two major additions were made to the MASIV model: the chemistry lookup table was extended to the low pressures associated with high altitude flight, and an advanced interpolation method based on Proper Orthogonal Decomposition (POD) was added. Finite-rate chemistry is included by using a flamelet approach, similar to that of Ihme [54] and Peters [55]. A flamelet lookup table was generated with the Stanford FlameMaster code [54, 56] that solves flamelet equations. For example, a flamelet equation for hydrogen species relates the mixture fraction dissipation rate, diffusion of H_2 mass fraction in mixture fraction space, and the H_2 reaction rate in the following way:

$$\frac{-\chi}{2}\frac{\partial^2 Y_{H2}}{\partial Z^2} = \dot{\omega}_{H2} \tag{3.14}$$

The reaction rate on the right side of equation 3.14 was computed for eight species (H_2, O_2, H_2O, H, OH, O, HO_2, and H_2O_2) and 24 elementary reactions [57]. A chem-

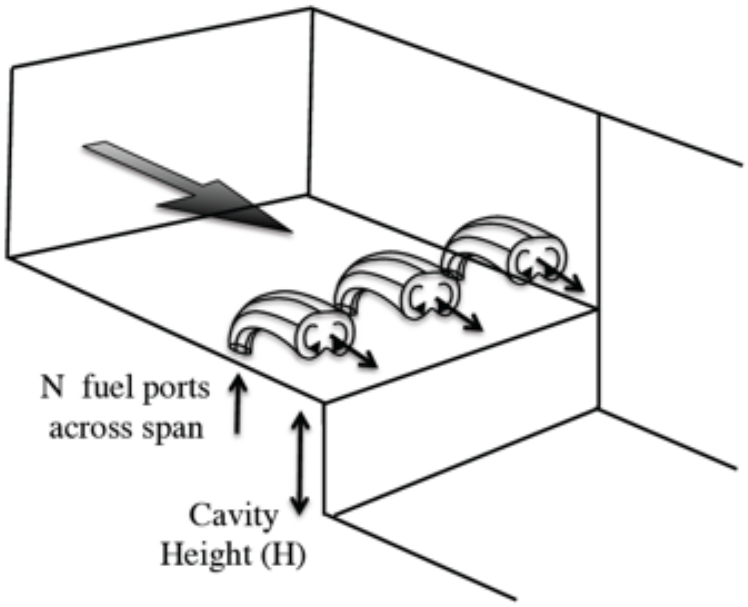

Figure 3.5: Schematic of three of the N = 19 fuel ports that are located across the span of the combustor; above each port is a fuel jet in an air crossflow. Also marked is the height (H) of the flame holder cavity.

istry lookup table was generated that correspond to four discrete combustor entrance static pressures (p_3) of 0.1, 0.32, 1.0 and 3.16 bar and four combustor entrance static temperatures (T_3) of 500, 900, 1300 and 1700 K.

Equations 3.5–3.14 yield 3-D contours of the hydrogen reaction rate ($\dot{\omega}_{H2}$) downstream of each of the 30 wall jets that are drawn in Figure 3.5. Figure 3.6(a) shows some 2-D slices of the computed 3-D profiles. Reaction rate in the upper profile of Figure 3.6(a) is largest just downstream of the wall fuel port, where scalar gradients are large. Reaction rates are smaller for the case of lower static pressure (Figure 3.6(a), lower profile) because the low pressure reduces the Arrhenius reaction rate as well as the fuel-air mixing rate. A mixing and jet scaling model is used for these computations, detailed in [3, 52], and the MASIV model further solves equations 1.1–1.7.

Figure 3.6(b) contains plots of the integrated hydrogen reaction rate ($\overline{\dot{\omega}_{H2}}$). The profiles in Figure 3.6(a) were integrated over each transverse (y, z) plane, using:

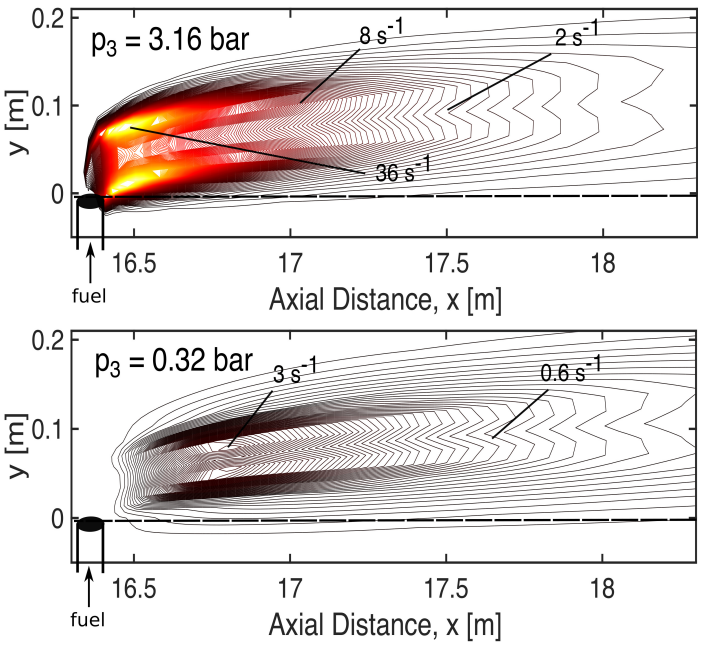

(a)

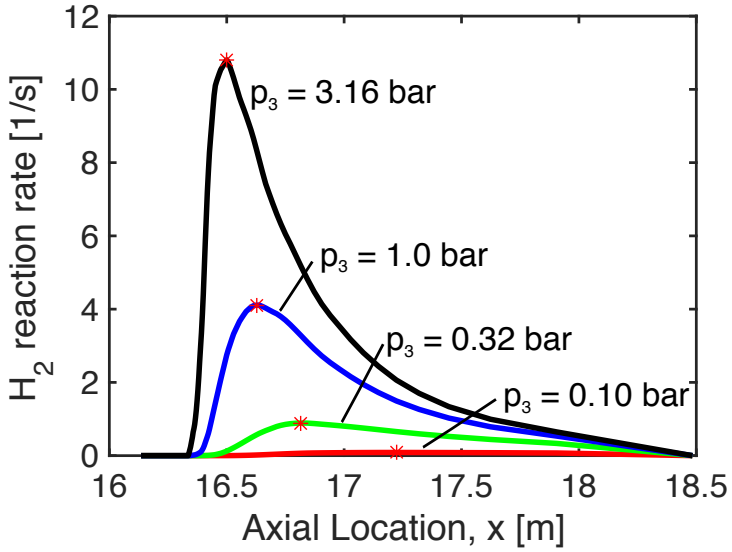

(b)

Figure 3.6: (a) 2-D slices of the 3-D contours of hydrogen reaction rates within one of the fuel jets sketched in Figure 3.5, at two pressure conditions. (b) The 1-D profiles of volumetric hydrogen reaction rate ($\overline{\dot{\omega}_{H2}}$) determined by integrating the contours in (a).i or (a).ii over the y-z plane. Fuel port is at x = 16.4 m. T3 = 900 K, U3 = 2,000 m/s, ER = 0.30.

$$\overline{\dot{\omega}_{H2}}(x) = \frac{1}{A} \iint \dot{\omega}_{H2}(x, y, z)\ dy\ dz \tag{3.15}$$

Thus the integrated hydrogen reaction rate $\overline{\dot{\omega}_{H2}}$ plotted in Figure 3.6(b) is only a function of the stream-wise coordinate x. This integrated reaction rate is required as input into equation 1.7, which determines how rapidly the hydrogen fuel was consumed in the flow direction downstream of the fuel port.

The curve marked $p_3 = 3.16$ bar in Figure 3.6(b) represents the highest pressure in this figure and the peak reaction rate is seen to be much larger than for the lowest pressure condition (0.1 bar). The trend in Figure 3.6(b) confirms the general rule that compression in the inlet should be sufficient to maintain combustor pressure above some baseline value, which is stated in Heiser and Pratt [35] to be about 0.5 atm.

A quantity of interest is the maximum fuel reaction rate (ω_τ), used in equation 3.4 to compute the air velocity at the flameout limit (U_3^*). This reaction rate is given by:

$$\omega_\tau = \frac{[\dot{\omega}_{H2}(x, y, z)]_{max}}{\rho_{H2}} \tag{3.16}$$

$$\rho_{H2} = \frac{\dot{m}_{H2}}{(U_{H2}\ \pi d_F^2/4)} \tag{3.17}$$

The first factor on the right $[\dot{\omega}_{H2}(x, y, z)]_{max}$ corresponds to the maximum values of the contours drawn in Figure 3.6. The density of the injected hydrogen (ρ_{H2}) depends on the equivalence ratio ER, which determines the mass flow rate of hydrogen via the following relation: $(\dot{m}_{fuel}/\dot{m}_{air})\ /\ f_s$. Here, f_s is the stoichiometric fuel-air ratio which is 0.029 for hydrogen. The hydrogen injection velocity U_{H2} is the sonic velocity of hydrogen (1200 m/s) at 300 K. The diameter of each fuel port (d_F) on the MAX-1 vehicle is 3.45 cm.

Combustion efficiency was defined in equation 3.1 to be the fraction of the total mass flow rate of hydrogen that is consumed in the combustor. The unburned hydro-

gen mass flow rate ($\dot{m}_{H2,4}$) in the equation is replaced with ($Y_{H2,4}\ \dot{m}_4$) where $Y_{H2,4}$ is the mass fraction of hydrogen at the combustor exit. The exit mass flow rate $\dot{m}_4$ is replaced with ($\dot{m}_3 + \dot{m}_{H2,inj}$) where $\dot{m}_3$ is the entering air mass flow rate. The fuel-air equivalence ratio ER is defined to be:

$$ER = \frac{\dot{m}_{H2,inj}}{\dot{m}_3\ f_s} \tag{3.18}$$

When the above relations are substituted into equation 3.1, the combustion efficiency becomes:

$$\eta_C = 1 - \left(\frac{Y_{H2,4}}{f_s\ ER}\right)(1 + f_s\ ER) \tag{3.19}$$

At each altitude during the ascent the combustor entrance pressure and temperature are computed, as well as the mass fraction of hydrogen at the combustor exit ($Y_{H2,4}$). This quantity is substituted into equation 3.19, along with the ER required to trim the vehicle, to compute the combustion efficiency.

The flameout limit was computed by employing equations 3.2 and 3.4. First a cavity flame holder of height H is selected for the MAX-1 vehicle. At each altitude along a constant dynamic pressure q_∞ trajectory the vehicle is trimmed in order to compute the angle of attack and equivalence ratio required to produce the necessary thrust. Then, MASIV computes the values of $[\omega_\tau/\omega_\tau^*]$ and U_3 at each altitude. ω_τ is the reaction rate of the fuel for the pressure and temperature at the combustor entrance. ω_τ^* is computed in the same way, but for the measured pressure and temperature at flameout of the Takahashi et al. [41] experiment. These values are input into equations 3.2 and 3.4 and if the computed air velocity U_3 exceeds the critical value U_3^*, then flameout is predicted to occur.

A new method was developed in order to reduce the computational time of the model and improve the interpolation between discrete values in the lookup table.

First a large lookup table was filled with computed values of chemical reaction rates. Secondly, the size of the table is reduced to less than 1% of its original size through a matrix decomposition of the data tables. Additionally, most of the table elements have negligibly small values of reaction rate. The third step was to apply a rapid interpolation method, because the combustor inlet pressure and temperature (p_3, T_3) at each altitude will fall in between the sixteen discrete values that were used to compute the lookup table. Standard interpolation methods were found to be too slow or too inaccurate to handle the multidimensional and occasionally ill-conditioned lookup tables.

Proper Orthogonal Decomposition (POD) is a well-defined method of producing reduced models of complex data sets. In this application, it provides a rapid and accurate way to reduce the size of the lookup table and enable rapid interpolation. The POD method represents the data approximately using a linear combination of basis functions, and only the modes that make the largest contributions are retained. POD methods, as described in references [31–33], are analogous to representing a time-varying voltage as a function of sine and cosine basis functions, along with their associated Fourier coefficients.

The lookup table for the finite-rate chemistry is a multi-dimensional matrix that is called **S**. It contains 93,907,200 elements; each element is a chemical reaction rate (in 1/s, normalized by density) that was computed by solving the flamelet equation 3.14 using the Stanford FLAMEMASTER code. This code considers 24 elementary reactions and 8 species (H_2, O_2, H_2O, H, OH, O, HO_2, and H_2O_2) from the Jachimowski mechanism [57]. The large number of elements in **S** is the product of six parameters; reaction rates are tabulated for each of the 8 species for 4 values of p_3 and 4 values of T_3. For good accuracy, it was decided to consider 201 values of mean mixture fraction, 25 scalar variances, and 146 scalar dissipation rates.

Figure 3.7(a) displays some of the reaction rates stored in **S** for one scalar dissi-

pation rate of 882 s^{-1}. Hydrogen (H_2) reaction rate is plotted as a function of mean mixture fraction and its variance. Notice that there is a small region in the bottom left where the reaction rates are significant (above 900 s^{-1}).

At most of the other locations in Figure 3.7(a) reaction rates are less than 5% of this value. Therefore a new, smaller matrix called ($\tilde{\mathbf{S}}$) then is computed that retains only the small number of significant reaction rates that are seen in the lower left corner of Figure 3.7. Many elements are ignored for which reaction rate is nearly zero. The new matrix $\tilde{\mathbf{S}}$ has less than 1% as many elements as $\mathbf{S}$. To identify and reduce the matrix $\mathbf{S}$, a POD decomposition is performed and only the four largest POD modes are retained. A more complete formulation of this POD approach and its accuracy is detailed in [16].

3.4 Results

We consider two cases: one is the assessment case and the other is the ascent case. For the assessment case, there is no ascent of the vehicle and each of the four governing parameters (p_3, T_3, U_3, ER) is varied independently to provide a basic understanding of their effects on fuel burn and combustion efficiency. For the ascent case all four variables (p_3, T_3, U_3, ER) continuously vary as the vehicle is trimmed along a constant dynamic pressure trajectory. For the ascent case there are many competing tradeoffs that were examined.

3.4.1 Assessment Case: Parameters Varied Independently

Figure 3.8 shows how the hydrogen fuel mass fraction varies in the axial direction within the combustor for different entrance pressures p_3. Equations 1.1–3.12 were solved for values of T_3, U_3 and ER that were fixed at 900 K, 2000 m/s and 0.30, respectively. The hydrogen mass fraction increases sharply at $x = 16.4$ m where the fuel is injected and then it decreases downstream due to chemical reaction. The upper

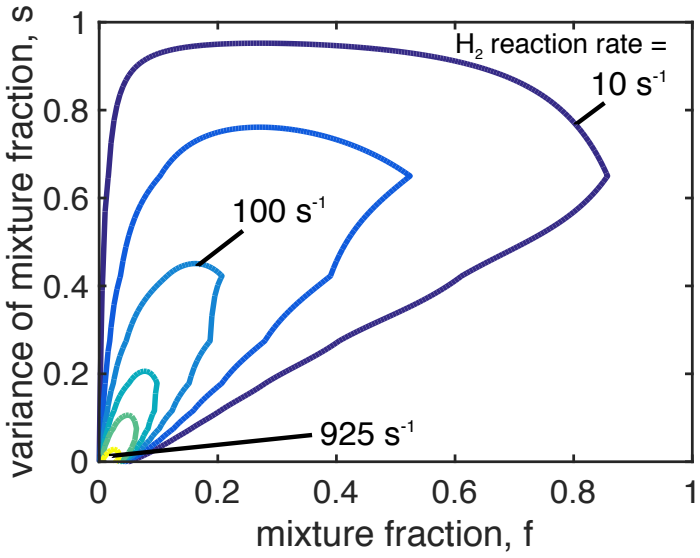

(a)

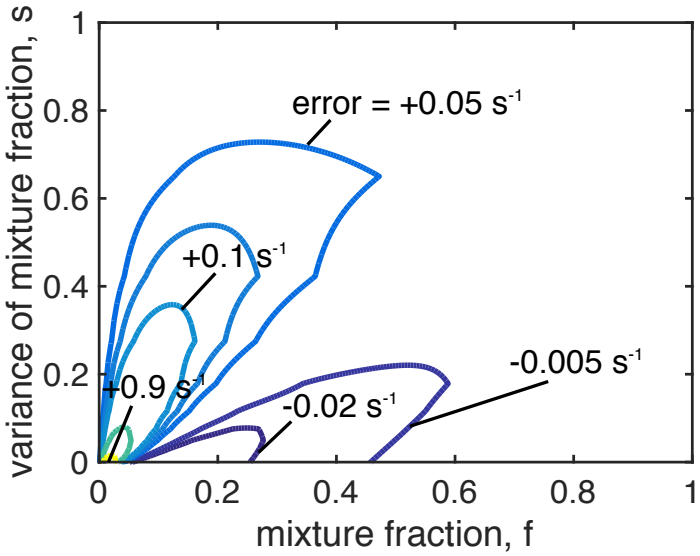

(b)

Figure 3.7: (a) Contours of hydrogen reaction rate ($\bar{\omega}_{H2}/\rho$) computed by the FLAMEMASTER code and stored in the matrix **S**, for one flamelet that corresponds to dissipation rate $\chi = 882$ s^{-1} and $p_3 = 3.16$ bar, $T_3 = 1300$ K. (b) Truncation error of the POD approximation, showing errors of less than 1% by keeping only the four largest POD modes.

curve indicates that little of the fuel is consumed at the end of the combustor ($x =$ 18.5 m) when p_3 is as small as 0.1 bar. Profiles of gas static temperature and static

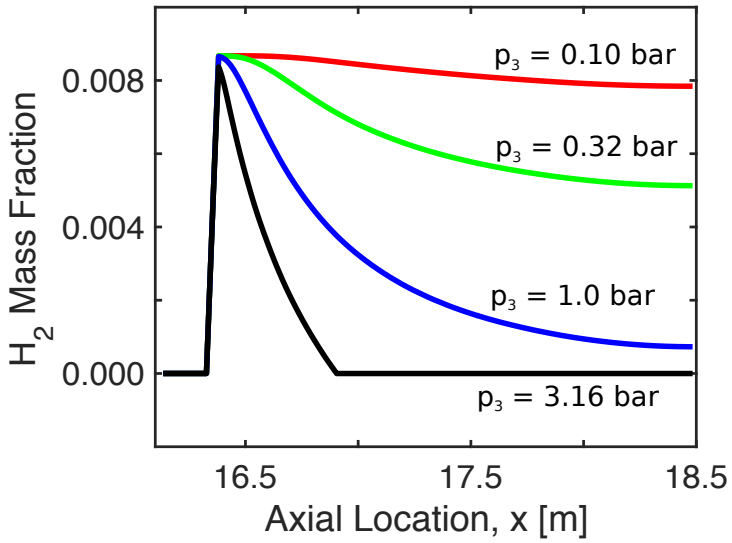

Figure 3.8: Assessment case, no ascent: hydrogen mass fraction profiles for different combustor entrance pressures p_3. T_3 = 900 K, U_3 = 2,000 m/s, ER = 0.3.

pressure have been previously studied [14] are not shown here; both quantities rise initially due to the heat addition from combustion then decrease downstream due to wall divergence. Static pressure rises because heat addition to a supersonic flow drives the Mach number down (towards unity).

Figure 3.9 is a plot of combustion efficiencies determined for the assessment case, measured at station 4 the combustor exit. Profiles computed by solving equations 1.1–3.12 were inserted into equation 3.19. As expected, higher combustion efficiency is achieved by operating at higher combustor entrance pressures and temperatures when ER is held constant. For p_3 less than 0.5 atm, a significant fraction of the hydrogen fuel is not consumed. This finding is consistent with the general understanding in Heiser and Pratt [35] that p_3 should exceed 0.5 atm. The trends in Figure 3.9 are due to two physical processes that control hydrogen reaction rate: mixing and finite-rate chemistry.

The gas velocity U_3 also was increased and, as expected, the combustion efficiency decreased because of the reduced residence time available to complete the mixing and

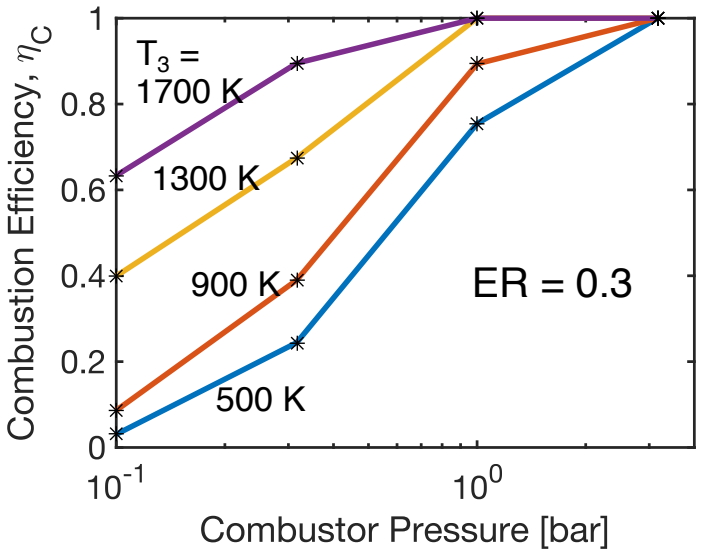

(a)

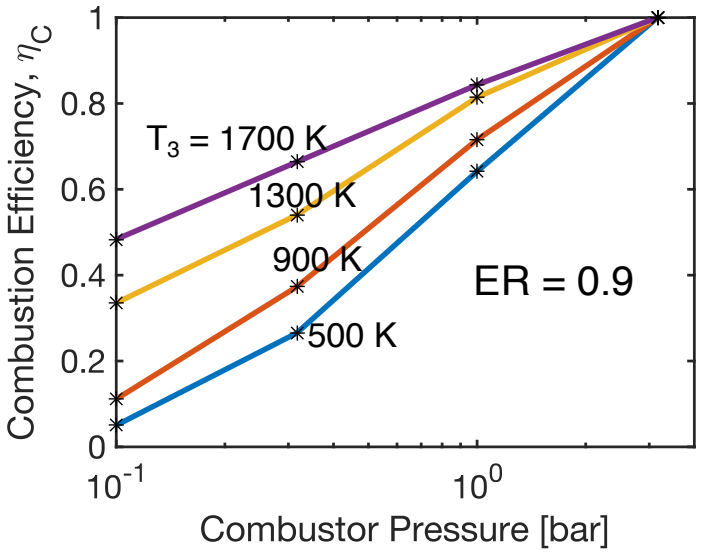

(b)

Figure 3.9: Assessment case, no ascent: combustion efficiencies for (a) $ER = 0.3$ and (b) $ER = 0.9$. $U_3 = 2{,}000$ m/s.

finite-rate chemistry.

The flameout limit was examined for the assessment case and some results are shown in Figure 3.10. The normalized Damköhler number was computed using equation 3.2. Figure 3.10(a) shows that reducing either the pressure p_3 or the temperature

T_3 while keeping U_3 and ER constant, drives the Damköhler number down toward unity, which is the flameout limit. However, Figure 3.10(b) also shows that increasing the equivalence ratio has a strong stabilizing effect, as expected. Propulsion devices often are operated fuel-lean, so smaller values of ER lead to flameout at some lean-limit. For larger ER conditions become closer to stoichiometric and are less likely to flame out.

3.4.2 Ascent Case: Combustor Flow Conditions

Now the ascent case is considered; it is defined by the following constraints. The trimmed MAX-1 vehicle ascends along a path of constant dynamic pressure that is selected to be either $q_\infty = 30$, 50, 70 or 100 kPa. Vehicle acceleration may vary along a trajectory, though in this study $\mathbf{a}$ is fixed at (2 m/s^2) to reduce the dimensionality of the problem. The equivalence ratio is set by the trim requirements at this acceleration, which is low enough to prevent choking of the combustor flow and avoids ram-scram transition for all Mach numbers considered. Figure 3.11 shows how the four governing parameters (p_3, T_3, U_3 and ER) vary as the flight Mach number varies from 5 to 14 along several ascent trajectories ($q_\infty = 30$ to 300 kPa).

Combustor entrance static pressure (p_3) in Figure 3.11(a) decreases as the vehicle ascends along a trajectory. There is some expected tradeoff occurring in this case: one might expect higher Mach numbers to produce strong shocks that raise the static pressure p_3 behind them. However, along a constant q_∞ ascent trajectory M_∞ is proportional to $(p_\infty)^{-1/2}$, and p_∞ varies inversely with altitude (illustrated in Figure 3.3). The decreasing trend of combustor pressure p_3 indicates that the atmospheric pressure conditions dominate the compression tradeoff between p_∞ and flight mach number M_∞. Also note that, p_3 is not directly proportional to p_∞ because the locations of the multiple shock waves in the inlet are changing as M_∞ and the angle of attack change.

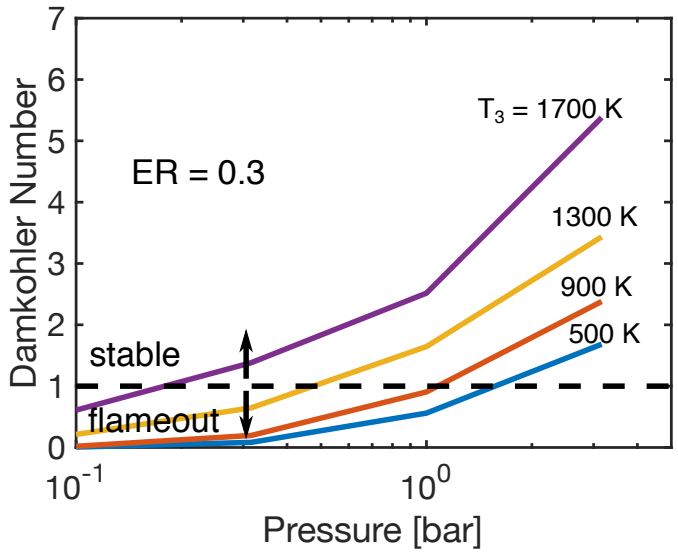

(a)

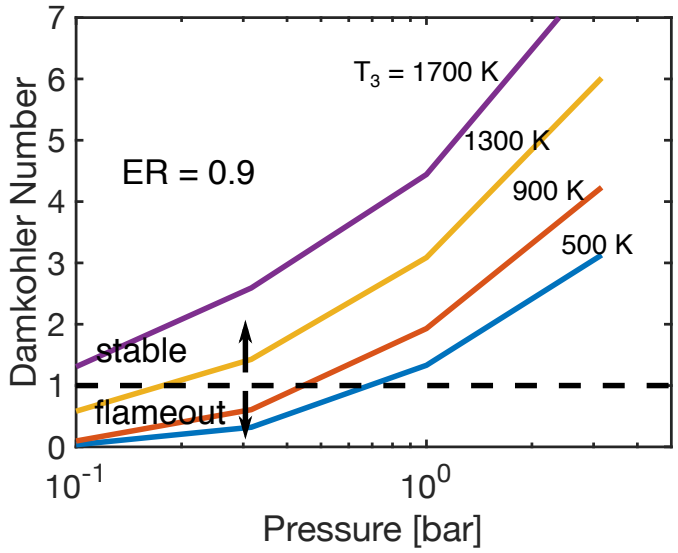

(b)

Figure 3.10: Assessment case, no ascent: flameout occurs below the horizontal line $Da_H = 1$, as defined by equation 3.2. (a) $ER = 0.30$ and (b) $ER = 0.90$. Mach number $M_3 = 2$.

Figure 3.11(b) indicates that the static temperature at the combustor entrance (T_3) increases during the ascent. This is because the increasing flight Mach number raises the stagnation temperature, and more importantly the Mach number M_3 of the

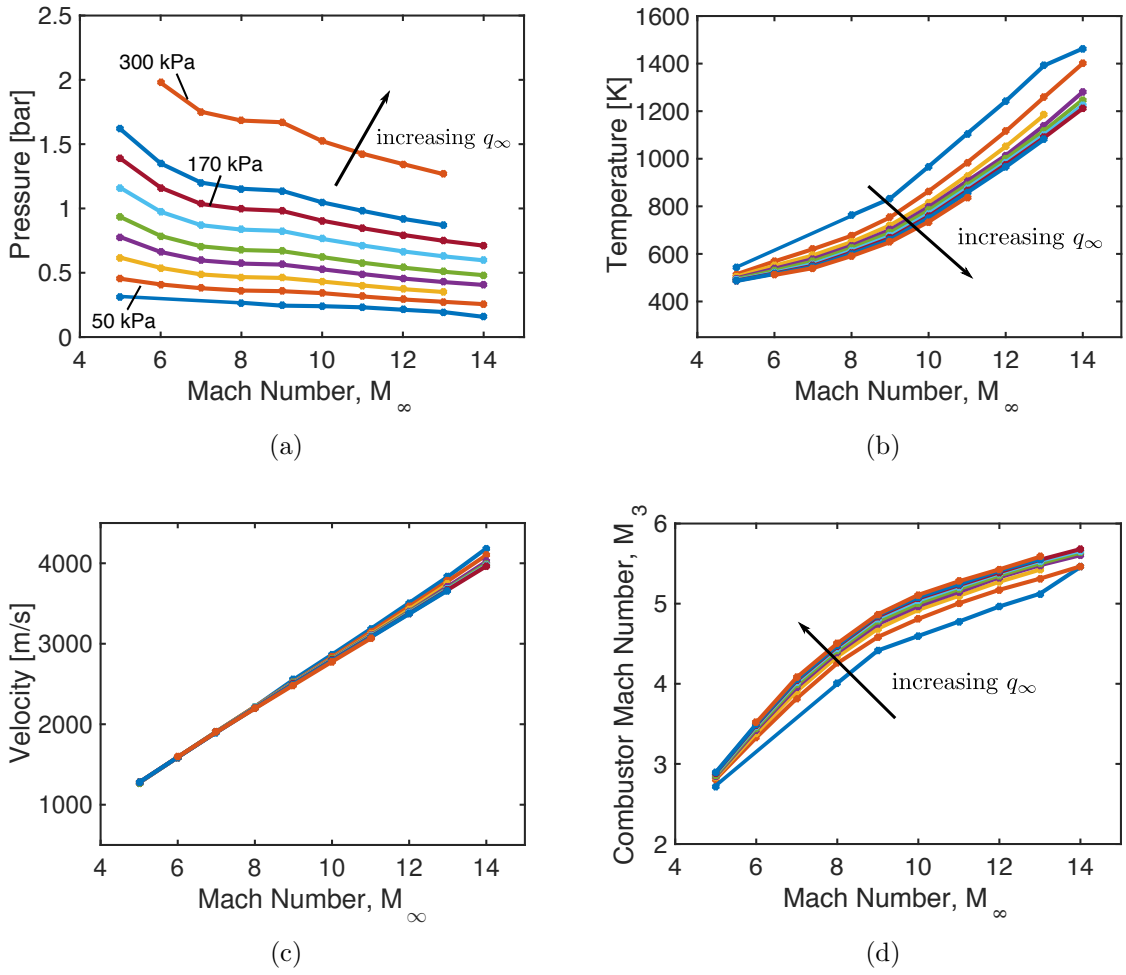

Figure 3.11: Ascent case: for a dynamic pressure (a) combustor entrance static pressure p_3, (b) static temperature T_3, (c) air velocity U_3, and (d) combustor Mach number M_3 versus flight Mach number M_∞.

compressed air entering the combustor, as shown in Figure 3.11(d). Figure 3.11(c) indicates that the entrance air velocity (U_3) also increases with M_∞, primarily due to the increased speed of sound.

An important observation is that Figure 3.12 shows that the equivalence ratio required to trim the vehicle increases during ascent. ER also is much larger along the small q_∞ (30 kPa) trajectory than along the 300 kPa trajectory. The trim requirement introduces interesting constraints. If a small q_∞ trajectory is selected, the vehicle flies at higher altitudes (for a certain M_∞). The ambient gas density is low and

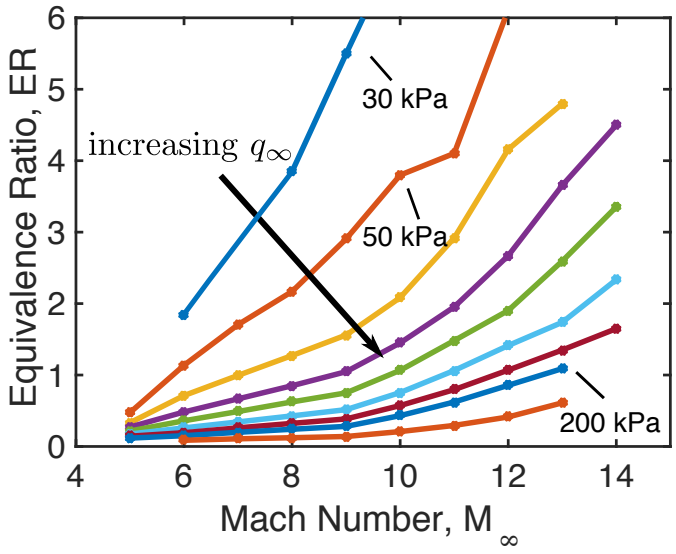

Figure 3.12: Ascent Case: fuel-air equivalence ratio ER versus flight Mach number, for different trajectories of constant dynamic pressure q_∞.

this requires a larger angle of attack to maintain sufficient lift force. Drag tends to vary as the square of the angle of attack, so increased thrust is needed. The low density of the ambient air means that the mass flow rate of air that is captured by the inlet decreases, which would reduce thrust unless ER is increased. Alternatively, the vehicle acceleration is fixed at 2 m/s^2 and if traveling along a high q_∞ trajectory large amounts of air enter the engine. Thus the ER must be reduced, as shown by the lower curve in Figure 3.12.

Noticeably, we observe that at some higher Mach numbers the equivalence ratio rises above unity to meet the thrust requirements. This is a result of two model assumptions handling residence time and incomplete combustion. In the MASIV ROM, fuel burn only takes place in the combustor; the nozzle computations do not contain any combustion chemistry. Secondly, as the crossflow velocity U_3 in the combustor increases, the residence time decreases and the flame length extends beyond the combustion chamber and out of the domain. Thus, even at a fuel-air equivalence ratio of 1 not all of the fuel may be burned and maximum thrust attained. In such case when

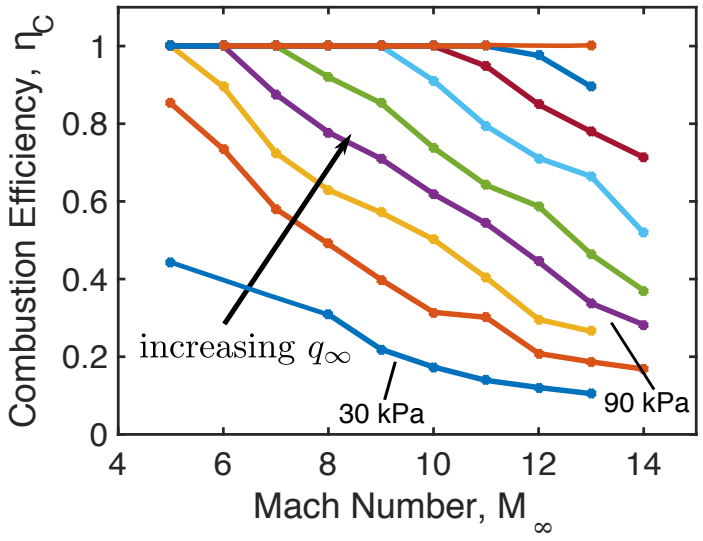

Figure 3.13: Ascent Case: combustion efficiency versus flight Mach number, for different trajectories of constant dynamic pressure q_∞.

$ER > 1$, a greater amount of fuel is dumped into the combustor for the opportunity to burn and produce thrust, but at the cost of reduced combustion efficiency.

3.4.3 Ascent Case: Combustion Efficiency and Flameout Limit

Figure 3.13 shows how combustion efficiency (η_C) varies during the ascent. The computed hydrogen mass fraction at the combustor exit ($Y_{H2,4}$) was inserted into equation 3.19. It can be concluded from Figure 3.13 that it is advantageous to select a trajectory with a large value of dynamic pressure (q_∞) in order to achieve high efficiency. The reason can be deduced from Figure 3.11, which showed that selecting a larger dynamic pressure results in higher pressures (p_3) and much lower equivalence ratios. The higher pressures tend to increase the reaction rates, and the lower ER means that the fuel is rapidly mixed because of the excess air.

A second conclusion deduced from Figure 3.13 is that for each q_∞ trajectory above some Mach number the combustion efficiency steadily decreases during an ascent, as flight Mach number rises from 5 to 14. This appears to be due to offsetting trends

in the combustor conditions. Figure 3.11 showed that during the ascent there is a decrease in p_3 and an increase in U_3, both of which tend to reduce efficiency due to slower chemistry and reduced residence time in the combustor. However, this is partially offset by the increases in T_3 and ER that are shown in Figure 3.11 that tend to speed up the chemical reactions. The pressure and velocity effects dominate the chemistry processes in the combustor, and less and less of the injected fuel is burned as the vehicle accelerates, reducing the overall combustion efficiency.

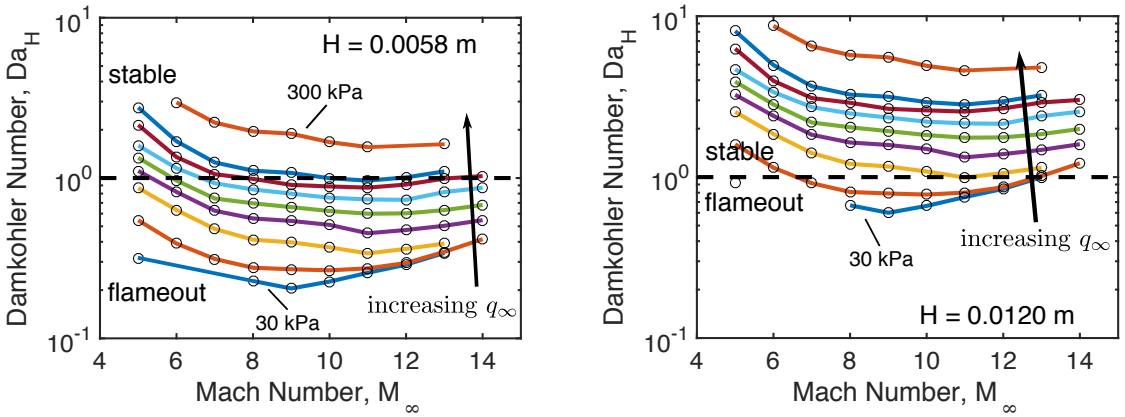

Figure 3.14: Damköhler number computed by MASIV as the MAX-1 vehicle ascends and accelerates along each of the ascent trajectories plotted in Figure 3.2. Dynamic pressure $q_\infty = 30$ kPa is the highest altitude trajectory, while $q_\infty = 300$ kPa is the lowest altitude trajectory. Cavity height varies from (a) H = 0.0058 m and (b) H = 0.0120 m.

The Damköhler number is plotted in Figure 3.14 for two different cavity heights H. In Figure 3.14(b), for most of the ascent trajectories considered the Da_H exceeds unity and so flameout is avoided. An expected result is that the lowest curve in Figure 3.14 corresponds to the lowest q_∞ of 30 kPa. This means that selecting a high dynamic pressure, low altitude trajectory is advantageous in avoiding flameout. A high altitude trajectory subjects the combustor to lower static pressures and a high trimmed ER, reducing combustion efficiency and approaching critically low Damköhler numbers for

a fixed step height H. A low altitude (large q_∞) trajectory provides high pressures, and the engine entrains large amounts of air. Thus a small (lean) ER is required by the trim conditions to prevent excessive thrust and maintain the specified 2 m/s^2 of acceleration.

Figure 3.14 shows that flameout occurs at high altitude (low dynamic pressure q_∞) due to a combination of low ambient pressures, reduced combustor residence time, and inefficient combustion and equivalence ratios at the target trim conditions. It is noted that a constant acceleration trajectory was studied. For ascent or cruise trajectories with a different trim constraint, it is expected that the shape and location of the flameout region will change, and a low altitude flameout may be observed. This might correspond to a Damköhler number "rich limit" as reported in [37], while this study focused only on fuel lean-limit Damköhler number experiments (in Table 3.1). If a high altitude trajectory is selected, Figure 3.13 also shows that the combustion efficiency would be significantly decreased. In some cases, the low efficiency limit is reached before flameout occurs. For fuel, range and overall efficiency considerations, it is desired that combustion efficiency remains high ($\eta_C > 0.90$).

3.4.4 Ascent Case: Operability Limits on a Flight Corridor Map

One goal is to plot operability limits on a flight corridor map, as seen in Figure 3.15. The thin black lines represent constant dynamic pressure trajectories that relate M_∞ to altitude. The upper, curved red line in Figure 3.15 is the flameout limit computed by the MASIV code. Operation above this line leads to flameout due to a combination of low pressures, reduced reaction rates, short residence times, and inefficient ER at the trim conditions. The straight, solid blue line is where the combustion efficiency is $\eta_C = 0.90$. Operation at altitudes above this line is less efficient and not desirable. The subsequent dashed blue lines represent $\eta_C = 0.75, 0.6$ respectively.

It is seen that in Figure 3.15(a) only one acceptable trajectory ($q_\infty = 300$ kPa)

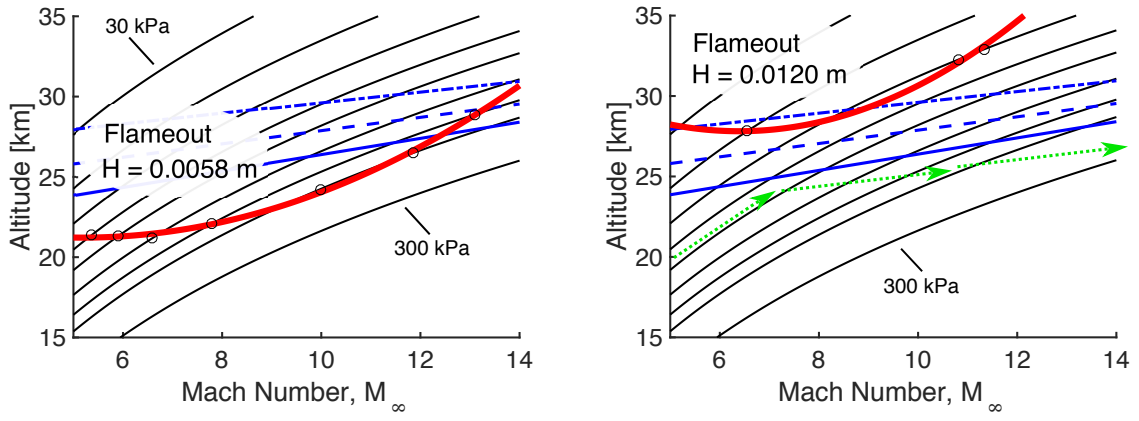

(a) (b)

Figure 3.15: Operability limits due to Flameout (thick curved, red lines) and combustion efficiency exceeding 0.90 (solid, blue line). Cavity flameholder height H is: (a) 0.0058 m and (b) 0.0120 m. The thin solid lines are ascent trajectories of constant q_∞. Vehicle acceleration = 2 m/s^2.

falls outside of the curved red and solid blue lines. One alternative is to increase the flameholder step height H, which shrinks the flamout region, as seen in Figure 3.15(b). The flight corridor is widened and an acceptable trajectory is shown by the green arrows. Even with a larger step height H, at higher flight Mach numbers we approach the loose combustion efficiency limits which tend the acceptable trajectories towards a higher q_∞.

3.5 Discussion of Uncertainty

An advantage of a ROM is that it be run rapidly for thousands of conditions, to estimate trends that occur for a trimmed vehicle ascending along different trajectories. Despite uncertainties introduced by the simplifying assumptions, the computed trends provide understanding, as well as multi-dimensional performance maps that are essential to develop optimization and control strategies. However, two disadvantages of a ROM are its limited range of applicability and the need to quantify uncertainty. The MASIV finite-rate chemistry lookup tables are limited to the fuel

type (hydrogen) for which they were generated. The mixture fraction (fuel mixing) profiles are limited to jets in a cross flow, since they are based on empirical formulas. The flameout Damköhler number is based on an empirical number that is only valid for a cavity-type of flameholder. Our methodology can be modified to account for other fuels, injectors and flameholders, but this has not yet been done.

Uncertainties previously have been shown to be less than 15% for several of the sub-models in MASIV because the selected geometry is simple. However, uncertainties are estimated to be larger for the combustor. Forces were computed using established panel methods; the angles of attack and turning angles are less than 8 degrees so flow separation is not a concern. Panel methods were shown in [58, 59] to predict pressure forces that agree with CFD results to within 10% if turning angles are less than 10 degrees. The engine has a large aspect ratio of 15, and the use of the 2-D Method of Characteristics in the inlet and nozzle were shown in references [2, 14] to compute wall pressures that are within 15% of CFD and experimental results. Only a 1% uncertainty is introduced by the decision to keep only the four largest POD modes to approximate the chemistry lookup table described in Section 3.3. The limitations of these approximations are bound by the parameter ranges of the generated chemistry tables: minimum and maximum pressures of 0.1 to 3.16 bar, and temperatures of 500 to 1700 K, respectively. A previous paper [15] focuses entirely on the uncertainties of the MASIV model.

The largest uncertainties are associated with the combustor, and they are estimated to be less than 30%. It is argued that the empirical formulas that are employed are reasonable for the simple geometry selected, but the uncertainty in the empirical constants c_1 to c_6 is about 30% due to scatter in the data from different experiments [51, 52]. Furthermore, such constants for the empirical scaling relations used in our study are developed from subsonic experiments. Accounting for and modeling more detailed turbulence effects for a jet in a transonic or supersonic crossflow requires

additional consideration – there are no experimentally developed constants at supersonic speeds. The MAX-1 combustor has a simple diverging duct geometry with fuel jets burning in a cross flow. Equations 3.5–3.10 are well-established mixing empirical formulas for jet mixing in a cross flow, based on experimental measurements [52]. The Damköhler number concept is commonly used [37] to correlate flame blowout data, and five sets of measurements in Table 3.1 yield Da^*_{crit} and k_1 values approximating blowout.

The uncertainty and variation of k_1 in some experiments is non-trivial. This provides an indication that there are further parameters beyond the Damköhler correlation of the reaction rate to the diffusion rate affecting flame stability and blowout. The exact measurement of flameout also varied between experiments, reporting either extinguished conditions or incipient flame instability as blowout. Large scatter is found in aggregate experiments using different fuels and mixing structures (cavities, struts), correlating Damköhler number to a defined equivalence ratio [37]. Furthermore, sometimes the conditions of each experiment are not very repeatable or dependable. Quantifying the uncertainty of k_1 is difficult without further experiments; however, in repeating the analysis of this study with a different baseline Da^*_{crit} and k_1 from Table 3.1 we yield the same trends of the flameout region, but with a different minimum cavity step height (a tunable design parameter).

To quantify some of the uncertainty in the combustor computations, previously references [3, 13] compared combustor wall pressure profiles from MASIV to an experiment of identical geometry; the agreement was within 15%. While the combustor uncertainty is larger than desired, the present empirical approach is argued to be justified because CFD codes cannot compute combustion efficiencies or flameout limits with uncertainties less than 30%. Additional measurements could reduce the uncertainty in the empirical constants c_1 to c_6, and k_1. However, the present conclusions have been limited to statements about general trends, and these conclusions are felt

to be accurate.

3.6 Conclusions

In this work, a methodology is presented to compute two operability limits that affect the ascent of a trimmed hypersonic vehicle that is powered by a dual-mode ramjet-scramjet engine. One is the flameout limit and the other is the limit where combustion efficiency drops below 0.90. A reduced-order model (ROM) called MASIV was used that includes finite-rate chemistry tables that are similar to those used in the code FLUENT. A 3-D turbulent mixing model uses empirical formulas for the profiles of mean fuel concentrations in jets in a cross flow. It also applies a conventional assumed-PDF approach to model turbulent mixing. A Proper Orthogonal Decomposition (POD) algorithm was developed to reduce the size of the chemistry lookup table matrix from 93 million elements to less than 1% of this number and speed up the computation. Retaining only the largest four POD modes introduced very small inaccuracy since nearly all of the table elements that were eliminated have negligibly small values, and the original matrices were well-conditioned.

While the ROM results are only approximate, they do successfully predict several measured flameout limit trends. To determine the flameout limits the aerodynamic and thrust forces are computed approximately 1,800 times. That is, for each of nine trajectories twenty altitudes are selected. For each altitude, ten angles of attack are selected to find the one that trims the vehicle. For this type of optimization study a ROM gives a useful first look at the small subset of conditions that should be investigated later using CFD.

For every computation, the vehicle is trimmed at each altitude. To evaluate the model an assessment case was run. For this case there was no ascent and each of the four governing variables (p_3, T_3, U_3 and ER) was systematically varied. The resulting trends were in qualitative agreement with previous experiments. For the ascent case,

multi-dimensional maps were generated by running the MASIV model hundreds of times, through various altitudes, atmospheric conditions, angles of attack and flight trajectories. Each trajectory has a different dynamic pressure. The variation of the angle of attack was necessary to find the trim angle and condition that balances all vehicle forces and moments at an acceleration of $\mathbf{a} = 2$ m/s^2.

From the flight vehicle maps, the two operability limits were computed that define a narrow flight corridor on a plot of altitude versus flight Mach number. The optimum trajectory was identified as the one that has maximum combustion efficiency and avoids the flameout limit. While results of the assessment case (no ascent) were straightforward, the ascent case yielded unexpected results; they arise due to competing effects of four parameters (p_3, U_3, T_3 and ER). During the ascent, the combustor entrance pressure p_3 drops and U_3 increases, which has the adverse effect of tending to slow the chemistry and reduce the residence time. However, ascent also causes T_3 and ER increase, which tends to speed up the chemistry. It was found that a high dynamic pressure (low altitude) trajectory is best to avoid fuel lean-limit flameout. A high-altitude trajectory causes low pressures to occur the combustor, causing slowed chemical reactions and burning in the combustor, lowering the combustion efficiency and approaching conditions for the lean flameout limit.

CHAPTER IV

Design Optimization Approach to Waverider Vehicles

4.1 Introduction

This paper discusses several trade-offs that are recommended to optimize a hypersonic vehicle that has a waverider design and a vehicle-integrated ramjet-scramjet engine. To explain and to quantify these tradeoffs, some results of a reduced-order model are presented. For example, Bowcutt et al. [11, 60–63], explained that it is desirable to achieve sufficiently large values of both thrust-to-drag ratio (T/D) as well as lift-to-drag ratio (L/D). For an ascent trajectory a large T/D provides rapid initial acceleration that reduces the distance needed to lift the fuel against gravity. Large L/D reduces the total amount of fuel required, according to the Breguet range equation. However, it is not possible to achieve the maximum possible values of both T/D and L/D simultaneously. This is because a waverider has properties that fall in-between those of an airplane and those of a rocket. The largest possible T/D occurs for a rocket-like design with a large ratio of frontal area to planform area; in contrast, the largest possible L/D occurs for an airplane-like design with a small ratio of frontal area to planform area.

Another observation by Bowcutt et al. [11, 60–63], Bolender and co-workers [8, 64–

66] and Dalle et al. [1, 12] is that the design rules that optimize only the propulsion system are incomplete for two reasons. First, these "propulsion-oriented" ideas ignore the additive drag that occurs when the engine is installed. Secondly, they ignore the trim requirements. For example, they assume that the fuel-air equivalence ratio is a free parameter when in reality it is constrained to be the value that produces the correct thrust to overcome the vehicle drag and to provide the necessary acceleration. The results presented in this paper go beyond "propulsion-oriented" ideas and they quantify a waverider that is trimmed at each point along an ascent trajectory. In this way we can discuss more general "vehicle-integration" design rules, and we point out where these rules contradict some unrealistic "propulsion-oriented" ideas.

Vehicle-integration ideas are important because the entire undersurface of a waverider contributes to the functions of propulsion, aerodynamics, and stability/control. Figure 4.1 shows that the forebody serves as part of the inlet compression system. A high compression ratio is desirable for the engine but it produces a nose-up moment that is not desirable for vehicle stability. The aftbody serves as part of the nozzle expansion system and it often contributes a nose-down moment. The propulsion system, in turn, supplies a fraction of the required vehicle lift, especially if it is canted at an angle with respect to the flight direction. The engine in Figure 4.1 is mounted on the underside so it contributes a nose-up moment.

Such tight design integration challenges the very design process, and the tools required to execute the design process. The highly integrated nature of hypersonic vehicles, combined with their non-linear behavior, render conventional techniques inadequate. It is argued that both high-fidelity and reduced-order simulations are useful and complement each other. The results of Bowcutt et al. [11, 60–63] were based on many high-fidelity CFD simulations and experiments. Another approach was taken by AFRL researchers who require a reduced-order, control-oriented model. Reduced-order models cannot replace high-fidelity CFD, but they typically can be

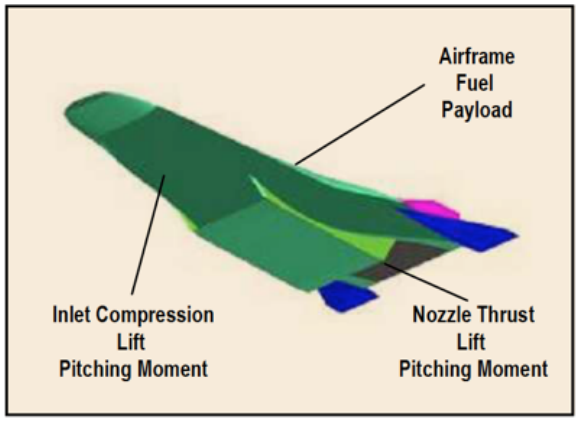

Figure 4.1: Close integration of vehicle components is required for hypersonic lifting body configurations.

run 10,000 times in a day on a few processors in order to map out the design space. For example, suppose that ten ascent trajectories, each with a different dynamic pressure (q_∞), are considered on a plot of altitude versus flight Mach number. Along each trajectory 100 altitudes are considered. At each altitude, the trim angle of attack is determined by selecting ten angles to find the one that balances forces and moments. This computation requires vehicle lift, drag and thrust to be computed 10,000 times. A reduced-order model can be useful in helping to identify a narrow range of conditions that are of most interest, and thereby reduce the number of CFD runs.

A reduced-order model of a trimmed hypersonic vehicle was reported in 2007 that is called the AFRL Bolender and Doman [8] model. It is a first-principles approach because it is based on the conservation equations for mass, momentum and energy. More recently it has evolved into the MASIV model [1–3, 12–17, 67–69] and it has been used for optimization. One paper [12] reports an ascent trajectory that minimizes the fuel required. Another paper [1] describes a trajectory that best avoids engine unstart, while computed trajectories in [17, 19] identify regions of flameout. The inlet geometry also was optimized [2, 67]. Sub-models have been added to compute complex inlet shock wave interactions [2], finite-rate combustion chemistry, 3-D fuel-

air mixing [3] and thermal choking [13]. MASIV also predict three operability limits: ram-scram transition [13], engine unstart [1] and engine flameout [17]. Prior to 2007 there were vehicle computations that were reported by Starkey and Lewis and others [9, 10, 70–82]. However, only MASIV includes inlet shock wave interactions, finite-rate combustion chemistry, 3-D fuel-air mixing and engine unstart. In addition, previous work has led to propulsion-oriented ideas, such as those reported by Heiser and Pratt [35] and by Billig and colleagues [83–87]. They did not consider the constraints imposed by the requirement that the vehicle must be trimmed.

The following Section 4.3 lists some previous propulsion-oriented design rules. Section 4.2 explains the need to optimize thrust/drag and lift/drag ratios, but tradeoffs are needed to optimize both. In Section 4.4 some general vehicle-integration design rules are discussed that sometimes conflict with conventional propulsion-oriented rules. Section I is a summary of the MASIV reduced-order model and Section 4.4 presents MASIV results in order to assess various design rules. To investigate the tradeoffs, MASIV computational runs were made to generate multidimensional maps of T/D, L/D and other parameters for the case of a waverider ascending along a $q_\infty = 100$ kPa trajectory. Then an optimization code was developed to determine how to vary parameters along the constant-q trajectory in order to minimize the total fuel required for ascent. The poles of the flight dynamics equations are presented to describe how the vehicle stability is reduced as it ascends.

4.2 Background: Importance of L/D and T/D for Waveriders

There are five classes of hypersonic vehicles; one is an airbreathing accelerator for space access which is the focus these studies. The other classes are: cruise vehicles (such as cruise missiles), gliders for re-entry (such as the Space Shuttle), re-entry capsules that have no wings to act as lifting surfaces, and rockets. It is necessary to achieve sufficiently large values of the thrust-to-drag ratio (T/D) and the lift-to-drag

ratio (L/D) in order to meet acceleration and range goals. One goal is to minimize the mass of fuel required for ascent, another is to maximize the vehicle acceleration (T/D) along a trajectory (and thus minimize flight time). Reducing drag is a primary objective, and any lift that is associated with angle-of-attack comes with a significant wave drag penalty. If some of this lift cant be replaced with other sources, such as spillage lift or lift due to engine cant as described below, fuel consumption can be further improved. Increasing the T/D also reduces fuel requirements, up to a certain point. Increased thrust comes with a fuel penalty, but some of the penalty can be offset by selecting a large initial acceleration (i.e., a large initial T/D). This minimizes the distance that the fuel is lifted against gravity, and the concept is the basis for booster rockets. Therefore, for a typical mission that requires acceleration, cruise and glide, the values of L/D and T/D must be optimally traded.

To understand the parameters that affect thrust, lift, drag and their ratios, the following equations are useful. First note that T/D is proportional to the vehicle acceleration (a), based on equation 4.1, which is Newton's Law after weight $(\mathcal{W})$ is set equal to lift:

$$\frac{T}{D} = 1 + \left(\frac{L}{D}\right)\left(\frac{a}{g}\right) + \left(\frac{L}{D}\right) + \sin(\gamma) \tag{4.1}$$

The gravitational constant is (g) and (γ) is the ascent angle. For simplicity, consider a vehicle whose lift is provided by a supersonic diamond-shaped airfoil. The following relation 4.2 provides a formula for the (L/D) factor that appears in 4.1. This formula applies in the supersonic range where the Prandtl-Glauert scaling is valid.

$$\frac{L}{D} = \frac{C_L}{C_D} = \frac{4\alpha(M_\infty^2 - 1)^{-1/2}}{C_{D,0} + 4\alpha^2\ (M_\infty^2 - 1)^{-1/2} + A_1\ (t/c)^2\ (M_\infty^2 - 1)^{-1/2}} \tag{4.2}$$

The denominator of equation 4.2 is the sum of the drag coefficients due to viscous

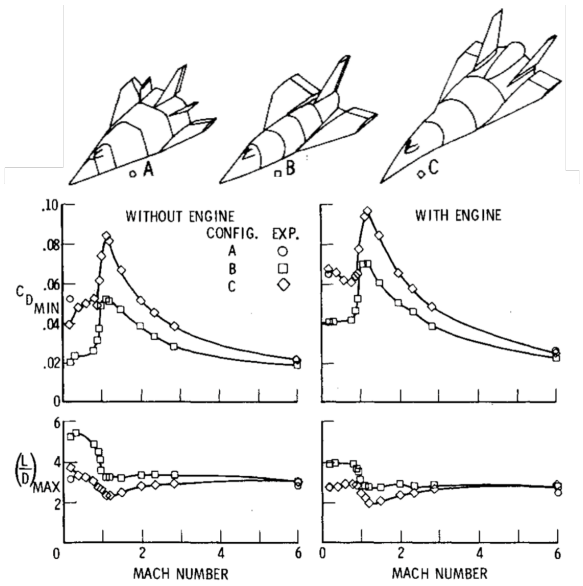

Figure 4.2: Variation of $C_{D,0}$ and $(L/D)_{\max}$ with Mach number for three variants of a NASA Hypersonic Research Aircraft concept, from [5].

drag ($C_{D,0}$) and wave drag. Wave drag depends on both the angle of attack and the airfoil thickness (t/c), where c is the chord length [88, 89]. A_1 is a tunable constant. White [90] explains that $C_{D,0}$ for supersonic flow over an adiabatic flat plate is proportional to $M_\infty^{-2}\,\mathrm{Re}_L^{-n}$. The exponent is 1/2 if the boundary layer is laminar and 1/5 if turbulent, based on the Van Driest II correlation. Finally, the angle of attack (α) appears in equation 4.2, and it is given by equation 4.3.

Now some previous measurements are presented for hypersonic waveriders in order to show that the measurements display general trends that are similar to those that are predicted by equations 4.1-4.2. Figure 4.2 indicates that measured values of $(L/D)_{\max}$ for hypersonic waveriders [5] can be increased if the Mach number is decreased. This trend is in agreement with equation 4.2. It is seen that as the Mach number increases up to six, measured values of $C_{D,\min}$ decrease while $(L/D)_{\max}$ decreases to a nearly constant value. This decrease in $C_{D,\min}$ with increasing M_∞ is consistent with White's adiabatic flat plate formulation.

Figure 4.3 contains additional values of $(L/D)_{\max}$ that were plotted by Bowcutt et.

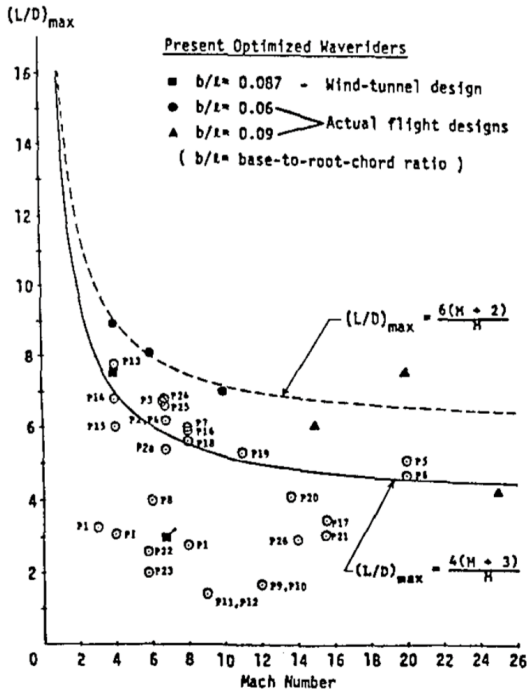

Figure 4.3: Increased Lift-to-Drag ratio provided by a waverider geometry (upper curve) compared to conventional configurations (lower curve), as Mach number is increased [6].

al. [6] for waveriders and conventional hypersonic designs. Both curves of $(L/D)_{\max}$ decay and plateau as expected. Viscous optimized cone flow waveriders (upper curve) were generated that exceeded the classical or Kuchemann [91] L/D barrier (lower curve).

Now consider how the angle of attack varies during an ascent. The lift coefficient for a diamond-shaped airfoil is the numerator of equation 4.2, which is set to $\mathcal{W}/(q_\infty S)$ such that the lift force balances the weight, and S is the planform area. Solving for α leads to:

$$\alpha = \frac{\mathcal{W}}{4\ q_\infty S}(M_\infty^2 - 1)^{1/2} \tag{4.3}$$

Equation 4.3 indicates the benefit of selecting a high dynamic pressure (q_∞) trajectory. High q_∞ is seen to lead to a small angle of attack and this reduces the wave drag

term in the denominator of equation 4.2 which scales as α^2. Equation 4.3 also shows that angle of attack will tend to increase during the ascent due to the $(M_\infty^2 - 1)^{1/2}$ factor. However, this will be partially offset by the decrease in weight ($\mathcal{W}$) caused by fuel consumption. Thus α should increase during ascent if the specific impulse of the engine is so large that the weight loss is comparatively modest.

It may be desired to maintain an angle of attack during ascent that ensures that (L/D) is close to $(L/D)_{\max}$ at all times, because the Breguet range formula indicates that this helps to minimize the fuel requirements. To do so, one cannot require that the dynamic pressure (q_∞) remain constant. Instead, to operate near $(L/D)_{\max}$, the derivative of equation 4.2 with respect to α is set equal to zero. This equation is solved for α, which is then inserted into equation 4.3. Solving for q_∞ yields:

$$q_\infty = \frac{\mathcal{W}}{4S}\, F \tag{4.4}$$

where the function F is given by:

$$F = \left[M_\infty^2 - 1\right]^{1/2} \left[C_{D,0} + A_1\, (t/c)^2\, (M_\infty^2 - 1)^{-1/2}\right]^{-1/2} \left[4\, (M_\infty^2 - 1)^{-1/2}\right]^{1/2} \tag{4.5}$$

Equation 4.4 shows that to stay at the angle of attack that yields maximum (L/D), any decrease in the weight due to fuel consumption should be offset by operation at a smaller q_∞ (i.e. higher altitude) for a given Mach number.

Another parameter to be optimized is the wing planform area (S). Larger values of S reduce the angle of attack required (as shown by equation 4.3 and thus there is less wave drag. However, a larger wing area has more viscous drag. If it is desired to operate at high q_∞ to capture sufficient air into the engine, the value of α will be small. Thus α will be smaller than the value that produces maximum L/D. For a high dynamic pressure trajectory, the wave drag becomes less important; it becomes

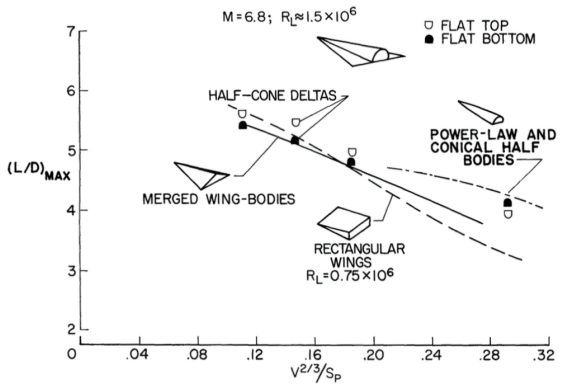

Figure 4.4: Trend in maximum lift-to-drag ratio with one measure of configuration fineness ratio, found in [7].

necessary to minimize $C_{D,0}$ by selecting a relatively small wing area. A recommended design approach to reduce the total drag is to simultaneously increase q_∞ and to reduce planform area S, as shown through the formulation of equation 4.4. This will allow α to be large enough to equal the value that provides maximum L/D, while viscous drag is reduced due to the reduced planform area of the wings. In other words, a vehicle designed for high (L/D) might have greater drag operating at a lift coefficient below the design value than a vehicle designed for low $C_{D,0}$ at the same reduced lift coefficient.

Another geometric factor that affects $(L/D)_{\max}$ is the fineness ratio that is defined to be $(\mathcal{L}_v/W_{\text{eff}})$. $\mathcal{L}_v$ is the vehicle length and W_{eff} is its effective width. Kuchemann [7] multiplied both the numerator and the denominator of this ratio by $(W_{\text{eff}})^2$ and took the $2/3^{\text{rd}}$ root to form the new ratio $(\mathcal{V}^{2/3}/S)$ aptly named Kuchemann's tau parameter (tau). $\mathcal{V}$ is the vehicle volume and S is the planform area. An airplane has a small value of τ because of its large planform area while τ is large for a rocket; τ is a measure of vehicle volume-carrying capacity relative to its lifting surface area. Figure 4.4 is a plot from studies by Fetterman et. al. [7] that indicates that $(L/D)_{\max}$ decreases, as expected, when τ increases and the vehicle becomes more slender and rocket-like.

4.3 Previous Propulsion-Oriented Design Rules

Heiser and Pratt [35] and Billig et al. [83–85] have presented ideas that are "propulsion-oriented"; they describe how the throttle setting and the inlet area affect the engine thrust. However, since they only consider the engine, their analysis is not "vehicle-oriented". Billig had suggested that if the engine is mounted underneath the vehicle, the bow shock wave should intersect the leading edge of the engine cowl when the flight Mach number reaches its maximum value. Figure 4.5 illustrates this condition. This condition insures that there is no spillage at the maximum Mach number. At lower Mach numbers the angle of the bow shock is larger, so spillage occurs. During ascent the capture area (A_C) becomes larger as M_∞ increases and the bow shock angle decreases. This is desirable because of the difficulty in capturing sufficient air at the maximum speed. Note that air mass flow rate ($\dot{m}_A$) equals $\rho_\infty U_\infty A_C$ and the dynamic pressure (q_∞) is $\frac{1}{2}\rho_\infty U_\infty^2$. Rearranging these two formulas leads to:

$$\dot{m}_A = \frac{2q_\infty A_C}{U_\infty} \tag{4.6}$$

Along a constant dynamic pressure trajectory it is desirable for the capture area to increase because this helps to offset the increase of U_∞ in the denominator of equation 4.6. As seen in Figure 4.5, the capture area at the maximum flight Mach number (M^*) is:

$$A_C^* = bW_e \tag{4.7}$$

where b is the forebody height and W_e is the width of the inlet. The superscript * is used to denote conditions at the maximum flight Mach number M^*.

Now consider the forebody height that is required to capture sufficient air at the maximum flight speed. To simplify this discussion it is assumed that the lift

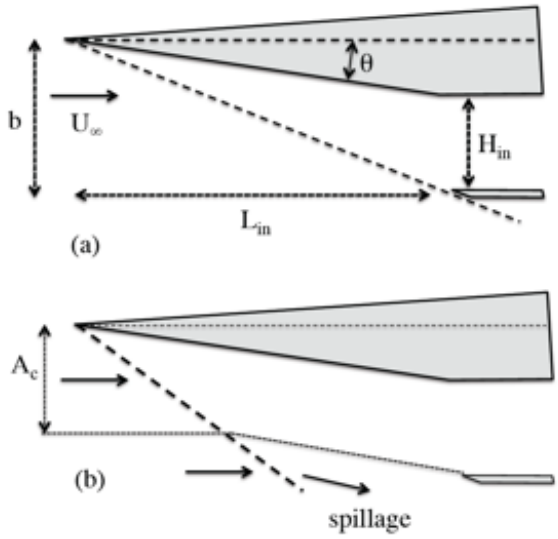

Figure 4.5: (a) Bow shock intersecting engine lip at maximum flight Mach number M^*. (b) Lower speed operation with air spillage.

(L) approximately equals the vehicle weight ($\mathcal{W}$). The specific impulse is defined to be $\mathcal{T}/(\dot{m}_F g)$ where $\mathcal{T}$ is thrust and ($\dot{m}_F$) is the fuel mass flow rate. The fuel-air equivalence ratio (ϕ) is defined to be $(\dot{m}_F/\dot{m}_A)/f_s$ where f_s is the stoichiometric fuel air ratio. To simplify the discussion of propulsion-oriented ideas, in this section (only) it is assumed that the quantities $C_{D,0}$ and $(t/L)^2$ in equation 4.2 are sufficiently small so that the drag is primarily due to the wave drag term in the denominator of equation 4.2. With this approximation, it follows that:

$$D = \mathcal{W}^2 \ (q_\infty S)^{-1} \ (A_2/A_1^2) \ (M_\infty^2 - 1)^{1/2} \tag{4.8}$$

Now consider flight at the maximum Mach number M^*. The required forebody height (b) is determined from equation 4.7 after the capture area is replaced using equation 4.6. The air mass flow rate then is replaced by applying the above definitions of equivalence ratio and specific impulse to yield:

$$b = \left(\frac{T}{D}\right)\left(\frac{1}{\phi^*}\right)\left(\frac{1}{W_e}\right)\left(\frac{\mathcal{W}^{*2}}{\rho_\infty^{*\frac{1}{2}} q_\infty^{3/2} S}\right)\left(\frac{1}{I_{sp}^*}\right)\left(\frac{1}{\sqrt{2} f_s g}\right)\left(\frac{A_2}{A_1^2}\right)\left(M_\infty^2 - 1\right)^{\frac{1}{2}} \tag{4.9}$$

Note that forebody height b is proportional to $\mathcal{W}^{*2}$; if the final weight $\mathcal{W}^*$ of the vehicle is doubled, the lift and angle of attack are doubled so the drag and thrust forces must become four times larger. Thus the forebody height also must be made four times larger to capture sufficient air. If the specific impulse becomes smaller, it is seen that the forebody height must be made larger in order to capture more air; the fuel flowrate also must be increased to maintain the same ϕ. If a trajectory with a larger dynamic pressure q_∞ can be tolerated by the structure, the required forebody height will be smaller.

The quantity (T/D) to be inserted into equation 4.9 is given by equation 4.1 and is proportional to vehicle acceleration. Thus for a desired acceleration and ascent angle, equation 4.1 determines the required thrust-to-drag ratio that is to be inserted into equation 4.9 to compute the forebody height. For a typical acceleration between 0.25 and 1.0 **g**'s, the thrust-to-drag ratio will have a value of approximately three.

Now consider the inlet height ($\mathcal{H}_{in}$) and the inlet lip x-location ($\mathcal{L}_{in}$) that appear in Figure 4.5. At the maximum flight Mach number the bow shock intersects the engine lip so the capture area equals (bW_e) and the engine air mass flow rate is ($\rho_\infty U_\infty b W_e$). Therefore the air flow rate does not depend on the inlet height ($\mathcal{H}_{in}$) when the vehicle flies at the maximum flight speed. At lower speeds the air flow rate does depend on $\mathcal{H}_{in}$ due to spillage. The value of $\mathcal{H}_{in}$ should be selected to provide the desired contraction ratio ($A_C/\mathcal{H}_{in}$) such that the pressure supplied to the combustor exceeds 0.5 atm in order to maintain sufficient combustion efficiency. Conservation of mass [92] requires that:

$$p_{0_\infty}\ (A^*_\infty/A_\infty)\ (bW_e) = p_{0_2}\ (A^*_2/A_2)\ (bW_e) \tag{4.10}$$

where A^*_2 is the area required to choke the flow at the isolator inlet. Equation 4.10 should be solved to determine the inlet height $\mathcal{H}_{in}$. First the quantity (A^*_∞/A_∞) is determined using compressible flow tables for the maximum Mach number M^*. The value of p_{0_2} next is computed from a table of the recovery factor (p_{0_2}/p_{0_∞}), which is typically 0.5 at M^* equal to nine [2]. This recovery factor can be estimated assuming that the inlet contains only three non-interacting shock waves, and the strength of the bow shock is determined from the forebody turning angle θ. Then the desired combustor inlet pressure p_2 is *selected* to be typically 1.0 atm. This provides the ratio (p_2/p_{0_2}) which yields a value of M_2. Compressible flow tables then provide (A^*_2/A_2), which is the remaining unknown in equation 4.10. The engine height $\mathcal{H}_{in}$ also should be designed to be large enough to prevent excessive spillage at low speeds.

The x-location of the engine inlet lip $(\mathcal{L}_{in})$ is suggested by Billig [84] to be set by the geometric constraint that the bow shock angle (β^*) causes the shock to intersect the inlet lip at $M_\infty = M^*$, so:

$$\mathcal{L}_{in} = \mathcal{H}_{in}\ \ [\tan(\beta^*) - \tan(\theta)]^{-1} \tag{4.11}$$

The total deflection angle is $(\theta + \alpha^*)$ but here α^* is assumed to be small compared to θ.

Heiser and Pratt [35] impose other constraints in the propulsion-oriented approach. They require that the burner entrance temperature (T_3) be less than 1670 K. Since T_{0_3} equals T_{0_∞} and free stream static temperature T_∞ is in the range of 216 K, their constraint requires M_3 to exceed 0.38 M_∞ in scram mode. This requires M_3 to be 4.6 when flying at Mach 12, so the residence time of the air in the combustor will be very small. The design of the combustor proposed in Heiser has a constant area section

with a length-to-height ratio (l/h) of approximately 5, followed by a diverging section having a similar (l/h) of 5. The combustor divergence angle should be approximately 4 degrees. Wall divergence is needed to provide operating margin, as explained by Heiser and Pratt [35]. Upstream of the combustor Heiser recommends an isolator having a length-to-height ratio (l/h) that exceeds 10. The nozzle exit area should expand the exhaust so that the nozzle exit static pressure equals the ambient pressure at a flight Mach number that is halfway between the minimum and maximum desired values of M_∞. The values of the fuel-air equivalence ratio (ϕ) that have been suggested by previous propulsion-oriented analyses cover the wide range from 0.5 to 2.0 [35, 83–85]. Billig recommends that ϕ should increase linearly from 0.5 to 2.0 [84], because he estimated that only half of the fuel will burn at the highest altitudes.

4.4 Development of Vehicle-Integration Design Rules

The previous sections explained that there are complicated tradeoffs that must be balanced in the attempt to operate near the optimum values of T/D and L/D. Computations of all of the vehicle forces and moments for thousands of cases are required to explore the effects of varying chord, span, engine width, altitude and Mach number, while trimming the vehicle at each conditions. Since CFD is not practical, the reduced order MASIV model was used. A total of 252 cases were run for 84 different geometries (varying chord, span, engine width) and three values of acceleration. The geometries include the "airplane-like" case in Figure 4.8 and the "rocket-like" case in Figure 4.9. Performance is quantified by the computed L/D, T/D, angle of attack α and elevon deflection angle δ. For the cruise condition tests, the thrust-to-drag ratio is not reported since it is computed to be unity to within 3%.

Consider the hypersonic waverider that is shown in Figure 4.6. This vehicle, called MAX-1 [12], is the default and prototypical design for this analysis. The geometric measurements and the vehicle profile (2-D) are shown in Figure 4.6(a); additional

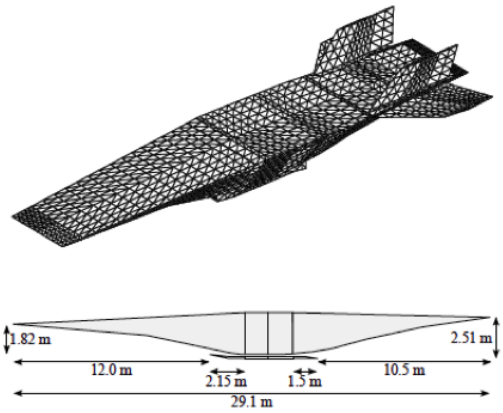

(a) MAX-1 vehicle dimensions

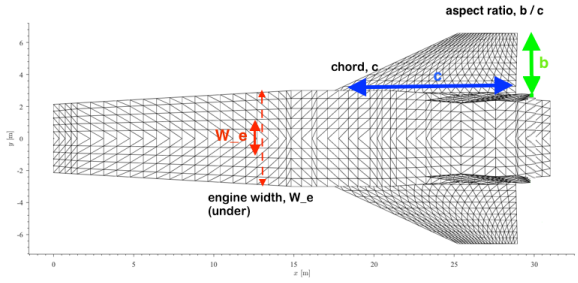

(b) Indepenent vehicle design parameters

Figure 4.6: (a) Reference MAX-1 vehicle and flow path dimensions. Engine width is 2.143 m. (b) Schematic top-view of the independent variable vehicle parameters examined.

geometric parameters are sketched in Figure 4.6(b). The design parameters of the default MAX-1 vehicle are referred to as reference values, to provide a basis for comparison and performance analysis. The engine width $W_{e,ref}$ is 2.143 m (corresponding to a capture area ratio of $A_{capture}/A_{frontal} = 0.5$), root chord length c_{ref} is 0.2 (20% of vehicle length, 6.1 m), elevon aspect ratio b_{ref} is 1.5, elevon sweep Λ_{ref} is 0.6 radians, and taper ratio λ_{ref} is 0.6.

4.4.1 The 84 Waverider Geometries Considered

In order to assess variational waverider designs on vehicle performance, it is necessary to select independent variable parameters of the vehicle geometry to map the design space. A full set of modifiable parameters for a waverider vehicle in MASIV is given in Appendix A; this study limits the independent variables to analyze some key aerodynamic parameters.

Table 4.1 lists the parameters that were varied in the MASIV computations of the MAX-1 vehicle. They are the root chord (c) and aspect ratio (b/c) of the elevons, the engine width (W_e), the vehicle acceleration (a) and two trajectories: cruise and

Table 4.1: Parameters varied in the MASIV computations of the MAX-1 vehicle.

Design Parameter		Values
Root chord of elevon	c/c_{ref}	1.0, 2.0, 3.0
Elevon aspect ratio	(b/c) / $(b/c)_{ref}$	0.5, 0.75, 1.0, 1.25, 1.5, 1.75, 2.0
Engine width	$W_e/W_{e,ref}$	0.75, 1.0, 1.5, 2.0
Acceleration (m/s^2)	**a**	0.0, 1.0, 2.0
Trajectory 1 (one point)		cruise at Mach 8, H = 26 km
Trajectory 2		ascent along q = 100 kPa

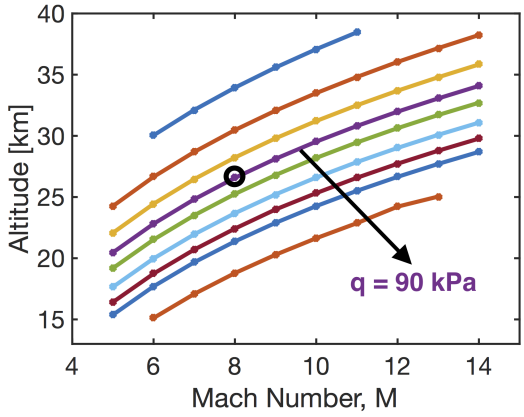

Figure 4.7: Altitude-Mach number plot of various constant-q ascent trajectories. Circle indicates the location of the 3 studied flight conditions.

ascent. Performance parameters that were computed and plotted below were L/D, T/D, angle of attack α and elevon deflection angle δ. The forces and moments are defined in Appendix B. The properties that were fixed for all MASIV computations were: vehicle length of 29.1 m, maximum width of 4.286 m and a tip chord of 3.66 m. The trailing edge of the wing (x_{TE}) was fixed to ensure pitch control and stability.

Table 4.2: Flight trim conditions selected for cruise/acceleration on Trajectory 1.

Flight Condition	Body Acceleration a (m/s)	Mach Number M_∞	Altitude H (m)	Dynamic pressure q (Pa)
Cruise	0	8	26,569	–
Acceleration 1	1	8	–	90,000
Acceleration 2	2	8	–	90,000

It was required that for each flight condition the vehicle be fully trimmed and

all forces balanced. One cruise mission and two accelerating cases are considered for the flight condition on Trajectory 1. All conditions were observed for a freestream Mach number of $M_\infty = 8$. For the cruise condition, there was no vehicle acceleration $a = 0$ m/s and the altitude $H \approx 26.5$ km, corresponding to a dynamic pressure of approximately $q = 90$ kPa. The two accelerating conditions were taken as instances on a constant dynamic pressure ascent trajectory where $q = 90$ kPa and Mach number $M_\infty = 8$. For both cases, the vehicle forces were trimmed such that the vehicle acceleration was $a = 1$ m/s and $a = 2$ m/s at that point in the trajectory. Figure 4.7 shows an altitude-Mach number sketch of multiple ascent trajectories of constant dynamic pressure, and indicates the approximate operating location for all three conditions studied. The specified conditions for vehicle trim are given in Table 4.2 for Trajectory 1. A number of geometric waverider designs were generated in this study, and each design was run at each of the three given flight conditions, and important aerodynamic trends are observed.

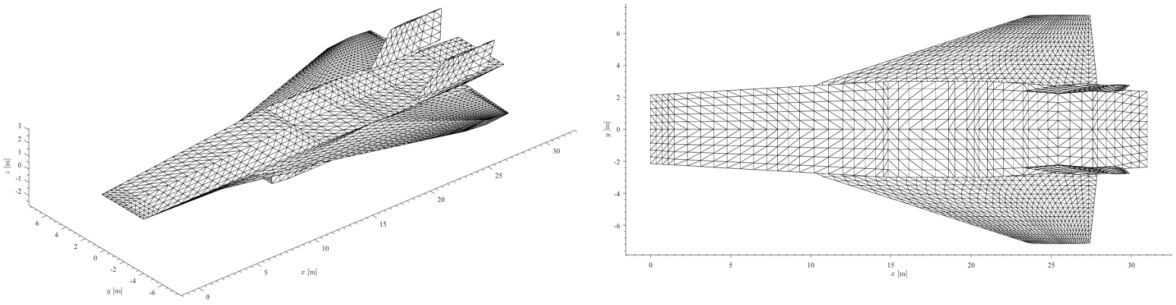

(a) (b)

Figure 4.8: (a) Azimuthal and top views of the waverider Design 3 "airplane-like", with $b/b_{ref} = 1$ and $c/c_{ref} = 3$ and $W_e/W_{e,ref} = 1$.

Changing these variables (W_e), (c), (b/c) allowed us to modification of the vehicle through an array of shapes designed to resemble a delta wing (large wing surface area, aspect ratio, "airplane-like"), a low profile slender-body aircraft (small wing

area, "rocket-like"), and numerous intermediary designs. All variations were made with respect to the default vehicle reference values, so in practice the ratios $W_e/W_{e,ref}$ and c/c_{ref} and b/b_{ref} were examined. 84 permutations of the waverider designs were generated, which included 7 different wing/elevon aspect ratios, 3 chord lengths, and 4 engine inlet widths; Table 4.3 shows the selected values for the key parameters.

Two example geometries are shown in Figures 4.8 and 4.9. The design parameters for each of these vehicles are given in Table 3, as well as those for the MAX-1 vehicle. In addition to the key parameters described earlier (b, c, and W_e), also listed are other auxiliary vehicle parameters that were also changed for each design. The motivation for additional selections was to match the constraints placed on the vehicle width $W_{vehicle}$, tip chord length c_{tip}, and the wing trailing edge location x_{TE}. The highlighted values in Table 3 correspond to parameters changed from their baseline value, with the default MAX-1 vehicle (shown in Figure 4.6(a)) serving as the basis for comparison.

Table 4.3: MASIV vehicle parameters for the MAX-1 vehicle and three different design cases.

Waverider Design #	Elevon aspect ratio b	Chord length c (% $L_{vehicle}$)	Engine inlet width W_e (m)	Elevon x-location	Sweep angle Λ (rad)	Elevon taper ratio λ
MAX-1	1.5	0.2	2.143	0.85	0.6	0.6
Design 3	1.5	0.6	2.143	0.6	0.980	0.2
Design 7	0.75	0.2	2.143	0.85	0.6	0.6
Design 23	1.125	0.4	4.286	0.73	0.828	0.3

4.4.2 Computed Effects of Geometry on L/D and T/D During Cruise

Bowcutt and others [6, 11, 12, 60–63, 93] have emphasized the need to operate near the maximum lift-to-drag ratio $(L/D)_{max}$ for good range, while maintaining sufficient T/D ratios to achieve the desired acceleration. However, also detailed were the complex interactions that occur while trying to reach optima for T/D or L/D.

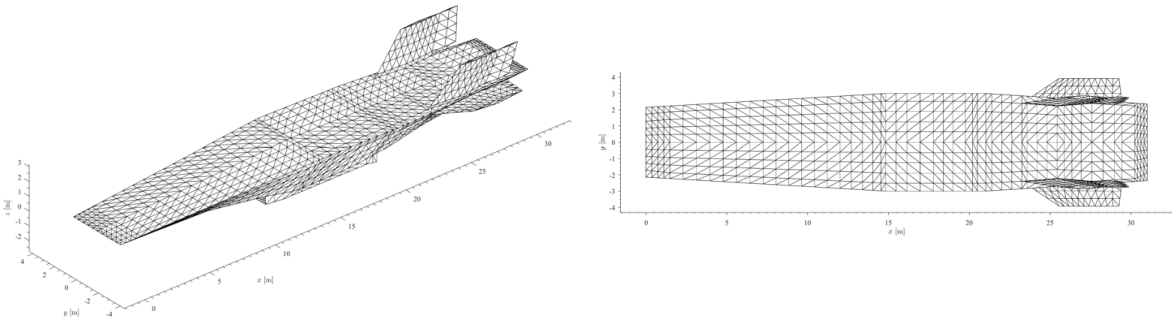

(a) (b)

Figure 4.9: (a) Azimuthal and top views of the waverider Design 7 "rocket-like", with $b/b_{ref} = 0.5$ and $c/c_{ref} = 1$ and $W_e/W_{e,ref} = 1$.

This section reports the relevant computations and compares them to the design rules and tradeoffs previously discussed.

For the first flight condition shown in Table 4.2, the vehicle is in a constant altitude cruise at 26,569 m and freestream Mach number of $M_\infty = 8$. Total net acceleration on the vehicle is zero, and all forces are balanced through trimming the vehicle. For this operating condition, we expect the total thrust to equal the drag force at cruise and similarly, a T/D ratio of near unity is observed and need not be reported. The cruise flight condition is important because it allows us to understand how the vehicle control surfaces and engine compensate for the change in vehicle design to maintain a net zero acceleration. The standard MAX-1 vehicle is given when the 3 independent vehicle design parameters $(b/c)/(b/c)_{ref}$ and (c/c_{ref}) and $(W_e/W_{e,ref})$ are equal to 1, their reference values. From the L/D trends shown in Figure 4.10, we observe some interesting results.

Figure 4.10(a) displays the computed cruise lift-to-drag ratio versus aspect ratio. The upper curve is for an elevon root chord equal to its reference value; the lower curves are for larger chords. We see that increasing the elevon wingspan via the aspect ratio $(b/c)/(b/c)_{ref} > 1$ decreases the L/D. Because the elevon control surface does not largely affect the engine inlet, we can discern that the reduction in L/D is due to

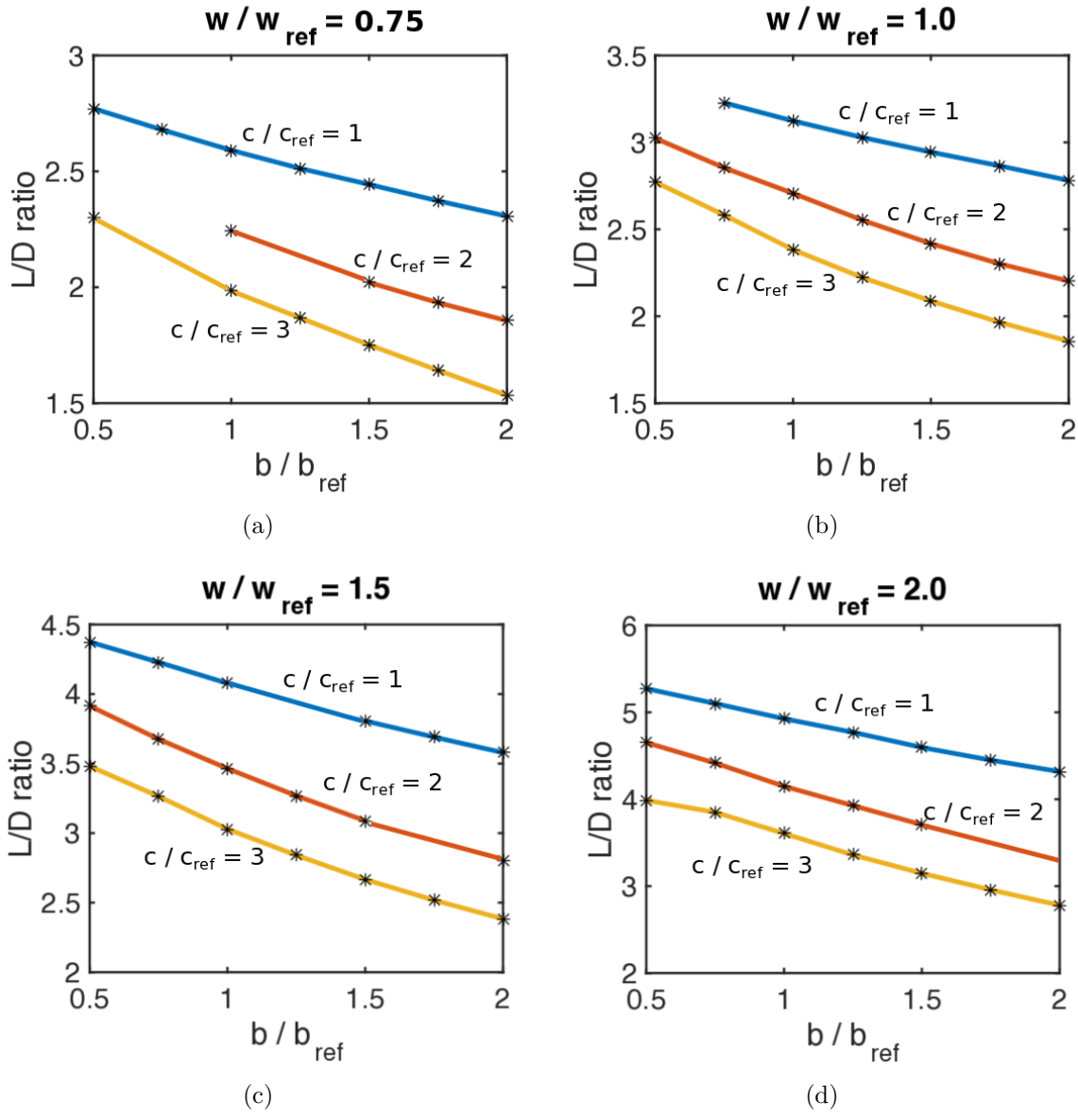

Figure 4.10: Cruise case ($\mathbf{a} = 0$): L/D ratio for a trimmed MAX-1 waverider at Mach 8 and 26 km altitude computed using MASIV. Effect of varying root chord (c), aspect ratio (b/c), engine width (W_e).

an increase in drag of the larger control surfaces. A similar conclusion is drawn for the increase of root chord length ($c/c_{ref} > 1$) and decrease of L/D. Figures 4.10(b)-4.10(d) indicate the changes as the engine width (W_e) is increased. Surprisingly, the "rocket-like" geometry (circular symbol, that corresponds to the smallest elevon planform area) has the largest L/D ratio of approximately 5.0. The "airplane-like" geometry (square symbol, largest planform area) has the smallest L/D ratio. This trend is opposite to that of a low speed aircraft.

On a hypersonic waverider, most of the lift is due to the forces on the fuselage, or engine flowpath underbody of the vehicle. As such, increasing the elevon area causes large increases in both the lift and the viscous drag, but the viscous drag dominates and becomes so large at Mach 8 that overall L/D is reduced. However, a constraint is that while a small surface area of the elevons is desired to minimize viscous drag, the elevon area may become too small to provide stability as a control surface.

Note that in going from Figure 4.10(a)-4.10(d) the engine inlet width (W_e) is more than doubled. Engine width is shown to have the largest impact on the Lift-to-Drag ratio of a waverider at cruise. The curves in Figure 4.10(d) have a larger L/D of up to 5.0 than those width the smallest engine inlet width. For the narrowest engine, L/D never exceeds 2.8. This is largely in part because of the vehicle lift due to thrust. The thrust vector is in the direction of the engine axis, which is inclined upward from the relative wind vector by the angle of attack. A significant portion of the thrust vector assists in providing the lift force that is perpendicular to the relative wind. Thus a wider engine inlet creates more lift due to thrust, thus a larger L/D ratio.

The angle of attack (α) trends in a unique manner. α, combined with the elevon deflection angle (δ) control surface, are used to trim the vehicle attitude to most closely match the target flight condition. In particular for hypersonic vehicles, small changes in angle of attack have a significant impact on the vehicle aerodynamic forces. Vehicles at larger angles of attack tend to produce more wave drag, evident in equa-

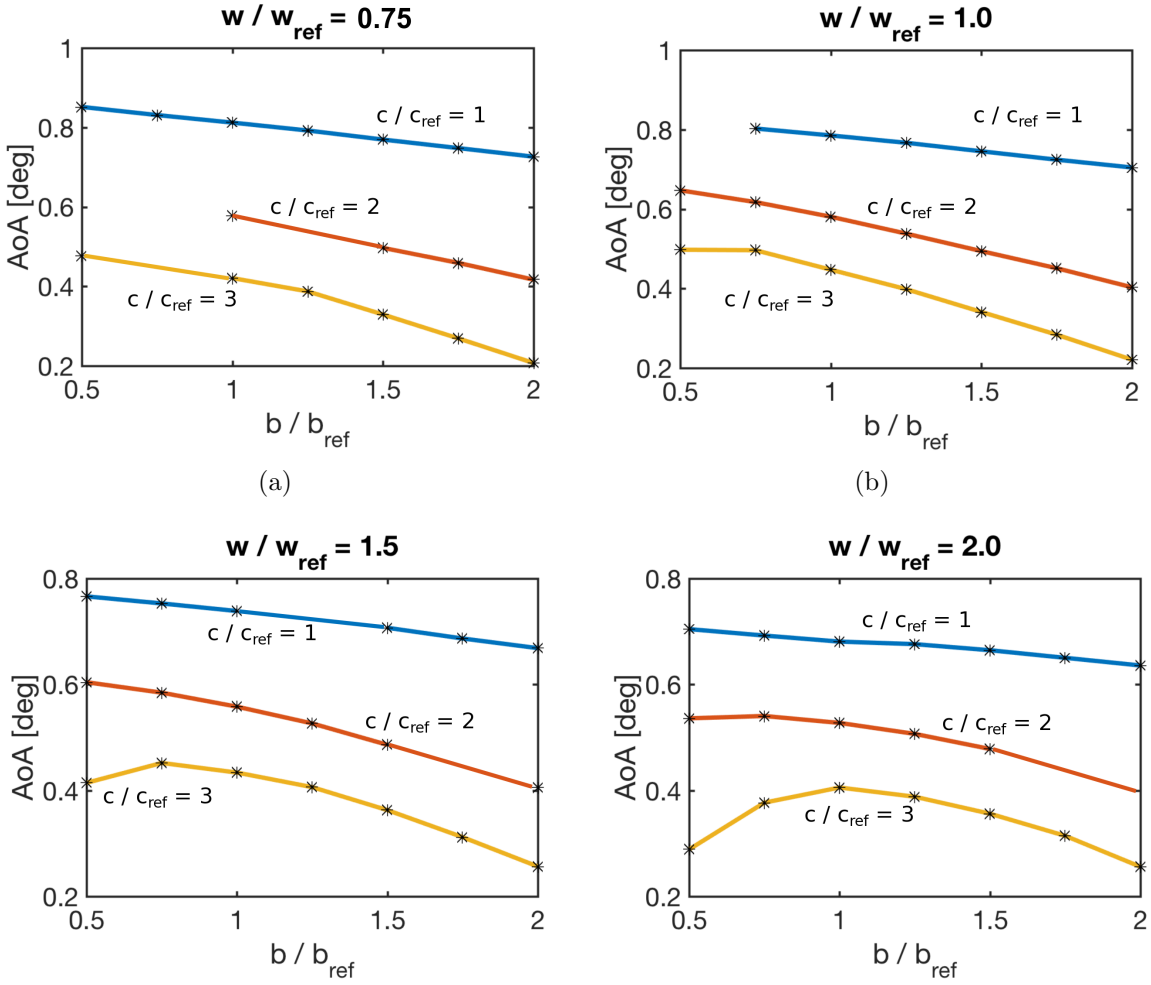

Figure 4.11: Cruise case ($\mathbf{a} = 0$): Angle of attack α for a trimmed MAX-1 waverider at Mach 8 and 26 km altitude computed using MASIV. Effect of varying root chord (c), aspect ratio (b/c), engine width (W_e).

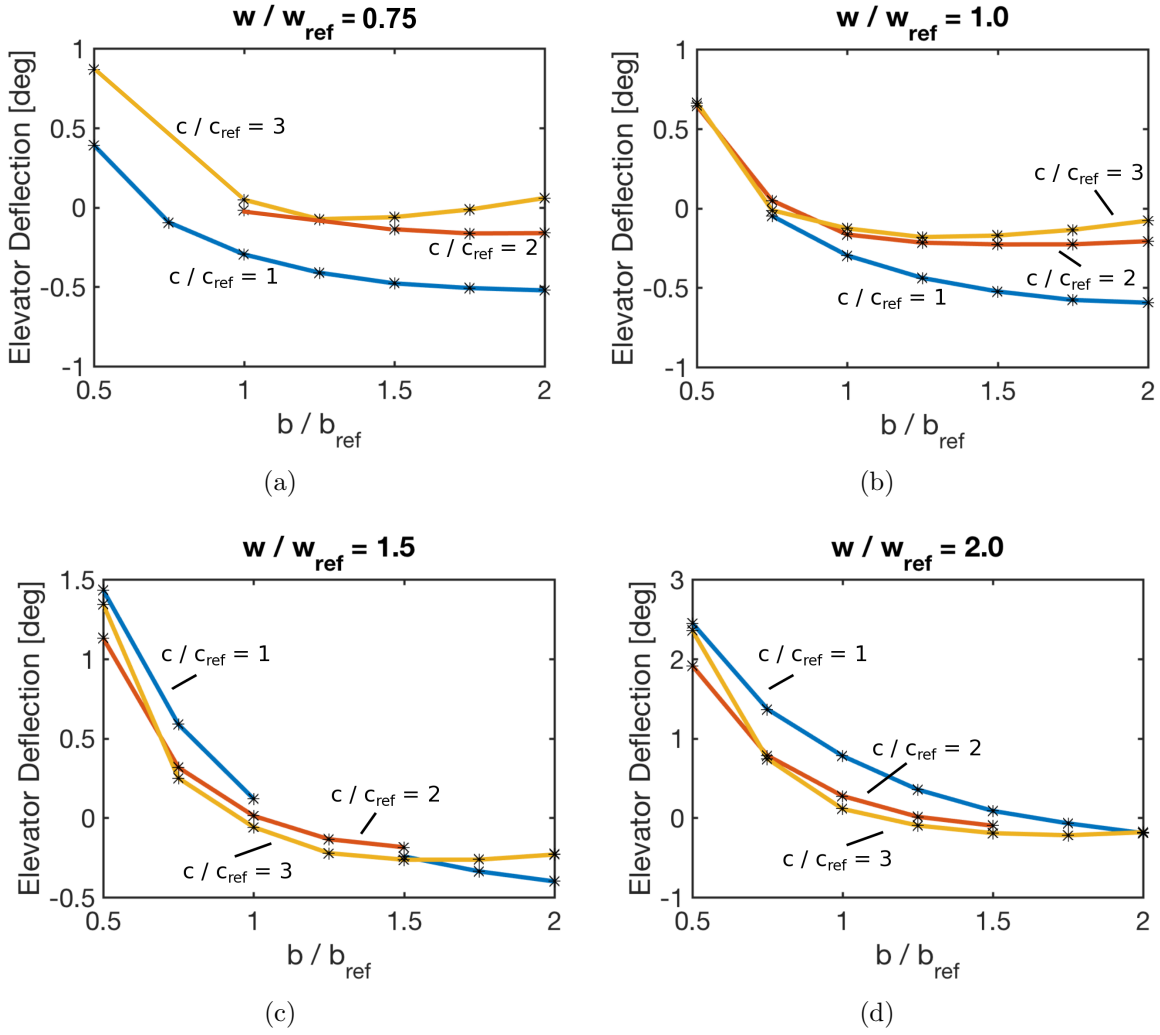

Figure 4.12: Cruise case ($\mathbf{a} = 0$): Elevon deflection δ for a trimmed MAX-1 waverider at Mach 8 and 26 km altitude computed using MASIV. Effect of varying root chord (c), aspect ratio (b/c), engine width (W_e).

tion 4.2; it is shown that as the drag inducing parameters $(b/c)/(b/c)_{ref} > 1$ and $(c/c_{ref}) > 1$ increase, the vehicle is trimmed to lower values of α.

Figure 4.11 shows the angle of attack and Figure 4.12 the elevon deflection angle for the Mach 8 cruise condition. Angle of attack is the largest (approximately 0.85 degrees) for the rocket-like geometry marked in Figure 4.11(a). The airplane-like geometry (square symbol) in Figure 4.11(a) has the smallest $\alpha = 0.2$ degrees, as expected. The curves show that as the wing surface area is increased (by either increasing the chord or the span), a smaller value of angle of attack α is needed to ensure that the lift balances the vehicle weight. Figure 4.12 indicates the elevon deflection angle that is required for trim at the cruise condition. As expected, the "rocket-like" geometry requires the largest deflection angle (of 2.5 degrees) since requires a large angle of attack due to the smaller planform area to provide lift. Note that a positive deflection angle δ corresponds to a trailing-edge-down deflection. Each curve in Figure 4.12 has a negative slope. This indicates that wings having a larger span require smaller elevon deflections to provide the necessary trim and moment force. However, care should be taken to ensure that the elevon deflection angle does not exceed the maximum value that the control system can handle.

Figure 4.13 shows the equivalence ratio ϕ required for cruise at Mach 8. As the engine width is increased from Figure 4.13(a) to Figure 4.13(d), the air flow rate captured in the engine flowpath increases and thus the fuel-air equivalence ratio ϕ tends to decrease, as expected. The results showed that an excessively wide engine captured too much air and could lead to lean flameout; it also leads to excess drag of air that is captured but not used for thrust. Similarly, too narrow of an engine leads to insufficient air and fuel rich combustion, which is undesirable. Furthermore, the selection of engine width changes the area ratio of $A_{capture}/A_{frontal}$, which affects the Drag force on the vehicle. For the cruise condition, as larger drag forces are induced by the increase of $(b/c)/(b/c)_{ref}$ and (c/c_{ref}), the equivalence ratio ϕ is shown to increase

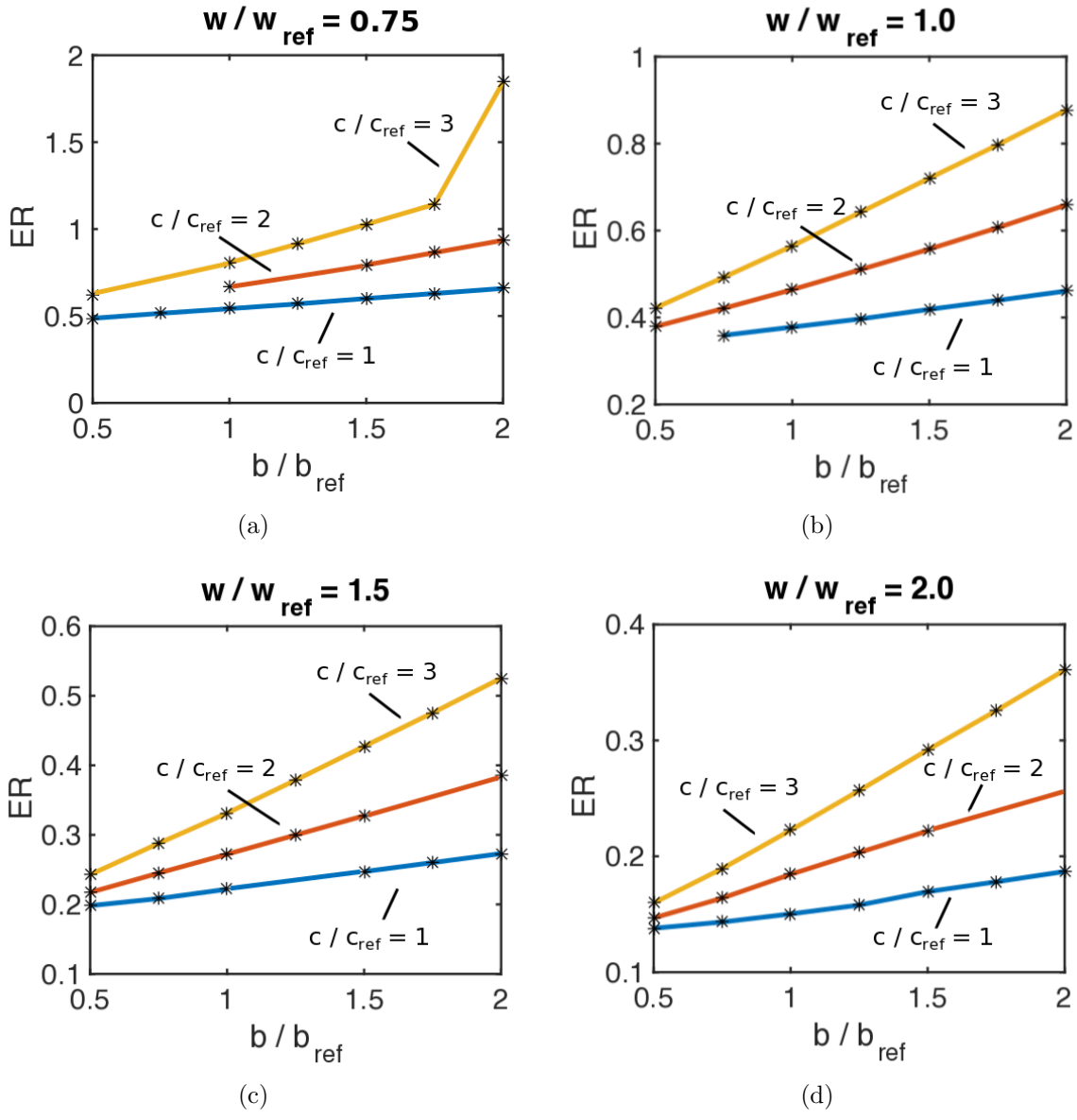

Figure 4.13: Cruise case ($\mathbf{a} = 0$): Equivalence ratio ϕ for a trimmed MAX-1 waverider at Mach 8 and 26 km altitude computed using MASIV. Effect of varying root chord (c), aspect ratio (b/c), engine width (W_e).

similarly to provide additional thrust. A higher ϕ increases the ratio of fuel being passed into the combustor for burning. The larger fraction of fuel burned results in additional thrust for the vehicle, despite short residence times that lead to incomplete combustion. Note that ϕ exceeds unity in Figure 4.13(a); this implies that some of the fuel is not burned within the combustor due to the finite rate chemical kinetics and the high strain rates imposed by the large gas velocities on the jet-in-cross flow flames.

4.4.3 Effects of Acceleration on L/D and T/D

MASIV also was used to compute L/D and T/D when the acceleration of the vehicle is set to 1 and 2 m/s^2, as shown in Table 4.1, and the trajectory is selected to be one altitude (approximately 26 km) along an ascent path of constant dynamic pressure (q = 90 kPa). Figures 4.14-C.8 show the $\mathbf{a}$ = 2 m/s^2 acceleration results, and these will be compared to the zero acceleration results for cruise detailed in Section 4.4.2. The results from $\mathbf{a}$ = 1 m/s^2 case can be found in Appendix C. For the 2 m/s^2 acceleration case, the Lift-to-Drag ratio is shown in Figure 4.14(a) to be the lowest for designs with the narrowest engine width, and highest for the largest engine widths (Figure 4.14(d). The L/D trends with respect to the elevon planform area remain consistent with the results of the zero acceleration cruise case: increasing values of $(b/c)/(b/c)_{ref}$ and (c/c_{ref}) induces a great enough wave drag penalty that offsets any Lift gained from the control surfaces and reduces overall L/D.

While the trends are similar as compared to the cruise flight case, note that the magnitude of the Lift-to-Drag ratio is higher for each vehicle design in the accelerating case. Figure 4.14(a) shows that for an "airplane-like" design the L/D is 2.3, which is not much different from the corresponding zero acceleration cruise case plotted in Figure 4.10(a) which shows L/D at 2.0. The largest gains of L/D for the 2 m/s^2 acceleration cases are seen for the "rocket-like" vehicle designs. Figure 4.14(d) shows

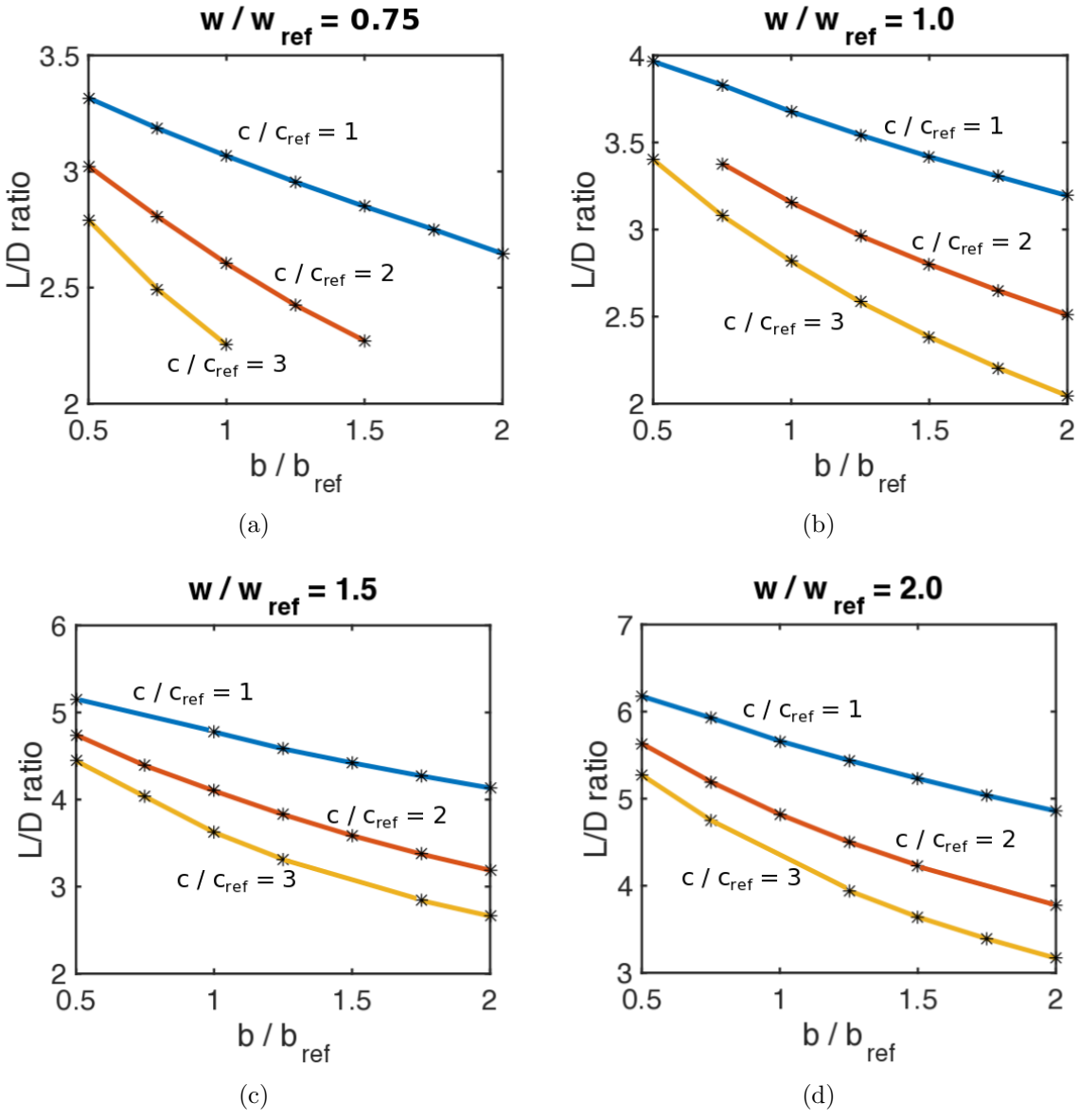

Figure 4.14: Accelerating case ($\mathbf{a} = 2$): L/D ratio for a trimmed MAX-1 waverider at Mach 8 and $q_\infty = 90$ kPa computed using MASIV. Effect of varying root chord (c), aspect ratio (b/c), engine width (W_e).

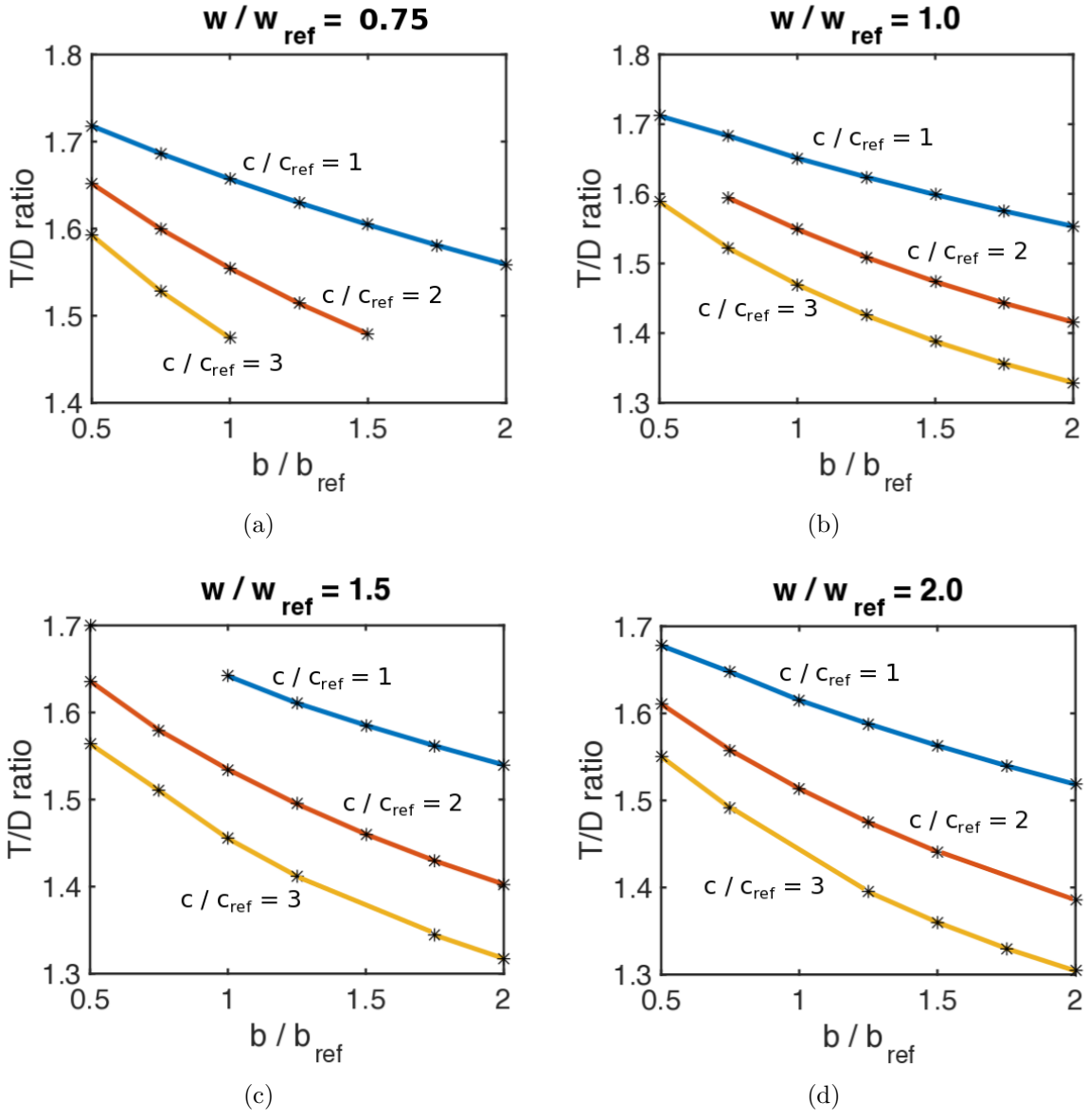

Figure 4.15: Accelerating case ($\mathbf{a} = 2$): T/D ratio for a trimmed MAX-1 waverider at Mach 8 and $q_\infty = 90$ kPa computed using MASIV. Effect of varying root chord (c), aspect ratio (b/c), engine width (W_e).

a low planform area, wide engine design with an L/D of about 6.3, higher than the 5.2 observed for the cruise flight condition in Figure 4.10(d). This is expected behavior, as we determined that most of the lift force for a waverider is produced as a derivative of the engine flowpath forces, which scales with vehicle thrust. Because the vehicle is operating at a higher acceleration, and thus higher T/D (as shown in Figure 4.15), the resulting vehicle lift force is greater and this drives up the L/D ratio.

The thrust-to-drag ratio T/D follows the same understanding as previously described. When the planform area of the elevon surfaces are increased, drag on the vehicle is also increased due to wave and viscous drag contributions. The additional drag penalties require compensation by the engine to produce enough thrust to maintain the target acceleration; this is shown by the corresponding increases in the fuel-air equivalence ratio in Figure 4.16. Figure 4.15(d) shows that the typical T/D ratio must be 1.7 for a "rocket-like" design and 1.3 for a "airplane-like" design, whereas for the zero acceleration cases T/D were approximately unity (see Appendix C).

One interesting result is that the T/D ratio remains mostly independent of the engine width design parameter ($W_e/W_{e,ref}$). This reveals two insights. One is that the drag contributions of the engine flowpath (including spillage drag forces) are small compared to the external wave and viscous drag. The second is that the equivalence ratio ϕ may be tuned to meet a specified thrust (acceleration) requirement so long as: some minimum engine width and capture area is met, and ϕ is not set to such high a value as to trigger engine unstart. Operating within these limits, equivalence ratio is allowed to exceed $\phi > 1$ indicating that combustor residence time is too short to completely burn all the injected fuel. There has been no optimization of the flow path geometry or the locations or the diameters of the wall fuel ports. If such an optimization was done, then the required equivalence ratio is expected to be closer to unity. Figure 4.16 shows the trends of the required equivalence ratio against the variation of vehicle designs. Note that the ϕ varies strongly with the engine width

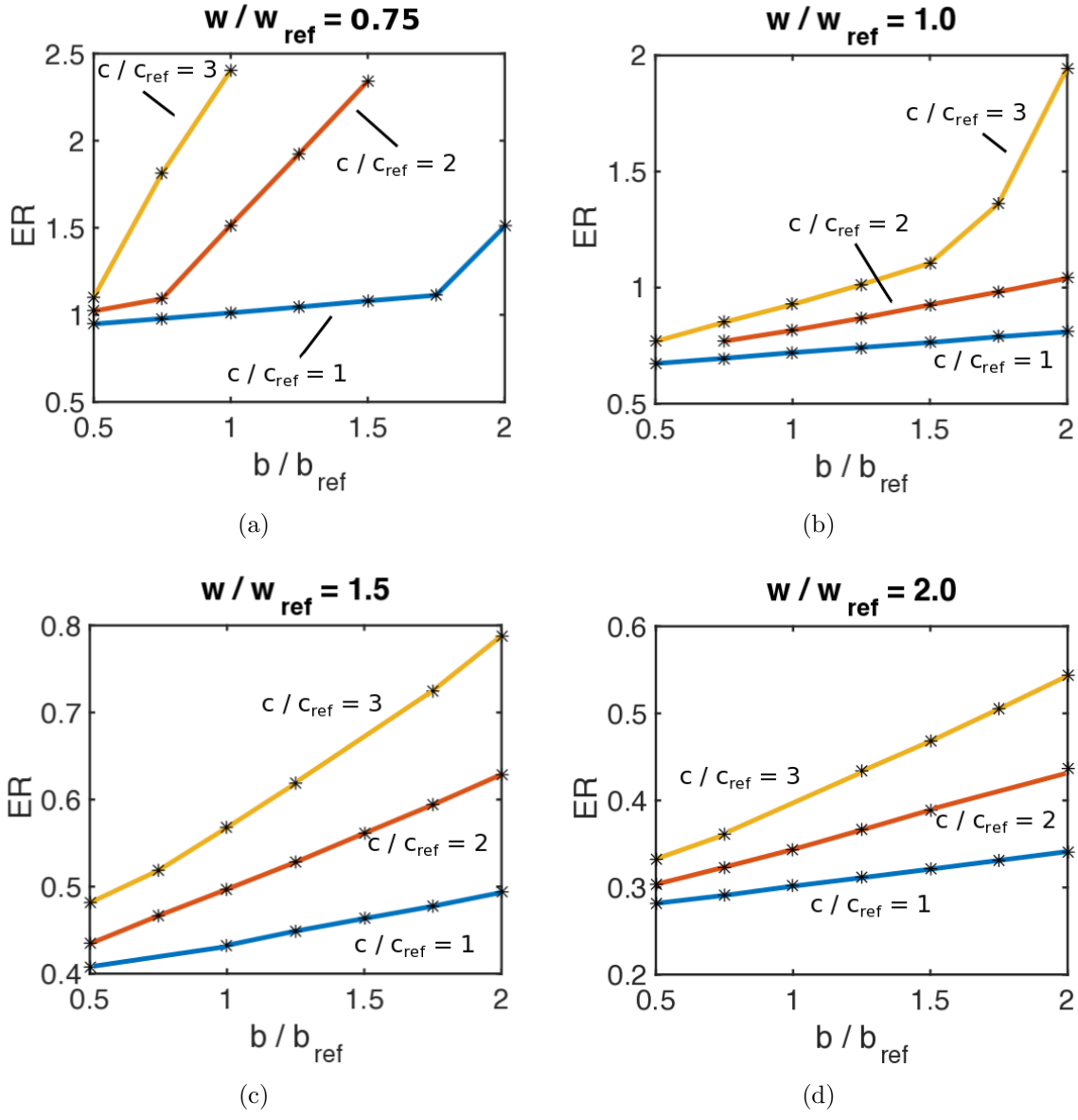

Figure 4.16: Accelerating case ($\mathbf{a} = 2$): Equivalence ratio ϕ for a trimmed MAX-1 waverider at Mach 8 and $q_\infty = 90$ kPa computed using MASIV. Effect of varying root chord (c), aspect ratio (b/c), engine width (W_e).

parameter as earlier described, similar to the results in Section 4.4.2.

Also reported are the computed angle of attack and elevon deflection angle for the 2 m/s^2 acceleration case, found in Appendix C. It is concluded that as the geometry is varied from "airplane-like" to "rocket-like", the results for the accelerating case on a $q_\infty = 90$ kPa at Mach 8 display similar trends as those of the zero-acceleration cruise case, except of course, for the T/D ratio.

4.4.4 Extension to Trajectory Operating Maps

The preceding studies have allowed an informed look at expected trends for a number of key performance metrics for 84 vehicle designs over three acceleration conditions at a single Mach number ($M_\infty = 8$) and altitude (26 km, corresponding to a dynamic pressure of $q_\infty = 90$ kPa). In an actual mission, waverider vehicles may be used to travel along some trajectory between two fixed flight conditions. These are typically prescribed as an initial and final altitude and velocity $\{h_i(q, M),\ V_i(M),\ h_f(q, M),\ V_f(M)\}$, functions of dynamic pressure and Mach number respectively. It is important, then, to map out an operating space within which the selected vehicle design's performance can be measured. Ascent trajectory maps are generated for the default MAX-1 vehicle geometry, one selected "airplane-like" design $[(b/c)/(b/c)_{ref} = 2.0,\ (c/c_{ref}) = 3.0,\ (W_e/W_{e,ref}) = 1.5]$ and one selected "rocket-like" design given by $[(b/c)/(b/c)_{ref} = 0.5,\ (c/c_{ref}) = 1,\ (W_e/W_{e,ref}) = 1.5]$.

The computed trajectory maps range from Mach numbers 7 to 13, accelerations from 0 to 8 m/s^2, and 4 dynamic pressures at 70, 90, 100 and 140 kPa. These ranges were selected to constrain the problem for analysis. Furthermore, this study is limited to scramjet-only solutions and the lower Mach number bound of 7 is chosen to avoid ram-scram transition at the target accelerations. For the remainder of this section (4.4), results from the 90 kPa constant dynamic pressure trajectory are presented. Trajectory operating maps for the 70, 100, and 140 kPa dynamic pressure q_∞ can be

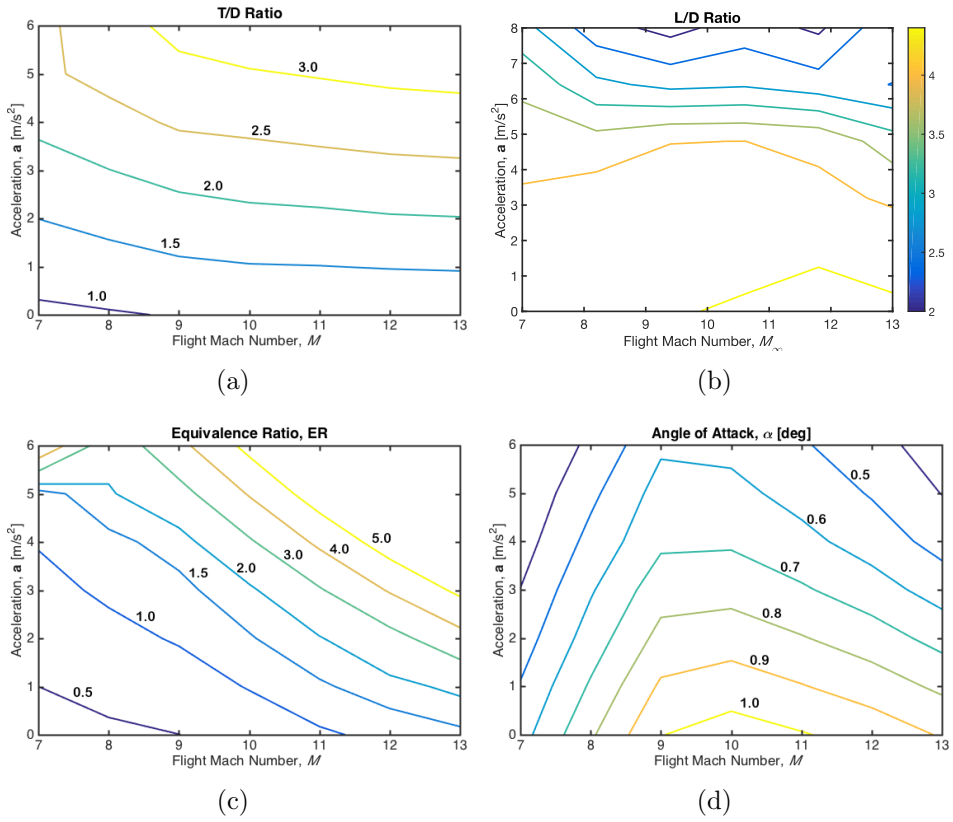

Figure 4.17: Ascent trajectory and MAX-1 vehicle geometry; showing (a) T/D ratio, (b) L/D ratio, (c) equivalence ratio ϕ, (d) elevon deflection angle δ. (Ascent is for constant dynamic pressure of 90 kPa and accelerations from zero to 8 m/s^2).

found in Appendix D. Note that maps in the appendix are computed with a heavier vehicle, at 75%-tanks-full fuel mass; the following 90 kPa analysis uses the default half tanks vehicle mass.

Consider a nominal trajectory where a vehicle accelerates from Mach 7 to 13 with a constant dynamic pressure of 90 kPa. Figure 4.17 shows the operating map for the MAX-1 vehicle geometry of the T/D, L/D and other flight conditions along this trajectory with an acceleration between 0 and 6 m/s^2. If a constant acceleration or acceleration profile is chosen for the flight (moving horizontally from left to right), the vehicle properties vary accordingly. For example on a constant 3 m/s^2 flight, the T/D ratio increases from 1.8 to 2.4 and the L/D ratio decreases slightly from 3.85 to

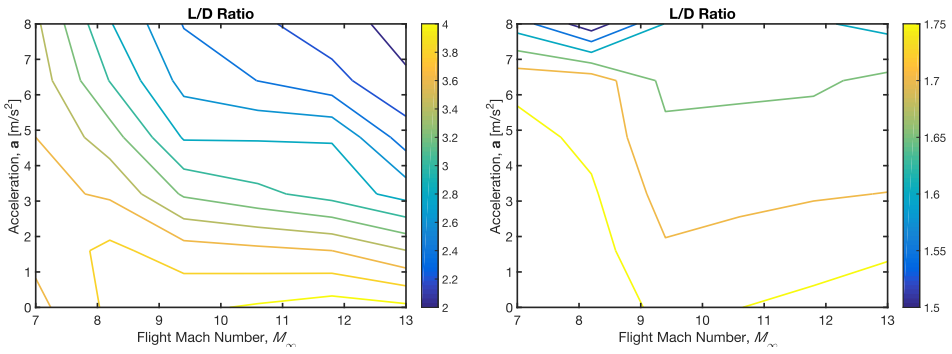

(a) (b)

Figure 4.18: Ascent trajectory map of L/D ratio for constant q_∞ of 90 kPa; showing the (a) "rocket-like" limit, (b) "airplane-like" limit. Accelerations range from zero to 8 m/s^2.

3.8. The equivalence ratio ϕ increases from a value below 1 to one greater than unity, indicating incomplete combustion at higher Mach numbers. The angle of attack α also varies from 0.4 to approximately 0.75 before dropping back down to 0.57.

Sections 4.4.2 and 4.4.3 detailed how the selection of a vehicle geometry affects the associated performance metrics for a waverider, and it was found that the trends when modifying the planform area and/or engine width were relatively consistent. The magnitudes of the L/D ratio and the equivalence ratio ϕ, however, were most pronounced between the designs and this was a result of the excessive drag induced by the larger planforms, and the resulting thrust compensation driven by the equivalence ratio. The same phenomena is observed across the whole trajectory operating maps for the two selected designs ("airplane-like" and "rocket-like").

Figure 4.18 shows the L/D ratio the two competing vehicle designs over the trajectory map of Mach number from 7 to 13 and acceleration from 0 to 8. The rocket-like vehicle in Figure 4.18(a) indicates that the lift-to-drag ratio is highest at low values of acceleration. At high values of acceleration L/D decreases quickly, dropping from 3.4 to 2.0 for a vehicle accelerating to Mach 13 at a constant 7 m/s^2. But along a trajectory of 2 m/s^2 acceleration, L/D falls less dramatically from 3.7 to 3.2. For

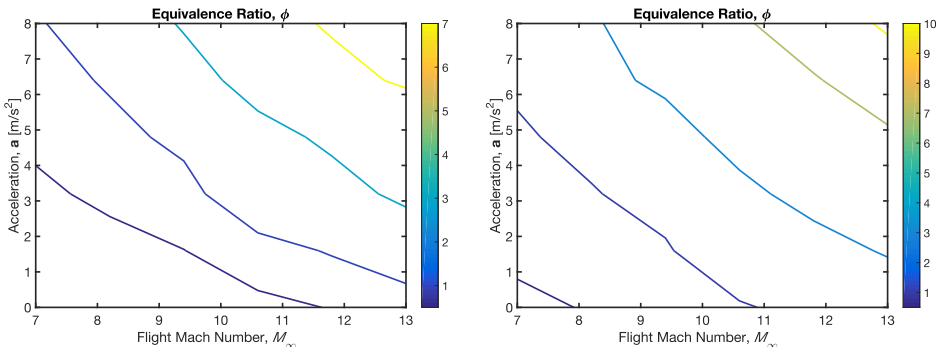

(a) (b)

Figure 4.19: Ascent trajectory map of equivalence ratio ϕ for constant q_∞ of 90 kPa; showing the (a) "rocket-like" limit, (b) "airplane-like" limit. Accelerations range from zero to 8 m/s^2.

the airplane-like vehicle design, the maximum L/D over the whole trajectory map is approximately 1.75, much less than that of the rocket-like design. It is still seen that L/D drops with both increasing acceleration and increasing Mach number. For a 6 m/s^2 constant acceleration flight, the L/D trends from 1.75 to about 1.65. The variation of lift-to-drag along the trajectory is smaller with the airplane-like design, but the associated drag penalties great reduce the overall L/D. The trends from both designs, however, provide similar insight that low acceleration trajectories are important for maximizing L/D on a constant dynamic pressure trajectory.

The operating maps for the equivalence ratio ϕ show expected results for a waverider. Equivalence ratio is a key parameter for driving the engine thrust output. In a typical engine, maximum thrust usually corresponds to a stoichiometric fuel-air equivalence ratio of 1, where all of the reactant fuel is burned without any excess air or oxidizer. Fuel-lean operation of $\phi < 1$ is then used to throttle the thrust output to a desired level. Equivalence ratio greater than unity is a fuel-rich scenario where the reaction is limited by the available oxidizer and the excess fuel is not burned and is wasted. In a scramjet waverider vehicle however, due to incredibly small combustor residence times, mixing-limited reaction zones, and incomplete combustion, an

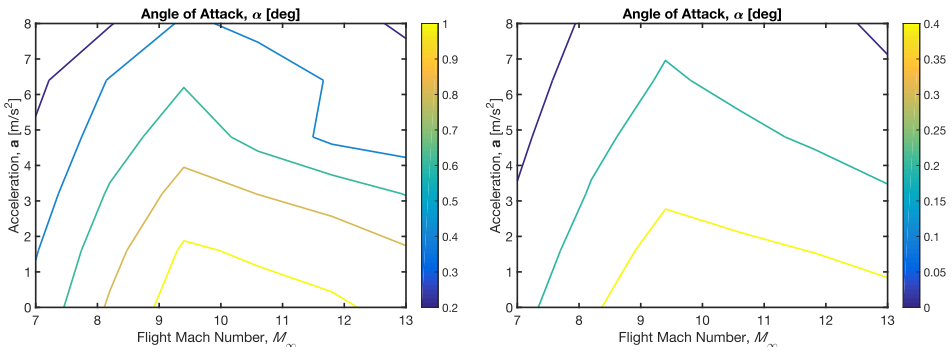

(a) (b)

Figure 4.20: Ascent trajectory map of angle of attack α for constant q_∞ of 90 kPa; showing the (a) "rocket-like" limit, (b) "airplane-like" limit. Accelerations range from zero to 8 m/s^2.

equivalence ratio $\phi = 1$ does not always correspond to complete burning or maximum thrust. Except at low Mach numbers and low altitude (high q_∞), for most points along an ascent trajectory the amount of fuel burned doesn't reach stoichiometric levels of ϕ. In these conditions though, increasing ϕ can still add thrust by increasing the volume of fuel injected and quickly burned before the excess is blown out of the engine.

Figure 4.19 shows that for each vehicle design, equivalence ratio increases with Mach number and acceleration from values less than 1 to greater than unity. The airplane-like design indicates higher equivalence ratios required over the entire operating map in order to compensate for the added drag of the design with additional thrust.

Lastly, the angle of attack is displayed in Figure 4.20. The rocket-like design indicates higher angles of attack than the airplane-like design over the whole operating map. This is expected behavior as the rocket-like waverider angle of attack plays are larger role in balancing the vehicle forces due to its reduced control surfaces. Lower angles of attack are seen for airplane-like design due to both the lift contributions of the larger control surfaces, as well as to reduce the induced drag in order to achieve

the target acceleration (or T/D) requirement.

4.4.5 Specific Impulse and T/D for Hypersonic Vehicles

A key parameter for hypersonic vehicles is the effective specific impulse, which is defined as:

$$I_{sp,\text{eff}} = (\mathcal{T} - D) \ / \ (\dot{m}_f g) \tag{4.12}$$

The traditional definition of specific impulse (I_{sp}) does not include drag and is a figure of merit for only the engine. The effective specific impulse includes drag and is useful metric for the entire vehicle. The quantity $(\mathcal{T} - D)$ in equation 4.12 is inserted into Newton's Law (equation 4.1) and both sides are multiplied by U_∞, while recognizing that $U_\infty \sin(\gamma)$ equals dh/dt, where h is altitude. Replacing $\dot{m}_f$ with $(-dm/dt)$ yields:

$$\ln\left(\frac{m_f}{m_i}\right) = -\left[\Delta\left(\frac{U_\infty^2}{2}\right) + g\Delta h\right] \left\{\frac{1}{g\ U_\infty\ I_{sp}[1 - 1/(T/D)]}\right\}_{avg} \tag{4.13}$$

Equation 4.13 is illuminating because it highlights the importance T/D is for air-breathing hypersonic vehicles. The goal is to accelerate (and achieve an increase in $U_\infty^2/2$) while achieving an increase in altitude (Δh) and minimizing the fuel mass. The equation shows that a low T/D would significantly reduce $I_{sp,\text{eff}}$ relative to engine I_{sp}, thus degrading the I_{sp} benefit of an air-breathing engine. For example, a T/D of two will halve the vehicle $I_{sp,\text{eff}}$ relative to engine I_{sp} and a T/D of three will reduce $I_{sp,\text{eff}}$ to two-thirds of I_{sp}.

The operating map for T/D is shown in Figure 4.21. Thrust-to-drag varies almost linearly with vehicle acceleration; the contours of T/D vary relatively slowly with Mach number. For a 2 m/s^2 acceleration of the rocket-like design in Figure 4.21(a),

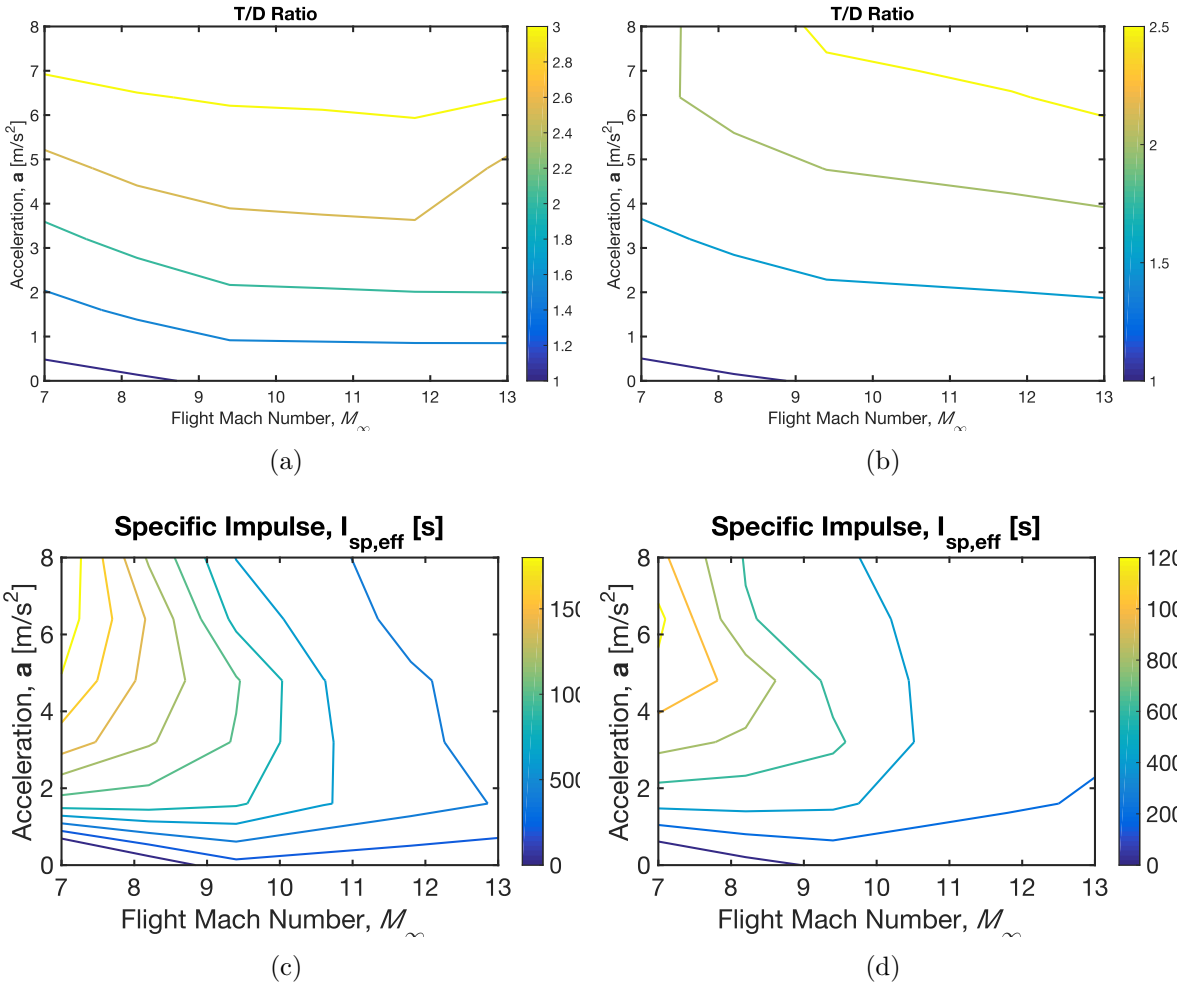

Figure 4.21: Ascent trajectory map of T/D ratio and $I_{sp,\text{eff}}$ for constant q_∞ of 90 kPa; showing the (a),(c) "rocket-like" limit, and (b),(d) "airplane-like" limit. Accelerations range from zero to 8 m/s^2.

the T/D increases from 1.5 to 2.0. Similarly, Figure 4.21(b) shows an increase in T/D from 1.25 to 1.5 for the airplane-like design. The total range of the T/D is also similar between the two designs, with minimum and maximum T/D values over the trajectory map ranging from 1.0 to 3.5 and 1.0 to 3.0 for rocket-like and airplane-like designs, respectively. The rocket-like design still observes higher T/D ratios because of its reduced planform configuration and smaller drag contributions. The effective specific impulse decreases with increasing Mach number, as a result of larger fuel mass flow rates required to maintain the same acceleration at higher speeds. Figure 4.21(c) shows a larger effective specific impulse $I_{sp,\text{eff}}$ than that in Figure 4.21(d), illustrating the T/D benefit of the rocket-like design.

4.5 Trajectory Optimization for Total Fuel Usage and T/D

The computation of trajectory operating maps a priori enables the inspection of how certain performance metrics vary from some initial to final flight condition (Mach numbers 7 to 13 for any target accelerations between 0 and 8 m/s^2). The trends of lift-drag and thrust-drag ratios, as well as the angle of attack and equivalence ratio can be observed directly from the computed maps. Thus, one can sketch a singular, continuous acceleration profile against Mach number that fully prescribes the vehicle trajectory from initial $\{h_i(q_\infty, M),\ V_i(M)\}$ to final $\{h_f(q_\infty, M),\ V_f(M)\}$ flight condition at a fixed dynamic pressure.

Restricting flight to a constant dynamic pressure trajectory allows us to determine altitude h as a function of Mach number M (and by extension also, $h = h(V)$) only. An assumed atmospheric model (U.S. 1976 Standard Atmosphere) is used for the thermodynamic conditions (ρ, p, T) at altitude. Differentiating the height function with respect to time yields:

$$\dot{h} = \frac{dh}{dV}\dot{V} = \frac{dh}{dV}a \tag{4.14}$$

Understanding that $\dot{h} = V\sin(\gamma)$, the expression for acceleration then becomes

$$a\frac{dh}{dV} = V\sin(\gamma) \tag{4.15}$$

Applying the condition of constant dynamic pressure $q = \frac{1}{2}\rho V^2$, we take the derivative with respect to altitude h and set $\dot{q} = 0$. This result is substituted back into equation 4.16 the following expression for acceleration:

$$a = -\frac{V}{2\rho(h)}\frac{d\rho}{dh}\sin(\gamma) \tag{4.16}$$

This shows that for an a range of trajectory flight conditions with a given constant dynamic pressure can be expressed in terms of two variables; in this work acceleration **a** and M are used to prescribe a trajectory profile.

While any trajectory profile of acceleration against Mach number may be selected, it is important to consider that not all trajectories are optimal. The goal of a trajectory optimization is to develop and implement a framework to minimize some arbitrary function, called an objective function. In this section, two primary objective functions will be explored: total fuel usage m_f and T/D ratio. Each optimization will yield a parametrized set of n flight conditions $\{(M_1, a_1), \ldots, (M_n, a_n)\}$ that prescribes a trajectory that best minimizes (or maximizes) its objective function.

4.5.1 Minimizing Fuel Usage, m_f

Total fuel usage is defined in terms of acceleration and velocity through a change of variables and transformation that allows the fuel consumption to be calculated without a time-domain simulation, following the formulation in Dalle et. al. [12]. The discretized formula for fuel consumption is given by:

$$m_f = \sum_{i=1}^{n-1}\frac{1}{2}\left(\frac{\dot{m}_{f,i}}{a_i} - \frac{\dot{m}_{f,i+1}}{a_{i+1}}\right)(V_{i+1} - V_i) \tag{4.17}$$

where $\dot{m}_f$ is the computed fuel mass flow rate at the given flight condition.

While this formulation is time-independent, it is still necessary to calculate the time spent on each trajectory segment. The time for a trajectory segment is

$$\Delta t_i = 2\frac{V_{i+1} - V_i}{a_{i+1} + a_i} \tag{4.18}$$

Taking the derivative of equation 4.17 gives insight into the optimality conditions for the trajectory at each step. It is important to note however, that it cannot be used to solve for all $a_1, \ldots, a_n$ simultaneously because a_i depends on the mass at the previous step $m_{f,i}$ and so on. At each step the vehicle mass is updated based on the computed fuel burn from the previous step. This illuminates two things: the acceleration profile *must* be solved sequentially, and that the trajectory operating maps discussed in Section 4.4.4 are partially limited because they do not account for the changing operating landscape as the vehicle mass varies along a trajectory. The objective function for this minimization problem is the *change* in fuel consumption from the previous step, shown in equation 4.19

$$m_{f,i} = \frac{1}{2}\left(\frac{\dot{m}_{f,i+1}}{a_{i+1}} - \frac{\dot{m}_{f,i}}{a_i}\right)(V(M_{i+1}) - V(M_i)) \tag{4.19}$$

Calculating a function gradient is useful for optimization problems and often enables the use gradient-based methods that converge to a solution more quickly. In practice however, the function gradient may not always be known. Perhaps the source function/code is proprietary and the function output is given as a blackbox. In other cases, taking numerical derivatives of a complex, non-analytic function could prove to be too costly. This is the case for the current problem; in order to compute $\dot{m}_f$ the vehicle must be evaluated and forces balanced through an iterative trimming process for a target condition. In such cases, the gradient is forgone and analysis is limited to methods that do not require derivatives, such as the Golden Section Search.

The Golden Section Search method is a function minimizer and does not require derivative calculations. The optimizer begins with a supplied interval within which the function minimum is assumed to exist. The selection of two interior points follows, in a symmetric, unbiased manner, and the function is evaluated at the new points. Comparing the values of the function at the inner points, the most promising interval containing the lowest function value is selected. The key to the Golden Section Search is maintaining the neutrality of the interior point selection and reducing computational load by reusing interior points previously evaluated. The golden ratio that retains the proportions of the interior points to the outer ones is achieved by:

$$\frac{\tau}{1} = \frac{1-\tau}{\tau} \Rightarrow \tau = \frac{\sqrt{5}-1}{2} \tag{4.20}$$

In this manner, the size of the interval is iteratively reduced until the convergence tolerance is reached. Golden Section Search exhibits linearly convergent behavior, meaning that the error decreases by some fixed amount each iteration.

This method is heavily dependent on using appropriate and valid starting intervals. Depending on the function, small changes in the interval size can yield widely different converged solutions, as depicted in Figure 4.22.

For the code implementation, the Golden Section Search is a standalone script function that takes as inputs an objective function, an $N \times 2$ matrix of starting intervals for N design variables, and a convergence tolerance value. The function outputs the solution column array of design variables, minimum function value, number of objective function evaluations, and the convergence error. The two latter outputs are performance metrics of the minimizer.

For simplicity, the initial flight condition for Mach number is kept the same at 7 and the final Mach number is extended to 14 ($M_1 = 7,\ M_n = 14$) The Mach number steps are set with equal spacing. Understanding that the design problem has now reduced to a single variable optimization exercise, the Golden Section Search

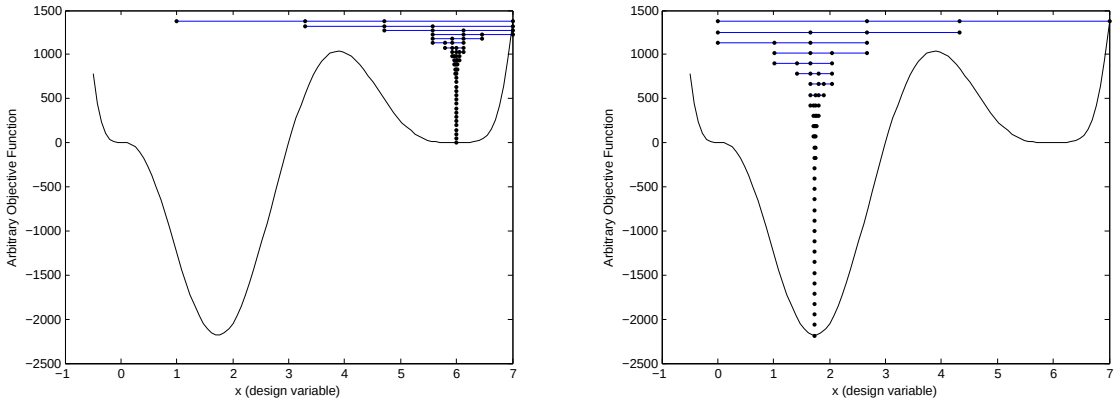

(a) (b)

Figure 4.22: Similar starting intervals result in different solutions using GSS on an arbitrary function.

algorithm is setup for $N = 1$ design variable, which is the acceleration a_i. The code, however, is constructed to handle multiple design variables as a column array, given that the objective function (and function gradient, if applicable) are properly coded to accept array inputs. The function minimization is performed at each Mach number step, and n is chosen to be 30 equally spaced steps between 7 and 14 for the remainder of this section.

4.5.1.1 Results

Table 4.4: Comparison of optimization performance for the GSS to MATLAB FMINCON methods.

Performance Metric	Golden Section Search	MATLAB FMINCON
Fuel consumed (kg)	9716.86	10941.6
Flight time (s)	805.14	1009.55
# of function evals	384	168
# of gradient evals	–	–
CPU time (s)	5712.16	3402.71
Tolerance Criteria	$\frac{\|\|(x_i - x_{i+1})\|\|}{(1+\|\|x_i\|\|)} + \frac{\|(f(x_i) - f(x_{i+1}))\|}{(1+\|f(x_i)\|)}$	$\frac{\|\|(x_i - x_{i+1})\|\|}{(1+\|\|x_i\|\|)}$
Step tolerance	2×10^{-2}	2×10^{-2}

Table 4.5: Fuel usage for several trajectories at three dynamic pressures.

Trajectory	Golden Section Search	MATLAB FMINCON
	Fuel consumed [kg]	Fuel consumed [kg]
$q_\infty = 70$ kPa, $d = 1.0$	9716.86	10941.59
$q_\infty = 70$ kPa, $d = 0.5$	7632.34	7826.65
$q_\infty = 100$ kPa, $d = 1.0$	8532.85	8609.40
$q_\infty = 100$ kPa, $d = 0.5$	5980.33	6263.14
$q_\infty = 140$ kPa, $d = 1.0$	6700.79	7000.78
$q_\infty = 140$ kPa, $d = 0.5$	4708.09	4820.97
	Flight time [s]	Flight time [s]
$q_\infty = 70$ kPa, $d = 1.0$	805.13	1009.54
$q_\infty = 70$ kPa, $d = 0.5$	723.17	833.73
$q_\infty = 100$ kPa, $d = 1.0$	841.05	774.43
$q_\infty = 100$ kPa, $d = 0.5$	631.57	650.58
$q_\infty = 140$ kPa, $d = 1.0$	668.78	649.94
$q_\infty = 140$ kPa, $d = 0.5$	494.21	509.95

4.5.2 Maximizing Thrust-to-Drag Ratio, T/D

The importance of a sufficiently high thrust-to-drag ratio is discussed at length in Section 4.2. Following the same methodology as for the fuel optimization problem, the application to the maximum T/D problem is straightforward. A simple, new objective is written as a function of T/D:

$$F(a_i, M_i) = 1 - \frac{T}{D} \tag{4.21}$$

where T/D is computed the same way as before: as an output based on the trim requirements of the given flight condition. Unlike the fuel minimization problem, the

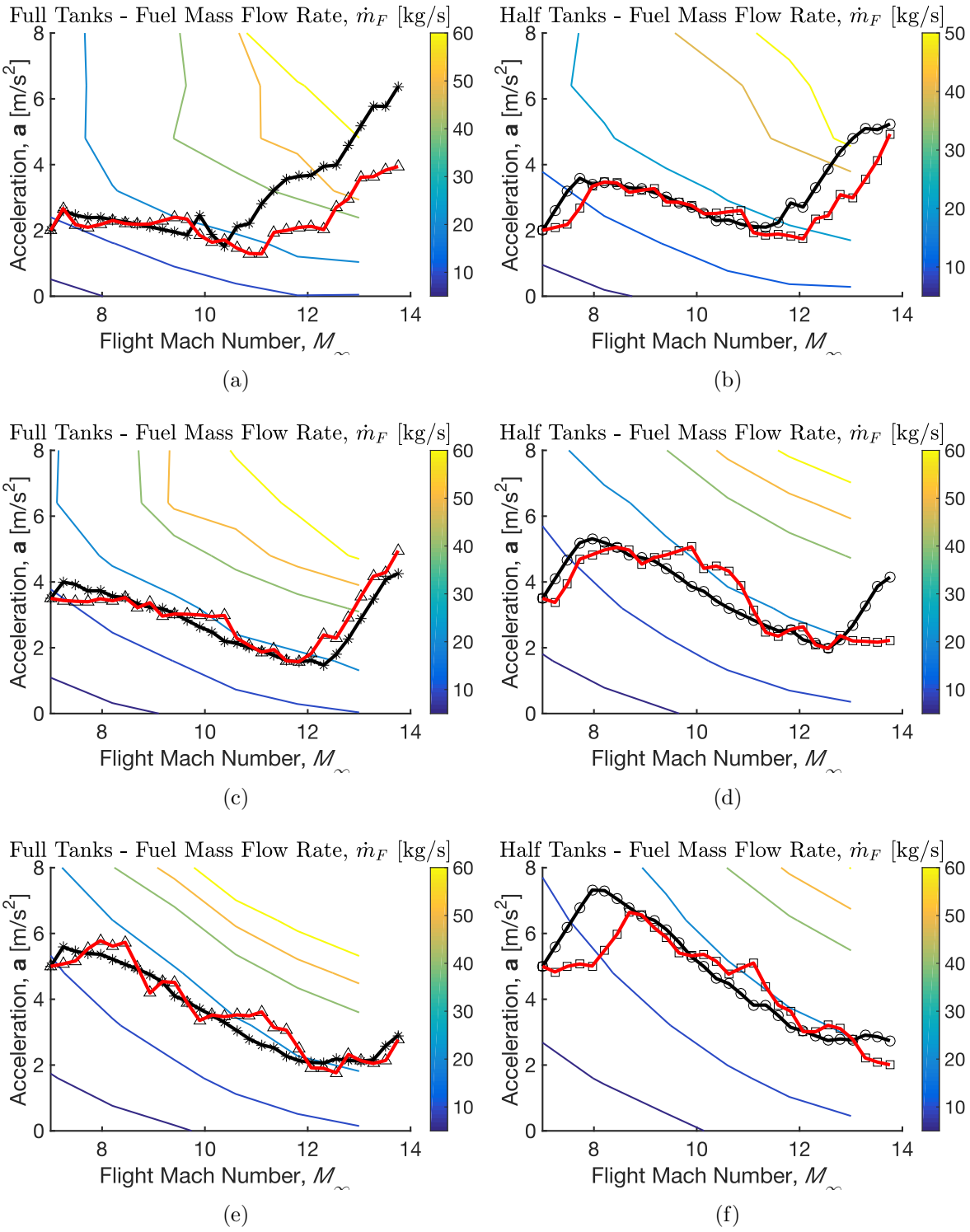

Figure 4.23: Minimum-fuel ascent trajectories for MAX-1, GSS (black) and FMINCON (red) optimizations compared. Two initial fuel fractions (d). Showing trajectories for (a) $q_\infty = 70$ kPa, $d = 1.0$, (b) $q_\infty = 70$ kPa, $d = 0.5$, (c) $q_\infty = 100$ kPa, $d = 1.0$, (d) $q_\infty = 100$ kPa, $d = 0.5$, (e) $q_\infty = 140$ kPa, $d = 1.0$, and (f) $q_\infty = 140$ kPa, $d = 0.5$.

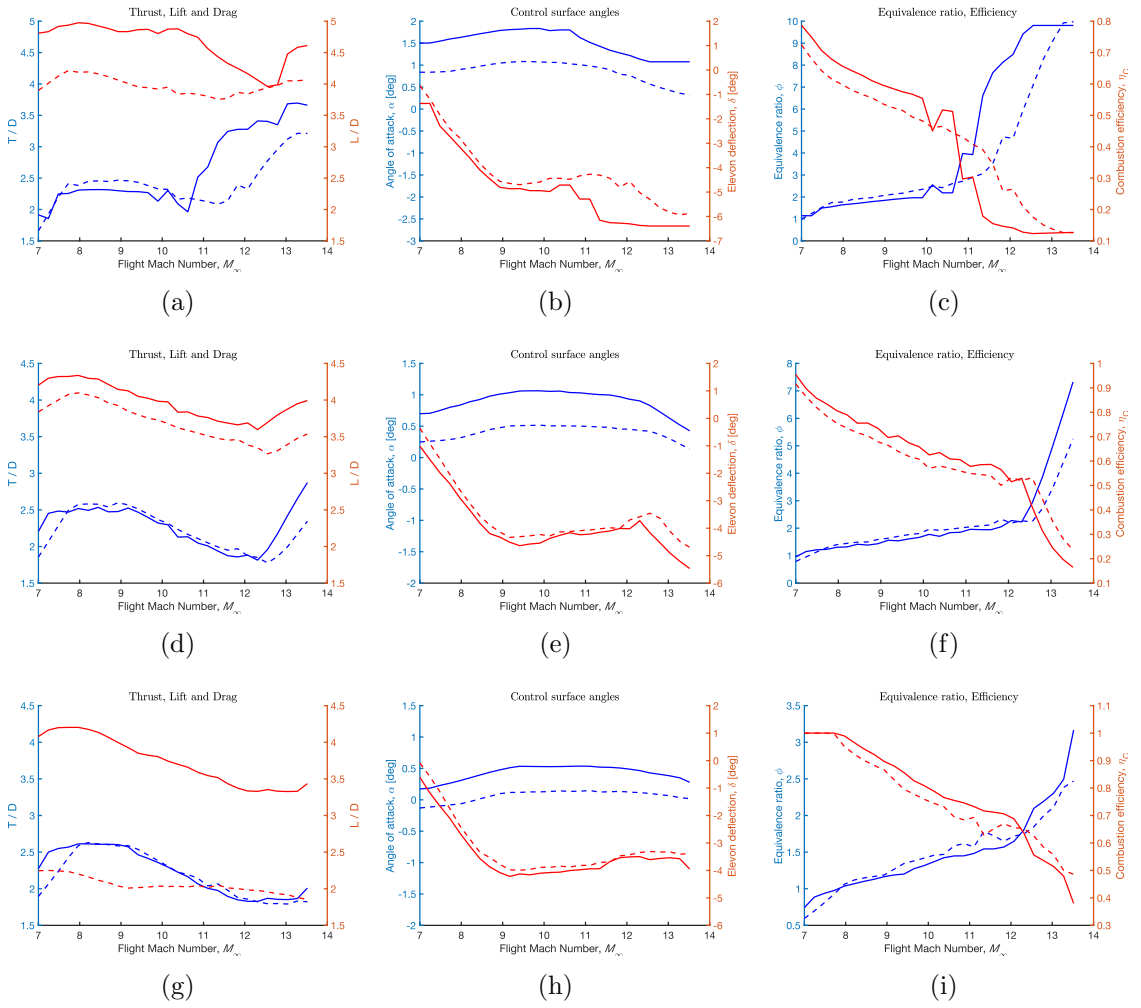

Figure 4.24: Computed metrics for the minimum-fuel ascent trajectories for MAX-1. Blue plots correspond to the Left axis, and Red plots to the Right. Solid lines are for initial fuel fraction $d = 1.0$, dashed lines for $d = 0.5$. (a), (b), and (c) represent constant dynamic pressure trajectories for $q_\infty =$ 70 kPa; (d), (e), and (f) for $q_\infty = 100$ kPa; (g), (h), and (i) for $q_\infty = 140$ kPa. Computed metrics include T/D, L/D, angle of attack α, elevon deflection δ, equivalence ratio ϕ, and combustion efficiency η_C.

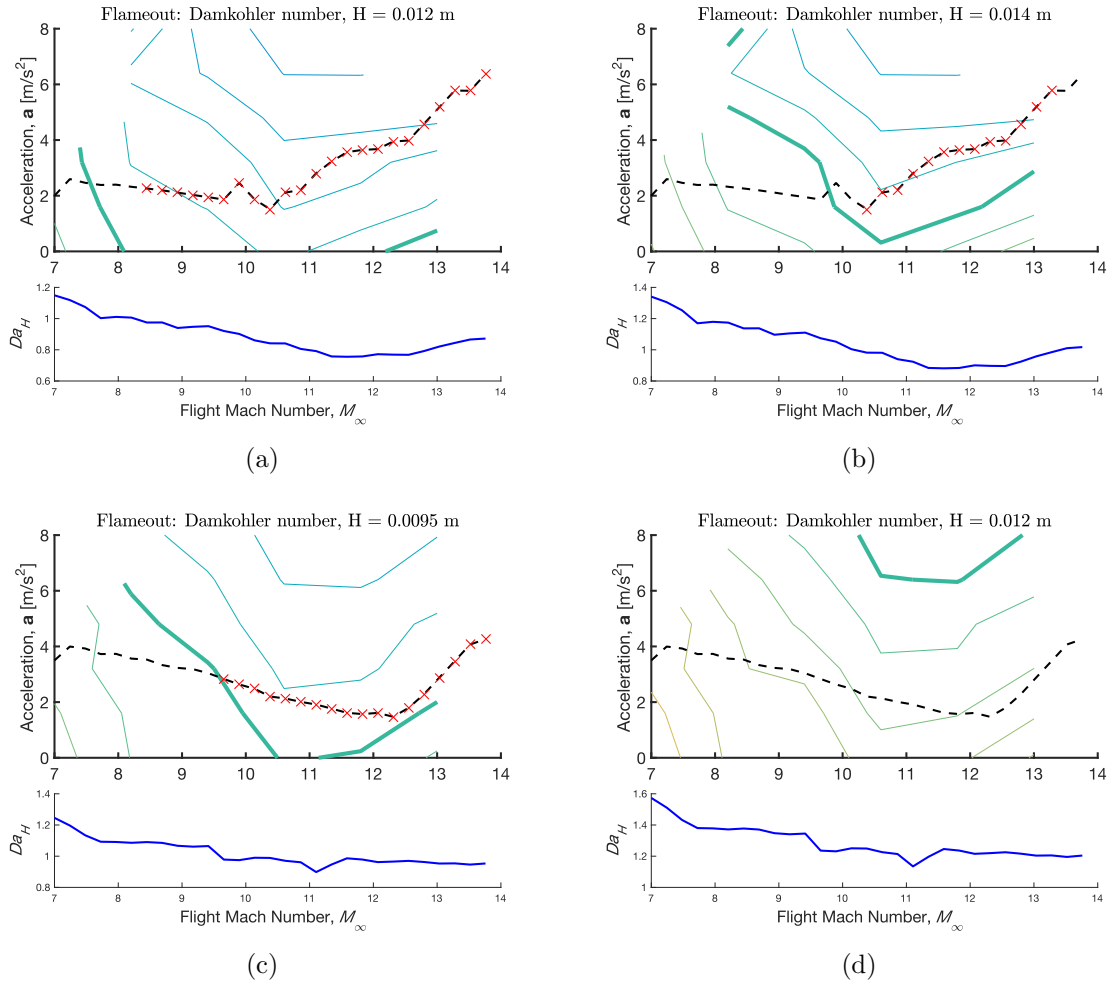

Figure 4.25: Damkohler number and Flameout limits computed along four minimum-fuel ascent trajectories. The MAX-1 waverider is used, and all vehicles start with full tanks ($d = 1.0$). Flameout regions along the ascent path are marked with an 'x'. (a) Dynamic pressure of $q_\infty = 70$ kPa, cavity step height $H = 0.012$ m, (b) $q_\infty = 70$ kPa, $H = 0.014$ m, (c) $q_\infty = 100$ kPa, $H = 0.0095$ m, and (d) $q_\infty = 100$ kPa, $H = 0.012$ m.

vehicle forces are based only on active flight conditions and not on any time history. However, due to the force balancing computations during the trimming process it remains necessary to have the correctly adjusted vehicle weight; thus, the problem must still be solved sequentially.

4.6 Conclusions

1. Some vehicle-oriented design rules were discussed that emphasize the importance of maximizing both thrust-to-drag and lift-to-drag ratios, despite some tradeoffs that are required, when designing a trimmed hypersonic accelerator on an ascent-cruise mission.

2. The advantages of selecting large dynamic pressure trajectories are discussed. Additive lift should be considered (that is due to spillage, engine cant and thrust vectoring of the exhaust) because it reduces the required angle of attack and the associated wave drag.

3. A reduced-order model (MASIV) was run for the trimmed ascent of the MAX-1 generic waverider, to quantify T/D, L/D and the advantages of the vehicle-oriented design rules. Results showed how to vary properties (such as acceleration and dynamic pressure) along the trajectory, in order to optimize both T/D and L/D and to minimize the fuel required.

4. The planform area was increased by increasing both the chord and span of the horizontal elevon surfaces. The lift increases but in most cases the viscous drag increased even more; thus excessive elevon surface area leads to an overall loss of L/D. Similar conclusions were drawn for the T/D; Variation of the engine width had the largest net effect on the L/D, due to the engine flowpath forces (and by extension the thrust) being the largest contribution to the vehicle lift. The additive drag of a wider engine is much smaller than the wave drag induced by larger control surface planform areas.

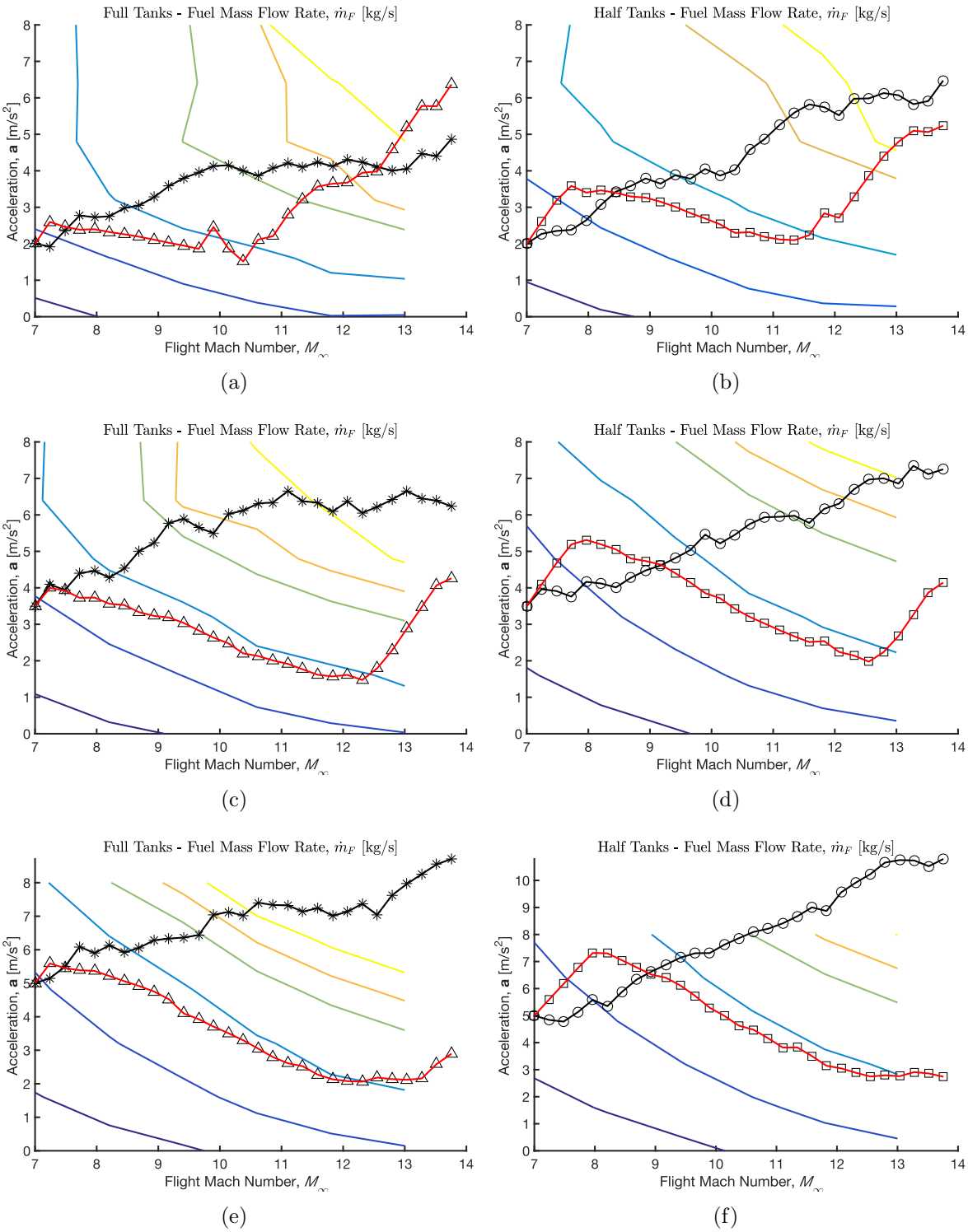

Figure 4.26: Maximum T/D (black) and minimum-fuel (red) ascent trajectories for MAX-1, superimposed. Two initial fuel fractions (d). Showing trajectories for (a) $q_\infty = 70$ kPa, $d = 1.0$, (b) $q_\infty = 70$ kPa, $d = 0.5$, (c) $q_\infty = 100$ kPa, $d = 1.0$, (d) $q_\infty = 100$ kPa, $d = 0.5$, (e) $q_\infty = 140$ kPa, $d = 1.0$, and (f) $q_\infty = 140$ kPa, $d = 0.5$.

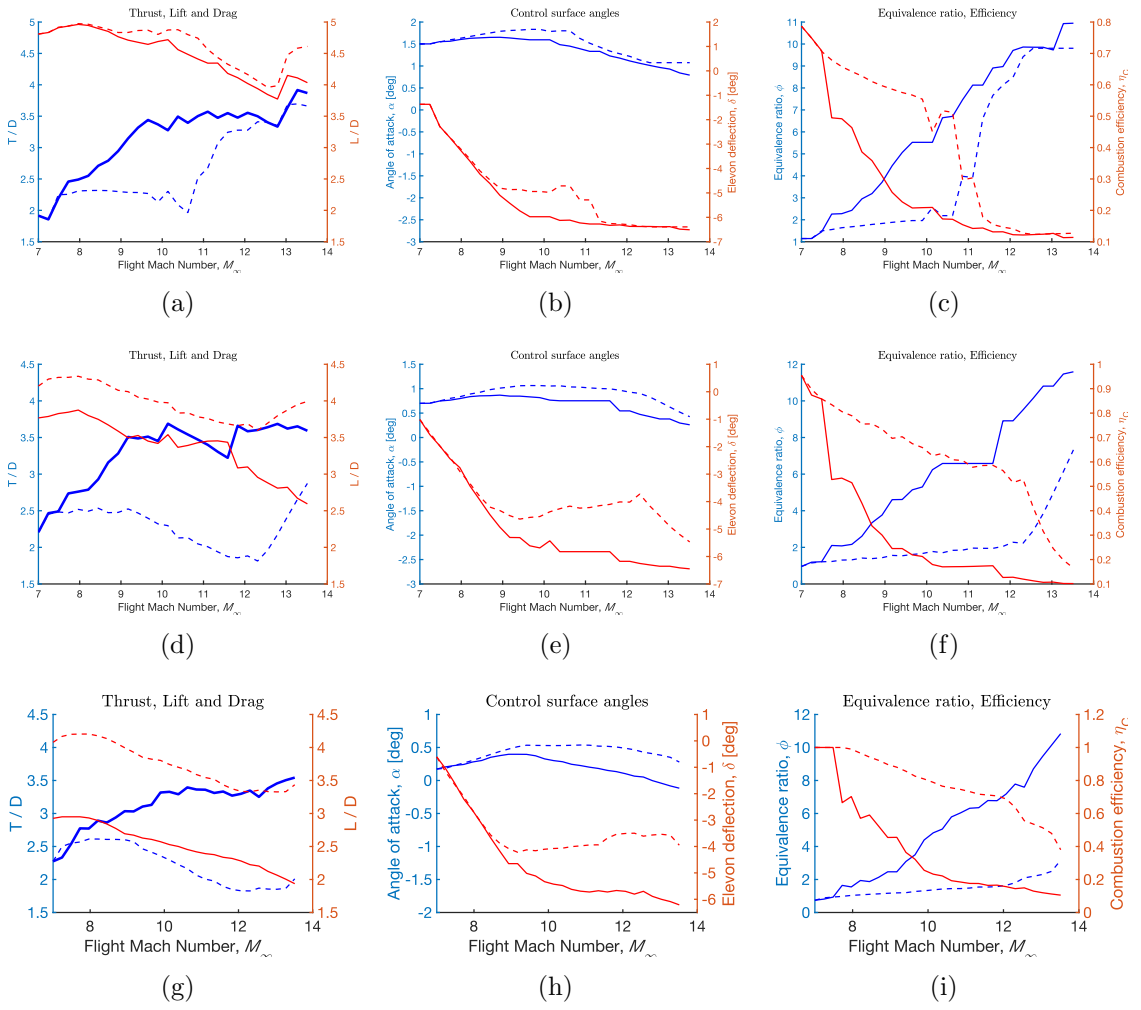

Figure 4.27: Computed metrics for the maximum T/D (solid lines) and the minimum-fuel (dashed lines) ascent trajectories for MAX-1. Blue plots correspond to the Left axis, and Red plots to the Right. All trajectories are plotted for an initial fuel fraction $d = 1.0$. (a), (b), and (c) represent constant dynamic pressure trajectories for $q_\infty = 70$ kPa; (d), (e), and (f) for $q_\infty = 100$ kPa; (g), (h), and (i) for $q_\infty = 140$ kPa. Computed metrics include T/D, L/D, angle of attack α, elevon deflection δ, equivalence ratio ϕ, and combustion efficiency η_C.

5. The computations quantify the idea that operation in the ram mode as long as possible is optimal because it provides high combustion efficiencies. The acceleration (and thus T/D ratio) selected should not exceed the unstart limit boundary that was computed.

CHAPTER V

Conclusions and Future Work

The study of hypersonic vehicles poses unique challenges in that the engine is tightly coupled with the vehicle, so it is not possible to analyze the engine by itself. Combustor pressure should not be allowed to drop too low, so the oblique shock pattern in the inlet and isolator must be strong enough to provide sufficient compression. The inlet shock strength depends on the vehicle angle of attack. This angle is determined by the trim condition that thrust, drag and acceleration be properly balanced. However, the thrust depends on the combustor pressure, temperature and other engine conditions, so these parameters are interrelated. As such, solutions can only be found through an iterative process.

The combustion flamelet data used in MASIV are stored in large, multi-dimensional matrices. The model is based on laminar diffusion flamelet theory. In particular, the gas reaction rates are found in 3-D lookup tables for each gas species that contain the rate data for discrete permutations of mixture fraction f, mixedness s, and scalar dissipation χ. Currently, data is retrieved through an interpolation of the function along the table near the given dimensions. It was necessary to speed up the interpolation process as additional dimensions were added. A program called FlameMaster, developed at Stanford, was used to solve the flamelet equations and generate the numerous lookup tables. The chemistry lookup tables have many millions of values, but

more than 90% of these values are nearly zero. The proper orthogonal decomposition (POD) is a well-defined method of producing reduced-order, but very accurate, models of large or complex data sets. POD techniques used to reduce and approximate large flamelet chemistry data sets proves to be very effective and accurate. Where the multidimensionality of the reaction rate requires numerous chemistry tables to be generated, POD is most useful in reducing the storage and memory footprint, while maintaining the integrity of the data with low error margins.

A methodology is presented to compute two operability limits that affect the ascent of a trimmed hypersonic vehicle that is powered by a dual-mode ramjet-scramjet engine. One is the flameout limit and the other is the limit where combustion efficiency drops below 0.90. During the ascent, there are competing effects of four parameters (p_3, U_3, T_3 and ER) examined. The combustor entrance pressure p_3 drops and U_3 increases, which has the adverse effect of tending to slow the chemistry and reduce the residence time. However, ascent also causes T_3 and ER increase, which tends to speed up the chemistry. It was found that a high dynamic pressure (low altitude) trajectory is best to avoid fuel lean-limit flameout.

Some vehicle-oriented design rules were discussed that emphasize the importance of maximizing both thrust-to-drag and lift-to-drag ratios, despite some tradeoffs that are required, when designing a trimmed hypersonic accelerator on an ascent-cruise mission. The advantages of selecting large dynamic pressure trajectories are discussed. Additive lift should be considered (that is due to spillage, engine cant and thrust vectoring of the exhaust) because it reduces the required angle of attack and the associated wave drag. The reduced-order model (MASIV) was run for the trimmed ascent of three waverider geometries: the MAX-1 generic waverider, a large planform area "airplane-like" design, and a narrow, low profile "rocket-like" design. The planform area was increased by increasing both the chord and span of the horizontal elevon surfaces. The lift increases but in most cases the viscous drag increased even

more; thus excessive elevon surface area leads to an overall loss of L/D. Similar conclusions were drawn for the T/D; Variation of the engine width had the largest net effect on the L/D, due to the engine flowpath forces (and by extension the thrust) being the largest contribution to the vehicle lift. The additive drag of a wider engine is much smaller than the wave drag induced by larger control surface planform areas. T/D, L/D and other metrics were quantified for each vehicle and the advantages of the vehicle-oriented design approach was discussed. Trajectory optimization results showed how to vary properties (such as acceleration and dynamic pressure) along the trajectory, in order to optimize both T/D and L/D and to minimize the fuel required.

There are many avenues for future work in the modeling of hypersonic vehicles. One of the limitations of these studies is the modeling of the combustor and fuel injectors. Currently only one jet-in-crossflow injection method is included, but future work may model different fuel injection scenarios that offer improved mixing capabilities such as: cavity-flameholder, struts, and fuel injection ports in series. More rigorous turbulence modeling can also be done to better characterize the flame and flow in the combustor. Furthermore, as additional flameout experiments are performed and reported, a more consistent and accurate measure of flameout during operation can be computed as described in this work (the trends presented here are the current emphasis). Lastly, in terms of flameout operability limits, only the lean-limit has been considered. Future research, investigation of experiments and modeling can provide an upper, rich-limit (if any) for scramjet waverider engine.

Ultimately, these findings are beneficial and contribute to the overall understanding of dynamically stable waverider vehicles at hypersonic speeds. These types of vehicles have a range of applications from technology demonstration, to earth-to-low orbit payload transit, to most compellingly another step in the development and realization of viable supersonic commercial transport.

APPENDICES

APPENDIX A

MASIV External Vehicle Design Parameters

Fuselage Parameters

Horizontal Stabilizer and Elevon Parameters

Vertical Stabilizer and Rudder Parameters

Table A.1: Full list of MASIV external vehicle body design parameters. Highlighted parameters are those investigated or constrained in this study.

Design Parameter	Description	Default Value
Fuselage		*Units [m]*
L_scale	Horizontal distance from leading edge of vehicle to leading edge of cowl. The rest of the vehicle is scaled off of this parameter.	12
L_vehicle	This can be used to force the vehicle to have a certain length. This parameter should not be used without changing L scale	30.5
tail_height	Vertical offset of trailing edge from leading edge	0.942857143
nose_width	Width of vehicle in the y-direction at the nose	4.285714286
engine_width	Width of engine flowpath	2.142857143
waist_width	Width of the upper part of the vehicle for the constantwidth section	6
waist_x	Horizontal distance from nose at which change in angle of the upper surface occurs	30.5
upper_body_angle	Angle of upper surface of the vehicle in xz-plane	0.05
tail_width	Width of vehicle in the y-direction at the trailing edge	4.714285714
mid_length	Length of upper part of vehicle that has constant width	6.1
triangle_resolution	Maximum length of side of a triangle divided by $\sqrt{(2)}$	0.915

Table A.2: Full list of MASIV external vehicle body design parameters. Highlighted parameters are those investigated or constrained in this study.

Design Parameter	Description	Default Value
Horizontal Stabilizer and Elevon		
elevator_x_root	The x-coordinate of the center of the horizontal control surface at the root as a fraction of L vehicle	0.85
elevator_z_root	The relative z-coordinate of the root of the horizontal surface. This is given as a fraction of the height of the side of the fuselage at the corresponding x-coordinate.	0.7
elevator_chord	Chord of total horizontal surface given as a fraction of L vehicle	0.2
elevator_sweep	Sweep angle of mean chord line in radians	0.6
elevator_taper_ratio	Ratio of chord at tip to chord at root	0.6
elevator_thickness	Ratio of thickness of airfoil to chord of airfoil	0.08
elevator_aspect_ratio	Aspect ratio of horizontal control surface wing planform	1.5
elevator_dihedral	Angle between plane containing wing planform and xy-plane in radians	0.05
elevator_fraction	Fraction of horizontal surface to be movable. If this is greater than 0.95, the surface will be all-moving.	1

Table A.3: Full list of MASIV external vehicle body design parameters. Highlighted parameters are those investigated or constrained in this study.

Design Parameter	Description	Default Value
Vertical Stabilizer and Rudder		
rudder_x_root	The x-coordinate of the center of the vertical control surface at the root as a fraction of L vehicle	0.85
rudder_y_root	The relative y-coordinate of the root of the vertical surface. This is given as a fraction of the width of the top of the fuselage at the corresponding x-coordinate.	0.9
rudder_chord	Chord of total vertical surface given as a fraction of L vehicle	0.2
rudder_sweep	Sweep angle of mean chord line in radians	0.6
rudder_taper_ratio	Ratio of chord at tip to chord at root	0.7
rudder_thickness	Ratio of thickness of airfoil to chord of airfoil	0.08
rudder_aspect_ratio	Aspect ratio of vertical control surface wing planform	1.1
rudder_dihedral	Angle between plane containing wing planform and xz-plane in radians	0.15
rudder_fraction	Fraction of horizontal surface to be movable. If this is greater than 0.95, the surface will be all-moving.	0.3

APPENDIX B

Details of the Flight Dynamics and Vehicle Forces

The MASIV trim code employs the same nomenclature and flight dynamics equations as those of the Bolender and Doman code [8]. Thrust is defined as the component of the total force imposed on the vehicle by the fluid that passes through the engine flow path, that acts in the direction of the axis of the engine. The engine flow path begins at the vehicle leading edge and ends at the vehicle trailing edge. The flow path

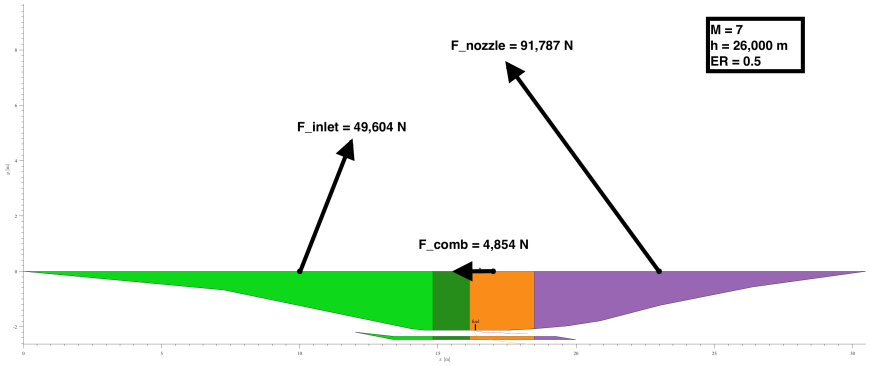

Figure B.1: Resultant forces *along the engine flowpath* for $M_\infty = 7$, $h = 26km$, $ER = 0.5$. Forces are in the body axes, such that Thrust points to $-$x-direction.

is only a fraction of the width of the underside of the vehicle, since the engine width is less than the vehicle width. Vehicle lift and drag are defined to be the components of the aerodynamic force that acts in the directions perpendicular and parallel to the relative wind, respectively. The aerodynamic force is the total force on the vehicle minus the thrust and gravitational forces. The acceleration of the vehicle is a vector in the direction of the flight path.

The pitching moment (M) has 7 components: $M_f + M_u + M_n + M_a + M_{cs} + M_{inlet} + z_T T$. The subscripts f, u and n correspond to the fore underbody, the upper surface, and the engine nacelle outer surface, respectively. Subscripts a, cs and $inlet$ refer to the aft underbody, the control surfaces and the inlet turning forces, respectively. Weight is not included since it acts at the center of gravity. Each moment is a product of a wall pressure and a length, as defined in [8]. For the case of a horizontal flight path that is parallel to the relative wind and for no engine cant, as shown in Figure B.2, the lift force is $F_x \sin(\alpha) - F_z \cos(\alpha)$ and the drag force is $D = -F_x \cos(\alpha) - \sin(\alpha)$. The magnitude of the thrust force is: $\dot{m}_a(V_e - V_\infty) + (p_e - p_\infty)A_e - (p_1 - p_\infty)A_i$ and the thrust vector is parallel to the engine axis, so it exerts a component in the lift direction. The two components of the weight force are: $W_z = Mg\cos(\alpha + \gamma)$ and $W_x = -Mg\sin(\alpha + \gamma)$.

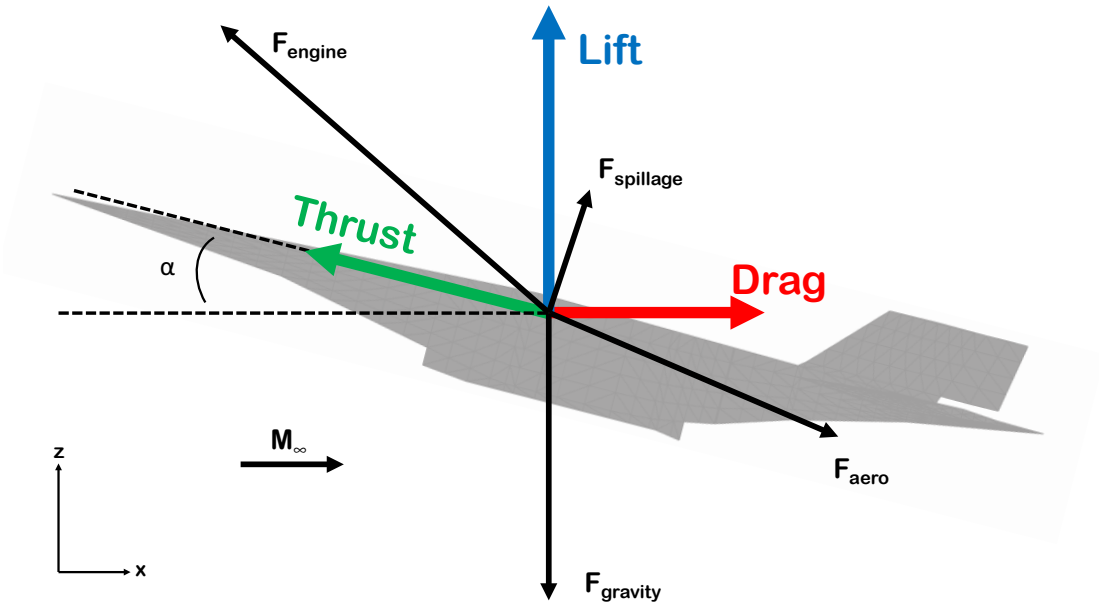

Figure B.2: Thrust, drag, lift and gravitational forces for the case of a horizontal flight path that is parallel to the relative wind and no engine cant.

APPENDIX C

Additional Computed Metrics for 0, 1, and 2 $\mathbf{m/s^2}$ Acceleration Cases

L/D, T/D, Equivalence ratio ϕ, Angle of attack α, and Elevon deflection angle δ Values for a $= 1$ $\mathbf{m/s^2}$

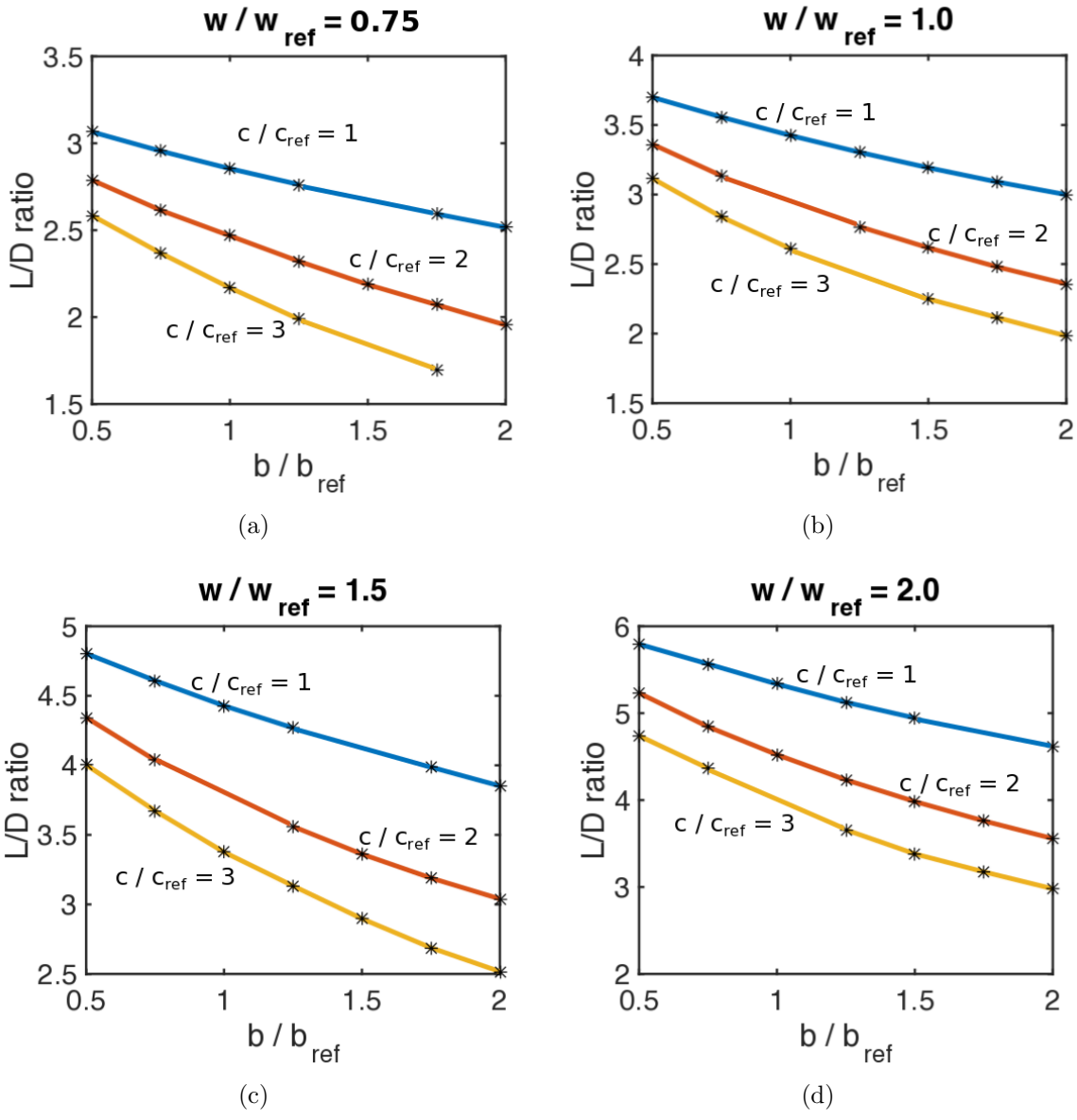

Figure C.1: Accelerating case ($\mathbf{a} = 1$): L/D ratio for a trimmed MAX-1 waverider at Mach 8 and $q_\infty = 90$ kPa computed using MASIV. Effect of varying root chord (c), aspect ratio (b/c), engine width (W_e).

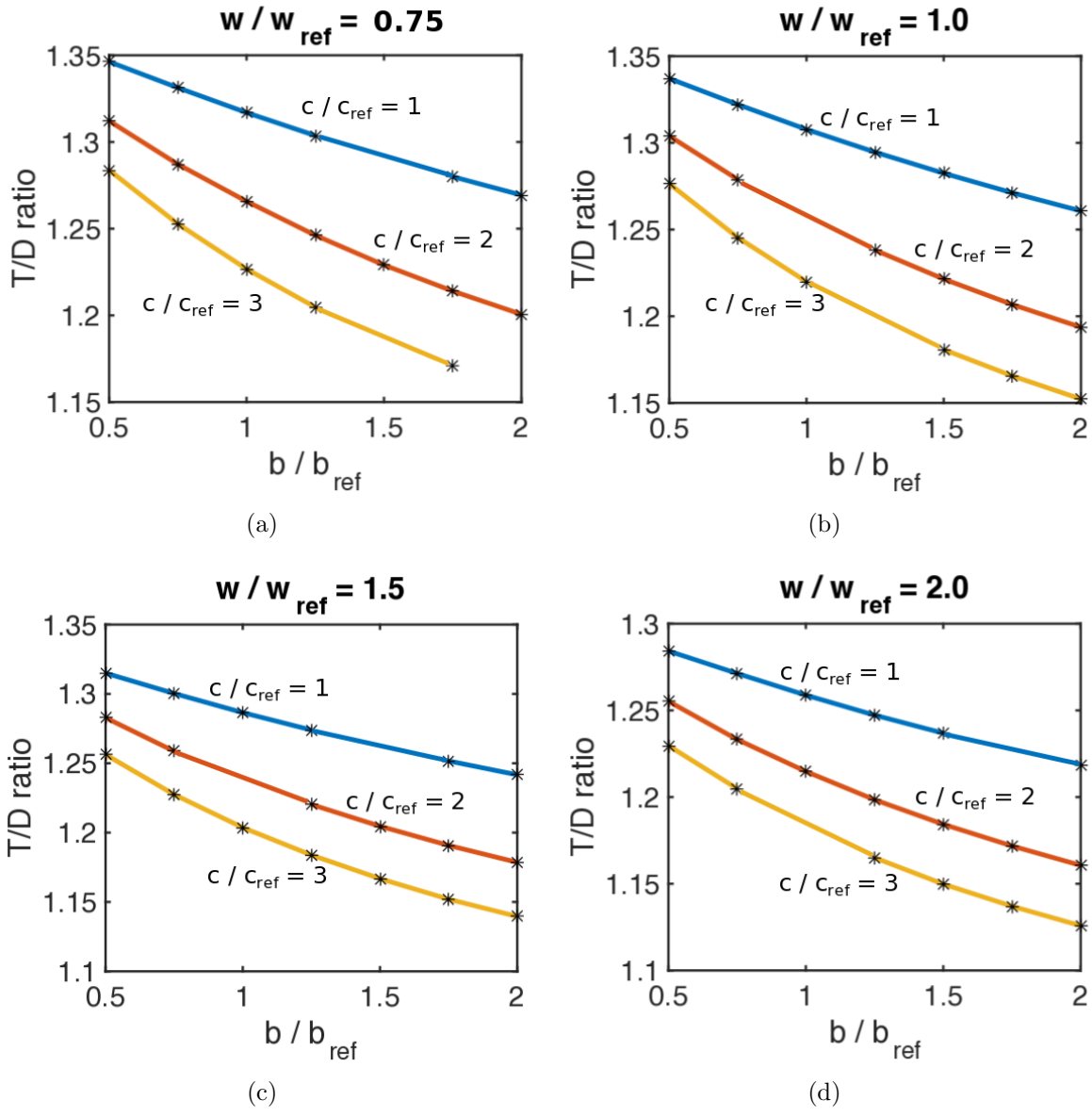

Figure C.2: Accelerating case ($\mathbf{a} = 1$): T/D ratio for a trimmed MAX-1 waverider at Mach 8 and $q_\infty = 90$ kPa computed using MASIV. Effect of varying root chord (c), aspect ratio (b/c), engine width (W_e).

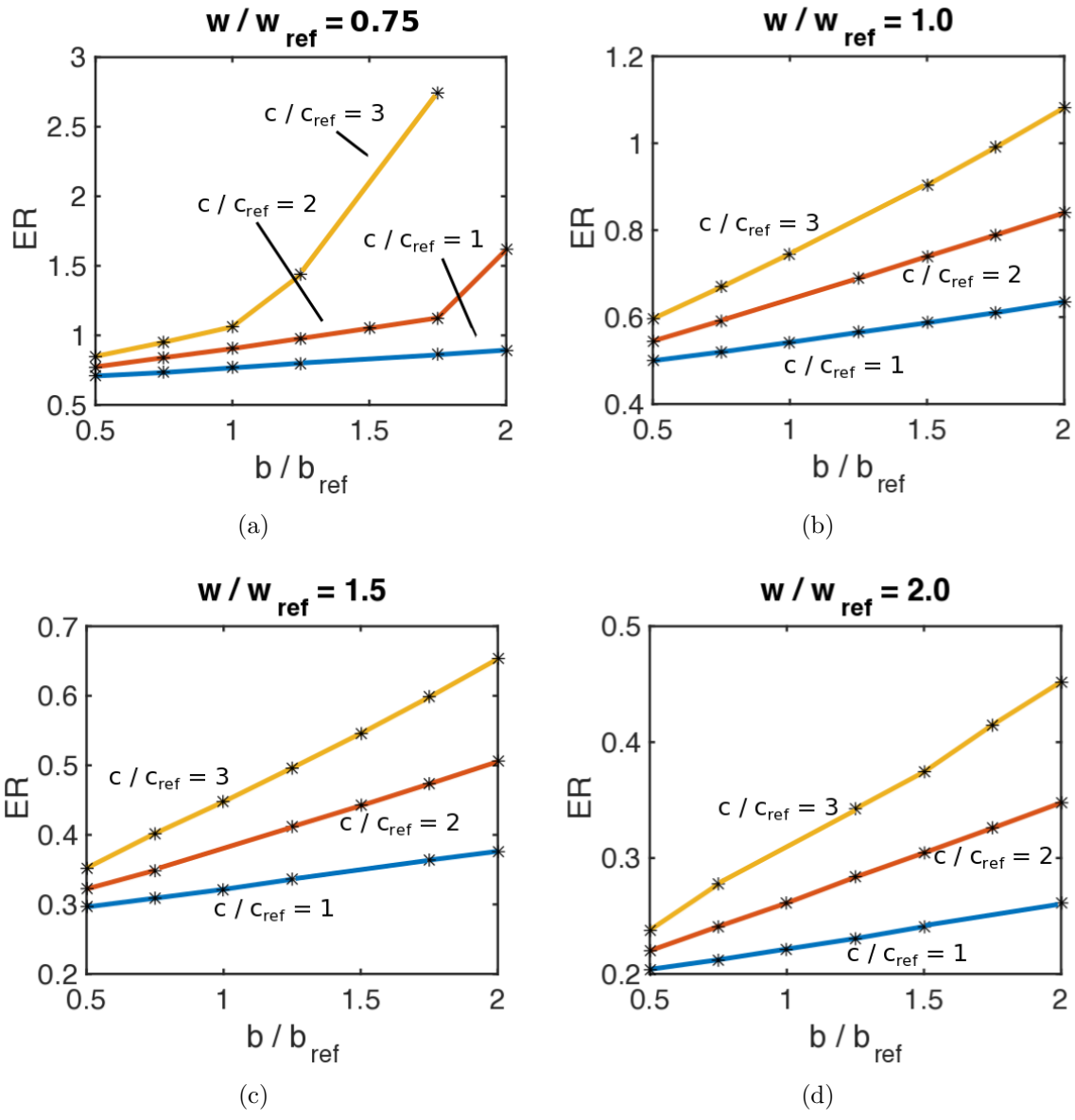

Figure C.3: Accelerating case ($\mathbf{a} = 1$): Equivalence ratio ϕ for a trimmed MAX-1 waverider at Mach 8 and $q_\infty = 90$ kPa computed using MASIV. Effect of varying root chord (c), aspect ratio (b/c), engine width (W_e).

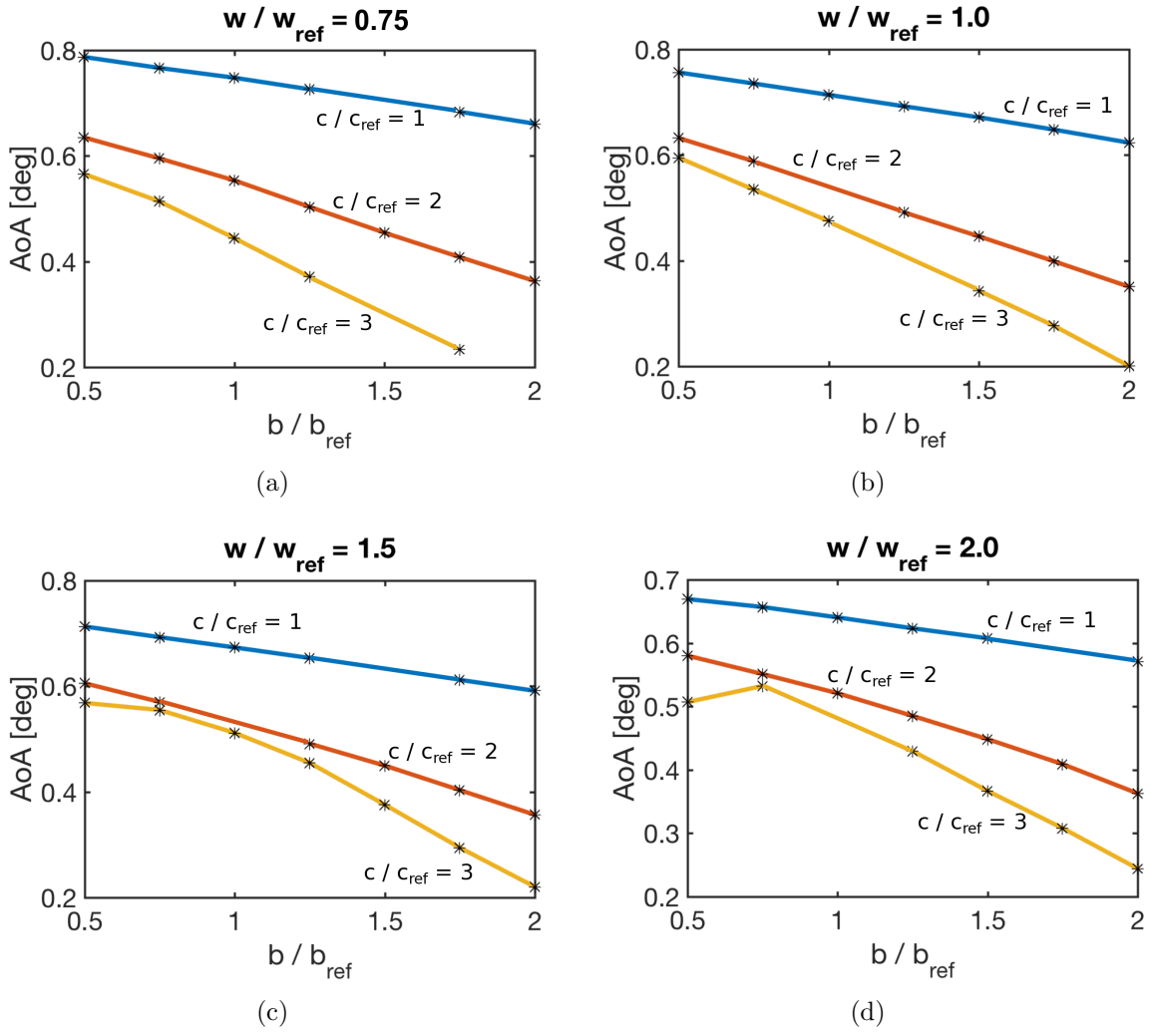

Figure C.4: Accelerating case ($\mathbf{a} = 1$): Angle of attack α for a trimmed MAX-1 waverider at Mach 8 and $q_\infty = 90$ kPa computed using MASIV. Effect of varying root chord (c), aspect ratio (b/c), engine width (W_e).

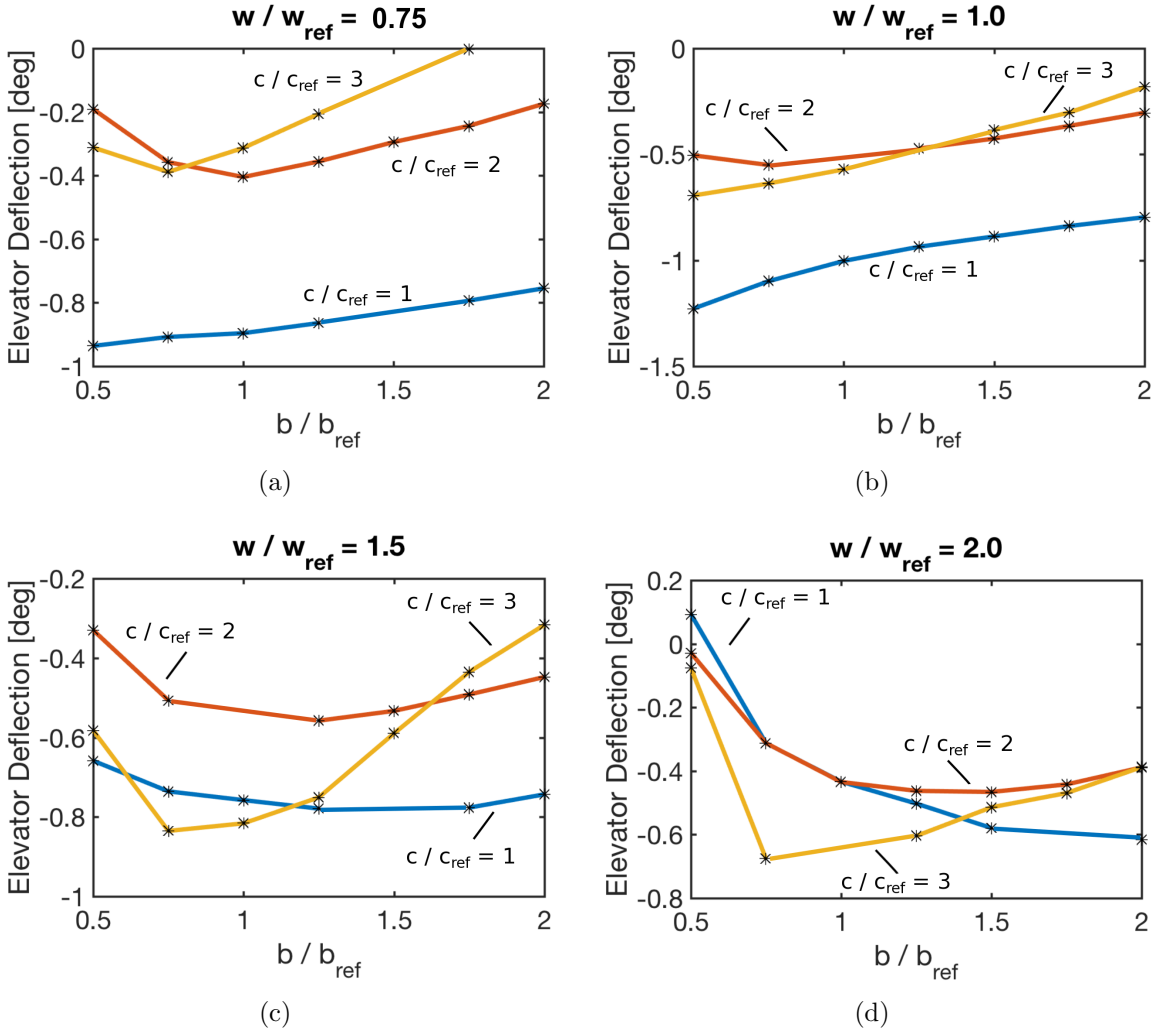

Figure C.5: Accelerating case ($\mathbf{a} = 1$): Elevon deflection δ for a trimmed MAX-1 waverider at Mach 8 and $q_\infty = 90$ kPa computed using MASIV. Effect of varying root chord (c), aspect ratio (b/c), engine width (W_e).

Computed T/D values for Cruise (zero acceleration)

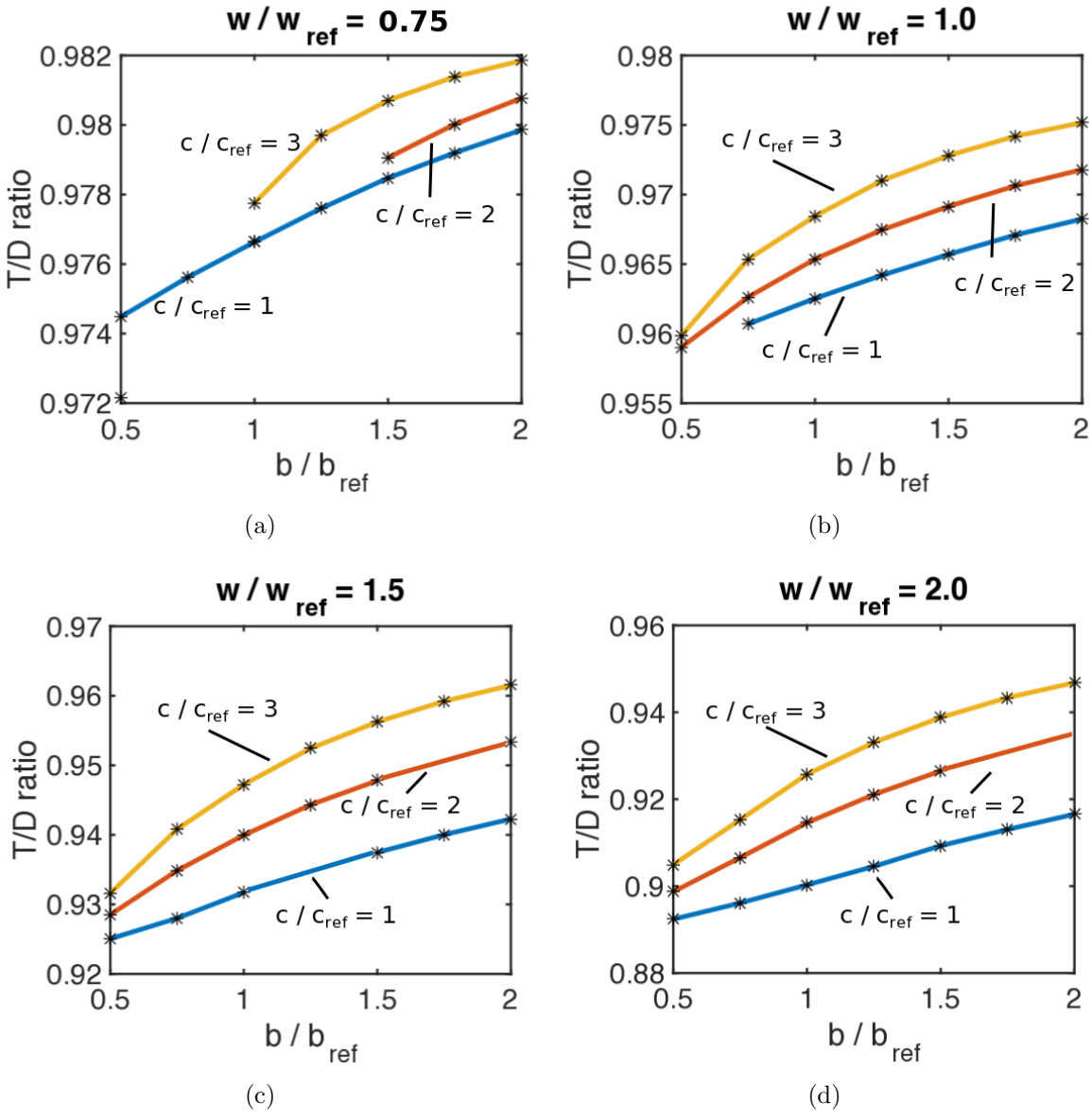

Figure C.6: Cruise case ($\mathbf{a} = 0$): T/D ratio for a trimmed MAX-1 waverider at Mach 8 and 26 km altitude computed using MASIV. Effect of varying root chord (c), aspect ratio (b/c), engine width (W_e).

Computed Angle of attack α and Elevon deflection angle δ Values for $\mathbf{a} = 2\ \mathbf{m/s^2}$

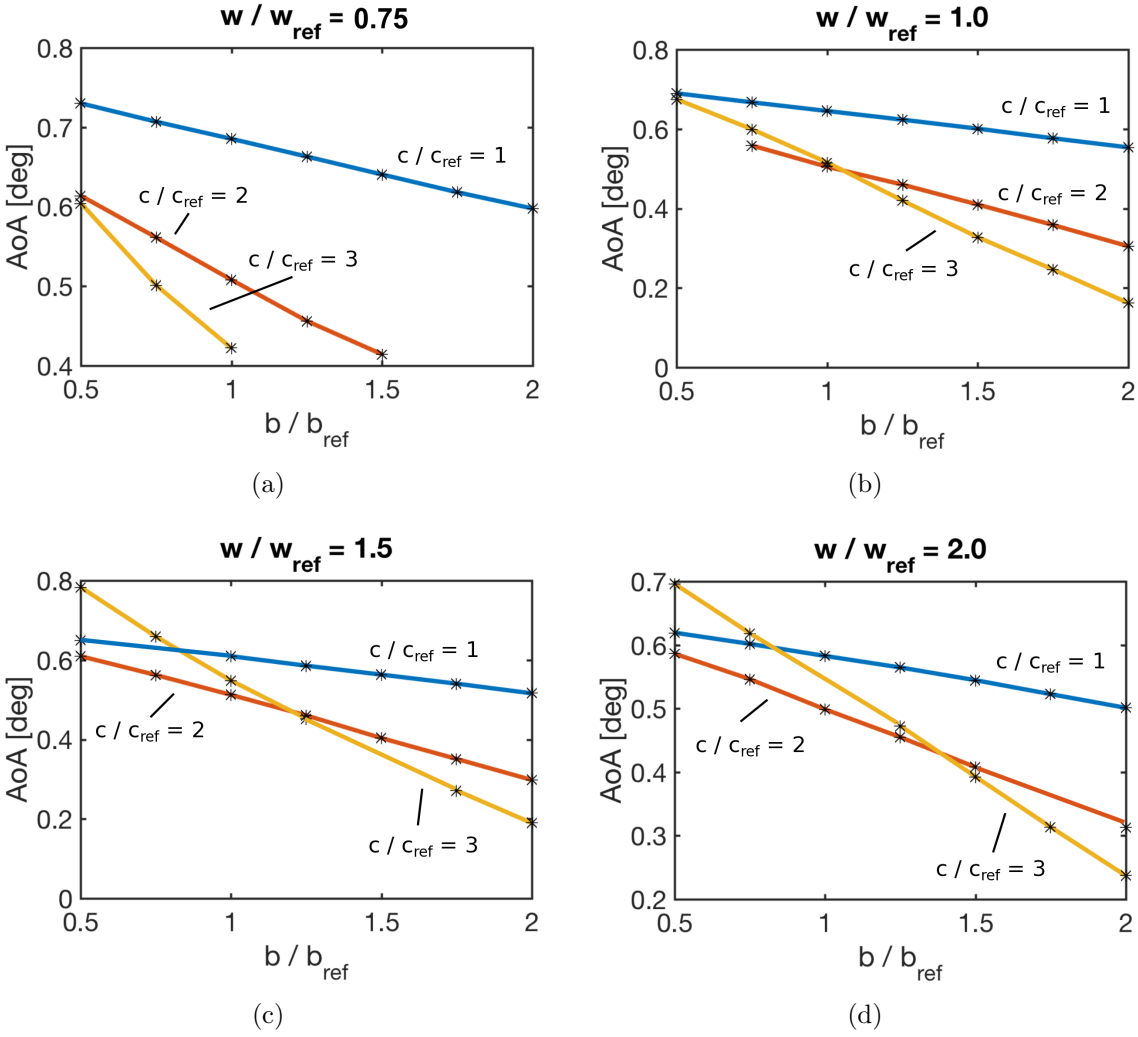

Figure C.7: Accelerating case ($\mathbf{a} = 2$): Angle of attack α for a trimmed MAX-1 waverider at Mach 8 and $q_\infty = 90$ kPa computed using MASIV. Effect of varying root chord (c), aspect ratio (b/c), engine width (W_e).

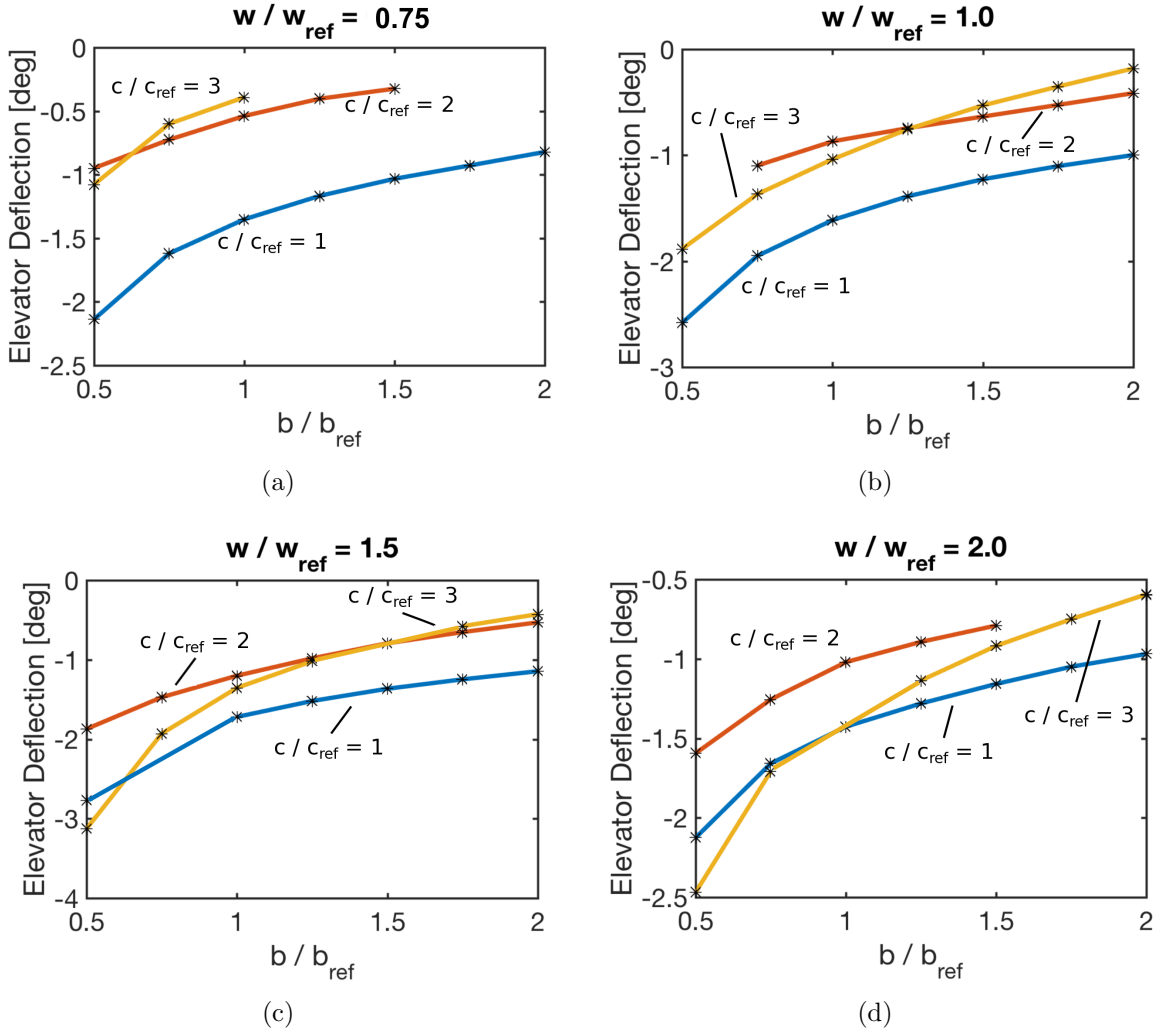

Figure C.8: Accelerating case ($\mathbf{a} = 2$): Elevon deflection δ for a trimmed MAX-1 waverider at Mach 8 and $q_\infty = 90$ kPa computed using MASIV. Effect of varying root chord (c), aspect ratio (b/c), engine width (W_e).

APPENDIX D

Trajectory Operating Maps for q_∞ = 70, 100, and 140 kPa

Constant q_∞ = 70 kPa Operating Maps

Constant q_∞ = 100 kPa Operating Maps

Constant q_∞ = 140 kPa Operating Maps

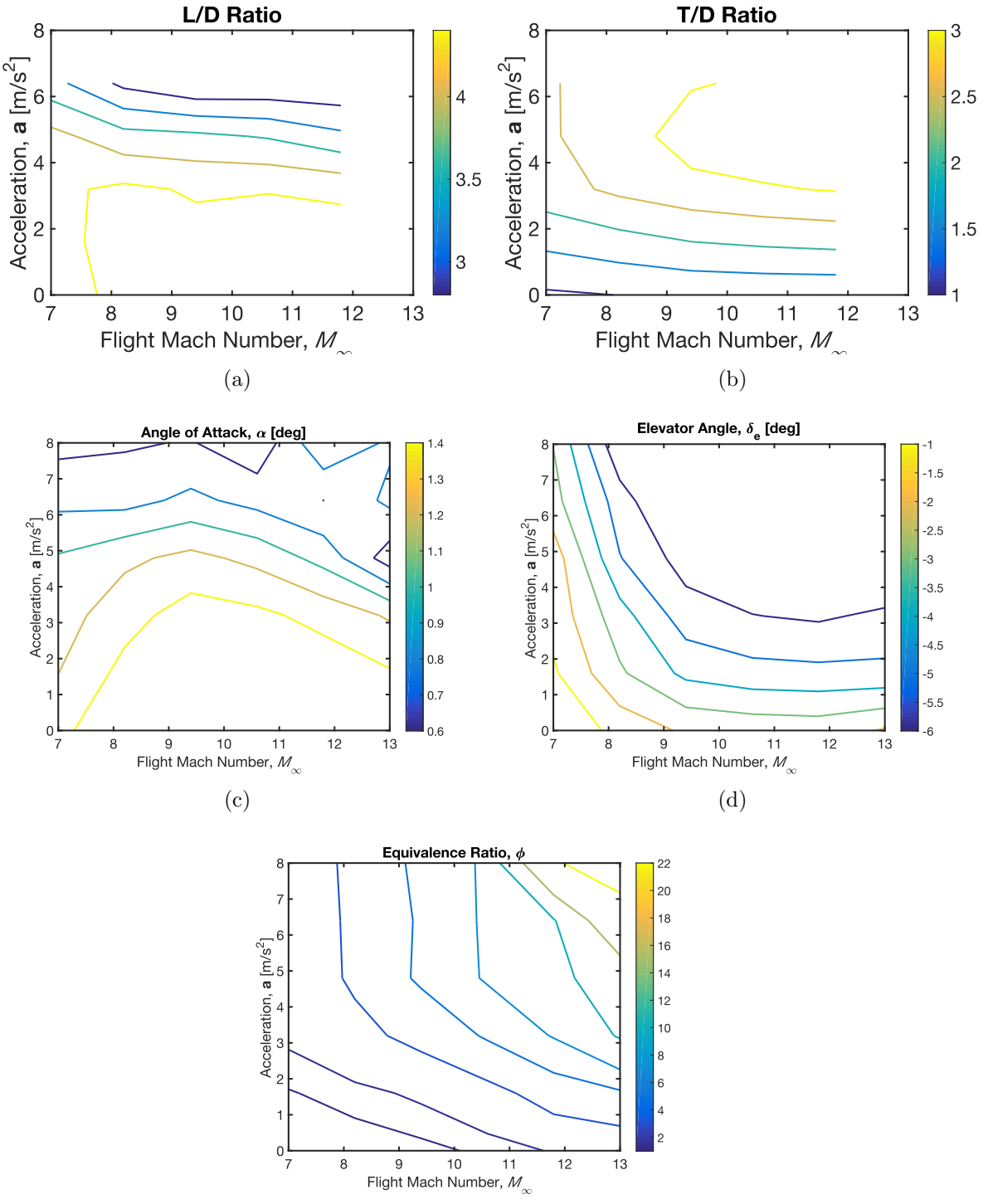

Figure D.1: Ascent trajectory and MAX-1 vehicle geometry; showing (a) T/D ratio, (b) L/D ratio, (c) angle of attack α, (d) elevon deflection angle δ, and (e) equivalence ratio ϕ. (Ascent is for constant dynamic pressure of 70 kPa and accelerations from zero to 8 m/s^2).

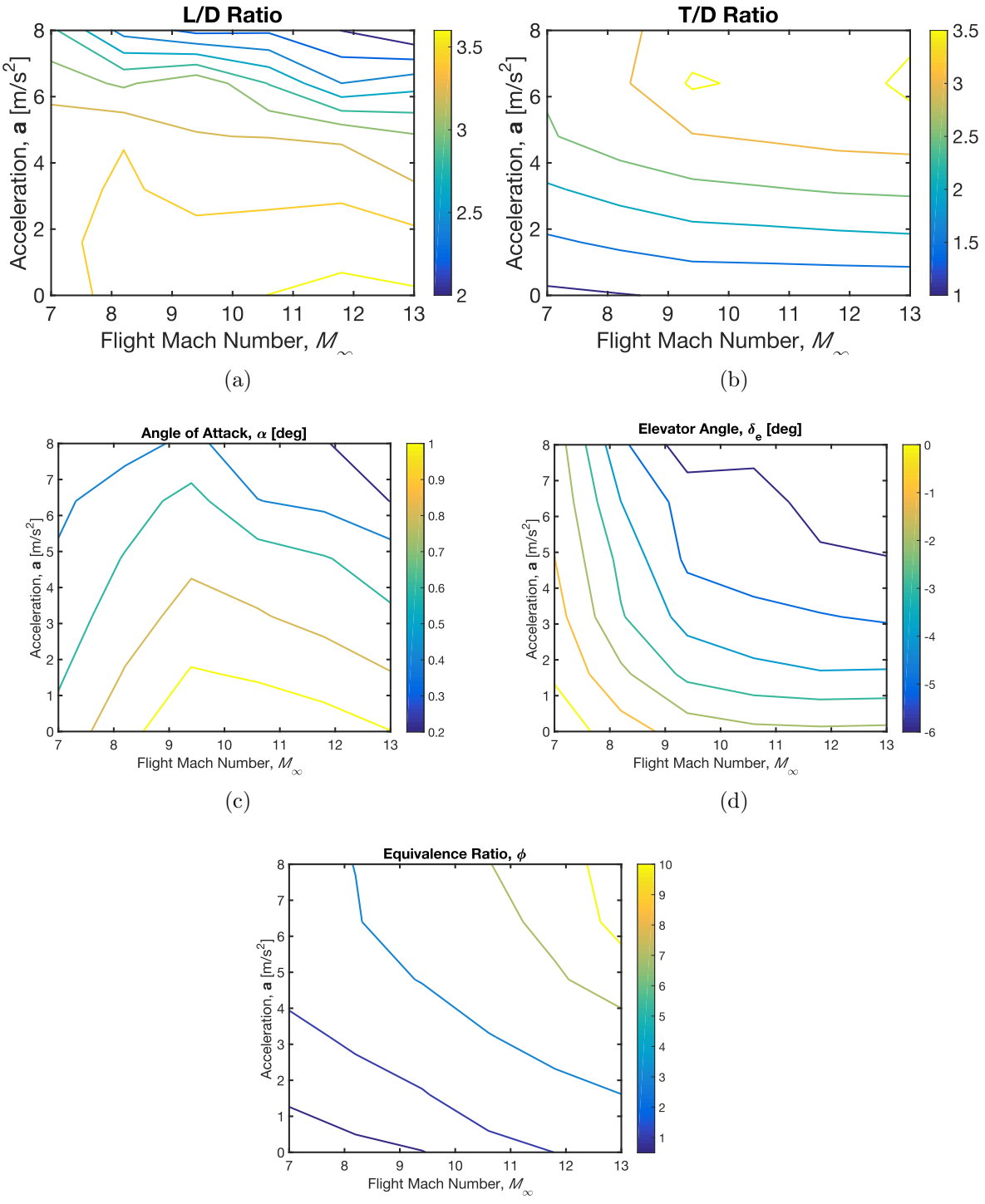

Figure D.2: Ascent trajectory and MAX-1 vehicle geometry; showing (a) T/D ratio, (b) L/D ratio, (c) angle of attack α, (d) elevon deflection angle δ, and (e) equivalence ratio ϕ. (Ascent is for constant dynamic pressure of 100 kPa and accelerations from zero to 8 m/s^2).

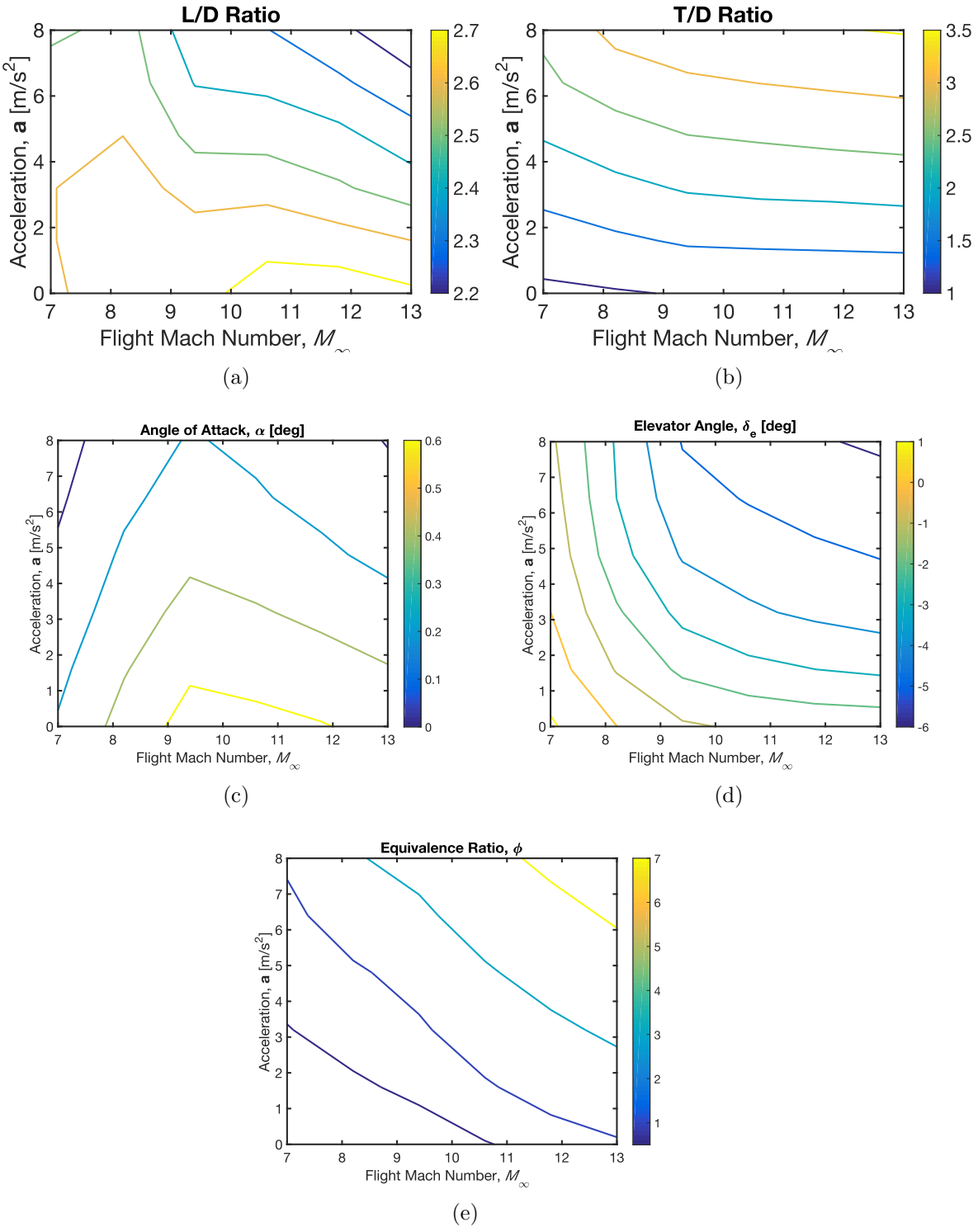

Figure D.3: Ascent trajectory and MAX-1 vehicle geometry; showing (a) T/D ratio, (b) L/D ratio, (c) angle of attack α, (d) elevon deflection angle δ, and (e) equivalence ratio ϕ. (Ascent is for constant dynamic pressure of 140 kPa and accelerations from zero to 8 m/s^2).

BIBLIOGRAPHY

BIBLIOGRAPHY

[1] D. J. Dalle, J. F. Driscoll, S. M. Torrez, Ascent Trajectories of Hypersonic Aircraft: Operability Limits Due to Engine Unstart, Journal of Aircraft 52 (4) (2015) 1–10. doi:10.2514/1.C032801.
URL http://arc.aiaa.org/doi/abs/10.2514/1.C032801 v, 2, 3, 4, 23, 24, 25, 56, 57, 58

[2] D. J. Dalle, M. L. Fotia, J. F. Driscoll, Reduced-Order Modeling of Two-Dimensional Supersonic Flows with Applications to Scramjet Inlets, Journal of Propulsion and Power 26 (3) (2010) 545–555. doi:10.2514/1.46521.
URL http://arc.aiaa.org/doi/abs/10.2514/1.46521 v, 24, 51, 57, 67

[3] S. M. Torrez, J. F. Driscoll, M. Ihme, M. L. Fotia, Reduced-Order Modeling of Turbulent Reacting Flows with Application to Ramjets and Scramjets, Journal of Propulsion and Power 27 (2) (2011) 371–382. doi:10.2514/1.50272.
URL http://arc.aiaa.org/doi/abs/10.2514/1.50272 v, x, 2, 3, 4, 16, 23, 24, 30, 33, 34, 52, 57, 58

[4] E. F. Hasselbrink, M. G. Mungal, Transverse jets and jet flames. Part 1. Scaling laws for strong transverse jets, Journal of Fluid Mechanics 443 (2001) 1–25. doi:10.1017/S0022112001005146. v, 2, 30

[5] J. A. Penland, J. L. Dillon, J. L. Pittman, An Aerodynamic Analysis of Several Hypersonic Research Airplane Concepts from M= 0.2 to 6.0, Journal of Aircraft 15 (11) (1978) 716–723. doi:10.2514/3.58437.
URL http://arc.aiaa.org/doi/10.2514/3.58437 vi, 60

[6] K. G. Bowcutt, J. D. Anderson, D. Capriotti, Viscous optimized hypersonic waveriders, 25th AIAA Aerospace Sciences Meeting (1987) 1987doi:10.2514/6.1987-272.
URL http://arc.aiaa.org/doi/abs/10.2514/6.1987-272 vi, 61, 72

[7] D. E. Fetterman, A. Henderson, M. E. Bertram, P. J. Johnston, Studies Relating to The Attainment of High Lift-Drag Ratios at Hypersonic Speeds, NASA Technical Note D-2956. vi, 63

[8] M. a. Bolender, D. B. Doman, Nonlinear Longitudinal Dynamical Model of an Air-Breathing Hypersonic Vehicle, Journal of Spacecraft and Rockets 44 (2) (2007) 374–387. doi:10.2514/1.23370. 2, 3, 55, 57, 113, 114

[9] M. K. L. O'Neill, M. J. Lewis, Design tradeoffs on scramjet engine integrated hypersonic waverider vehicles, Journal of Aircraft 30 (6) (1993) 943–952. doi:10.2514/3.46438. 2, 4, 58

[10] T. F. O', Brien, R. P. Starkey, M. J. Lewis, Quasi-One-Dimensional High-Speed Engine Model with Finite-Rate Chemistry, Journal of Propulsion and Power 17 (6) (2001) 1366–1374. doi:10.2514/2.5889.
URL http://arc.aiaa.org/doi/abs/10.2514/2.5889 2, 58

[11] K. G. Bowcutt, Multidisciplinary Optimization of Airbreathing Hypersonic Vehicles, Journal of Propulsion and Power 17 (6) (2001) 1184–1190. doi:10.2514/2.5893. 2, 55, 56, 72

[12] D. J. Dalle, S. M. Torrez, J. F. Driscoll, M. a. Bolender, K. G. Bowcutt, Minimum-Fuel Ascent of a Hypersonic Vehicle Using Surrogate Optimization, Journal of Aircraft (2014) 1–14doi:10.2514/1.C032617.
URL http://arc.aiaa.org/doi/abs/10.2514/1.C032617 2, 3, 4, 23, 24, 56, 57, 68, 72, 93

[13] S. M. Torrez, D. J. Dalle, J. F. Driscoll, New Method for Computing Performance of Choked Reacting Flows and Ram-to-Scram Transition, Journal of Propulsion and Power 29 (2) (2013) 433–445. doi:10.2514/1.B34496.

URL http://arc.aiaa.org/doi/abs/10.2514/1.B34496 32, 52, 58

[14] C. Mbagwu, J. F. Driscoll, An Approach to Computing the Combustion Efficiency of a Scramjet-Powered Hypersonic Vehicle, in: 20th AIAA International Space Planes and Hypersonic Systems and Technologies Conference, no. July, American Institute of Aeronautics and Astronautics, Reston, Virginia, 2015. doi:10.2514/6.2015-3506.
URL http://arc.aiaa.org/doi/10.2514/6.2015-3506 41, 51

[15] N. Lamorte, P. P. Friedmann, D. J. Dalle, S. M. Torrez, J. F. Driscoll, Uncertainty Propagation in Integrated AirframePropulsion System Analysis for Hypersonic Vehicles, Journal of Propulsion and Power 31 (1) (2015) 54–68. doi:10.2514/1.B35122.
URL http://arc.aiaa.org/doi/pdf/10.2514/6.2011-2394http://arc.aiaa.org/doi/abs/10.2514/1.B35122 51

[16] C. Mbagwu, J. F. Driscoll, A Method to Compute Flameout Limits of Scramjet-Powered Hypersonic Vehicles, in: 51st AIAA/SAE/ASEE Joint Propulsion Conference, American Institute of Aeronautics and Astronautics, Reston, Virginia, 2015. doi:10.2514/6.2015-3749.
URL http://arc.aiaa.org/doi/10.2514/6.2015-3749 39

[17] C. Mbagwu, J. F. Driscoll, Flameout and Combustion Efficiency of Scramjet-Powered Hypersonic Vehicles During Ascent, in: 54th AIAA Aerospace Sciences Meeting, no. January, American Institute of Aeronautics and Astronautics, Reston, Virginia, 2016. doi:10.2514/6.2016-0914.
URL http://arc.aiaa.org/doi/10.2514/6.2016-0914 2, 4, 23, 24, 57, 58

[18] F. R. Chavez, D. K. Schmidt, Analytical aeropropulsive-aeroelastic hypersonic-vehicle model with dynamic analysis, Journal of Guidance, Control, and Dynamics 17 (6) (1994) 1308–1319. doi:10.2514/3.21349. 2

[19] C. Mbagwu, J. F. Driscoll, D. J. Dalle, S. M. Torrez, Combustion Efficiencies and Flameout Limits Computed for a Hypersonic Vehicle During Ascent, Journal of Propulsion and Power. 6, 57

[20] M. Ihme, Artificial Neural Network Architectures for Application to Chemical Systems: Comparison of Generalized Pattern Search Method and Evolutionary Algorithm, Ann Arbor.
URL http://cdn.intechweb.org/pdfs/14906.pdf 8, 10, 11

[21] a. Fiszelew, P. Britos, a. Ochoa, H. Merlino, E. Fernandez, R. Garcia-Martinez, Finding Optimal Neural Network Architecture Using Genetic Algorithms, Advances in Computer Science and Engineering Research in Computer Science 27 (2007) 15–24.
URL http://www.iidia.com.ar/rgm/articulos/RCSJ-27-15-24.pdf 10

[22] J. L. Lumley, The Strucure of Inhomogeneous Turbulent Flows, Atmospheric Turbulence and Radio Wave Propagation (1967) 166–178. 14

[23] G. Berkooz, P. Holmes, J. L. Lumley, The Proper Orthogonal Decomposition in the Analysis of Turbulent Flows, Annual Review of Fluid Mechanics 25 (1) (1993) 539–575. doi:10.1146/annurev.fl.25.010193.002543.
URL http://www.annualreviews.org/doi/pdf/10.1146/annurev.fl.25.010193.002543

[24] A. C. Poje, J. L. Lumley, A model for large-scale structures in turbulent shear flows, Journal of Fluid Mechanics 285 (-1) (1995) 349. doi:10.1017/S0022112095000577.
URL http://www.journals.cambridge.org/abstract{_}S0022112095000577 14

[25] K. Tang, W. Graham, J. Peraire, Active flow control using a reduced order model and optimum control, AIAA paper (June). doi:10.2514/6.1996-1946.
URL http://arc.aiaa.org/doi/pdf/10.2514/6.1996-1946 14

[26] M. Romanowski, Reduced order unsteady aerodynamic and aeroelastic models using Karhunen-Loeve eigenmodes, AIAA paper

(1996) 7–13.
URL http://arc.aiaa.org/doi/pdf/10.2514/6.1996-3981 14

[27] T. Kim, M. Hong, K. G. Bhatia, G. Sengupta, Aeroelastic Model Reduction for Affordable Computational Fluid Dynamics-Based Flutter Analysis, AIAA Journal 43 (12) (2005) 2487–2495. doi:10.2514/1.11246. 14

[28] D. J. Lucia, P. S. Beran, W. a. Silva, Aeroelastic System Development Using Proper Orthogonal Decomposition and Volterra Theory, Journal of Aircraft 42 (2) (2005) 509–518. doi:10.2514/1.2176. 14

[29] P. Beran, C. Pettit, Prediction of nonlinear panel response using proper orthogonal decomposition, AIAA paper (c).
URL http://arc.aiaa.org/doi/pdf/10.2514/6.2001-1292 14

[30] J. P. Thomas, E. H. Dowell, K. C. Hall, Three-Dimensional Transonic Aeroelasticity Using Proper Orthogonal Decomposition-Based Reduced-Order Models, Journal of Aircraft 40 (3) (2003) 544–551. doi:10.2514/2.3128. 14

[31] Y. Cao, J. Zhu, I. M. Navon, Z. Luo, A reduced-order approach to four-dimensional variational data assimilation using proper orthogonal decomposition, International Journal for Numerical Methods in Fluids 53 (10) (2007) 1571–1583. doi:10.1002/fld.1365.
URL http://onlinelibrary.wiley.com/doi/10.1002/fld.1365/abstracthttp://doi.wiley.com/10.1002/fld.1365 14, 18, 38

[32] K. C. Hall, J. P. Thomas, E. H. Dowell, Proper orthogonal decomposition technique for transonic unsteady aerodynamic flows, AIAA Journal 38 (10) (2000) 1853–1862. doi:10.2514/3.14622.
URL http://arc.aiaa.org/doi/pdf/10.2514/2.867 16

[33] M. Rathinam, L. R. Petzold, A New Look at Proper Orthogonal Decomposition, SIAM Journal on Numerical Analysis 41 (5) (2003) 1893–1925. doi:10.1137/S0036142901389049.
URL http://epubs.siam.org.proxy.lib.umich.edu/doi/abs/10.1137/S0036142901389049 16, 18, 38

[34] D. C. Lay, Linear Algebra and its applications, 2nd Edition, Addison Wesley Longman, Inc, 2000. 17

[35] W. Heiser, D. Pratt, D. Daley, U. Mehta, Hypersonic Airbreathing Propulsion, American Institute of Aeronautics and Astronautics, Inc., Washington, DC, 1994. doi:10.2514/4.470356.
URL http://arc.aiaa.org/doi/book/10.2514/4.470356 26, 27, 36, 41, 58, 64, 67, 68

[36] M. R. BAXTER, A. H. LEFEBVRE, Flame stabilization in high-velocity heterogeneous fuel-air mixtures (nov 1992). doi:10.2514/3.11454.
URL http://arc.aiaa.org/doi/abs/10.2514/3.11454

[37] J. F. Driscoll, C. C. Rasmussen, Correlation and Analysis of Blowout Limits of Flames in High-Speed Airflows, Journal of Propulsion and Power 21 (6) (2005) 1035–1044. doi:10.2514/1.13329.
URL http://arc.aiaa.org/doi/abs/10.2514/1.13329 27, 49, 52

[38] R. I. Ozawa, Survey of Basic Data on Flame Stabilization and Propagation for High Speed Combustion Systems, The Marquart Co., TR AFAPL-TR-70-81. 27

[39] S. J. Shanbhogue, S. Husain, T. Lieuwen, Lean blowoff of bluff body stabilized flames: Scaling and dynamics, Progress in Energy and Combustion Science 35 (1) (2009) 98–120. doi:10.1016/j.pecs.2008.07.003.
URL http://dx.doi.org/10.1016/j.pecs.2008.07.003 27

[40] G. T. Kalghatgi, Blow-Out Stability of Gaseous Jet Diffusion Flames. Part I: In Still Air, Combustion Science and Technology 26 (5-6) (1981) 233–239. doi:10.1080/00102208108946964.
URL http://www.tandfonline.com/doi/abs/10.1080/00102208108946964 27

[41] S. Takahashi, N. Sato, M. Tsue, M. Kono, M. Nakamura, H. Kondo, Y. Ujiie, Control of Flame-Holding in Supersonic Air-

flow by Secondary Air Injection, Journal of Propulsion and Power 14 (1) (1998) 18–23. doi:10.2514/2.5260. 27, 28, 29, 37

[42] M.-b. Sun, H. Geng, J.-h. Liang, Z.-g. Wang, Flame Characteristics in Supersonic Combustor with Hydrogen Injection Upstream of Cavity Flameholder, Journal of Propulsion and Power 24 (4) (2008) 688–696. doi:10.2514/1.34970.
URL http://arc.aiaa.org/doi/abs/10.2514/1.34970 28, 29

[43] D. J. Micka, J. F. Driscoll, Stratified jet flames in a heated (1390K) air cross-flow with autoignition, Combustion and Flame 159 (3) (2012) 1205–1214. doi:10.1016/j.combustflame.2011.10.013.
URL http://linkinghub.elsevier.com/retrieve/pii/S001021801100318X 28, 29

[44] S. H. Kang, Y. J. Lee, S. S. Yang, M. K. Smart, M. K. Suraweera, Cowl and Cavity Effects on Mixing and Combustion in Scramjet Engines, Journal of Propulsion and Power 27 (6) (2011) 1169–1177. doi:10.2514/1.48818.
URL http://arc.aiaa.org/doi/abs/10.2514/1.48818 28, 29

[45] G. Retaureau, S. Menon, Experimental Studies on Flame Stability of a Fueled Cavity in a Supersonic Crossflow, in: 46th AIAA/ASME/SAE/ASEE Joint Propulsion Conference & Exhibit, no. 46, American Institute of Aeronautics and Astronautics, Reston, Virigina, 2010, pp. 25–28. doi:10.2514/6.2010-6718.
URL http://arc.aiaa.org/doi/abs/10.2514/6.2010-6718 27, 28, 29

[46] M. R. Gruber, J. M. Donbar, C. D. Carter, K.-Y. Hsu, Mixing and Combustion Studies Using Cavity-Based Flameholders in a Supersonic Flow, Journal of Propulsion and Power 20 (5) (2004) 769–778. doi:10.2514/1.5360.

[47] C. C. Rasmussen, J. F. Driscoll, Characteristics of Cavity- Stabilized Flames in a Supersonic Flow, Journal of Propulsion and Power 21 (2) (2005) 765–768. doi:10.2514/1.40131.

[48] C. C. Rasmussen, J. F. Driscoll, K. Y. Hsu, J. M. Donbar, M. R. Gruber, C. D. Carter, Stability limits of cavity-stabilized flames

in supersonic flow, Proceedings of the Combustion Institute 30 II (2) (2005) 2825–2833. doi:10.1016/j.proci.2004.08.185.
URL http://linkinghub.elsevier.com/retrieve/pii/S0082078404002371

[49] C. C. Rasmussen, S. K. Dhanuka, J. F. Driscoll, Visualization of flameholding mechanisms in a supersonic combustor using PLIF, Proceedings of the Combustion Institute 31 (2) (2007) 2505–2512. doi:10.1016/j.proci.2006.08.007.
URL http://linkinghub.elsevier.com/retrieve/pii/S1540748906002707

[50] B. J. Tatman, R. D. Rockwell, C. P. Goyne, J. C. McDaniel, J. M. Donohue, Experimental Study of Vitiation Effects on Flameholding in a Cavity Flameholder, Journal of Propulsion and Power 29 (2) (2013) 417–423. doi:10.2514/1.B34687.
URL http://arc.aiaa.org/doi/abs/10.2514/1.B34687 28

[51] E. F. Hasselbrink, M. G. Mungal, Transverse jets and jet flames. Part 2. Velocity and OH field imaging (2001). doi:10.1017/S0022112001005158.
URL http://journals.cambridge.org/download.php?file=/FLM/FLM443/S0022112001005158a.pdf{&}code=c113e3eea2f7fbbf1d84a553e6b92ef1 30, 31, 33, 51

[52] S. H. Smith, M. G. Mungal, Mixing, structure and scaling of the jet in crossflow, Journal of Fluid Mechanics 357 (1998) 83–122. doi:10.1017/S0022112097007891.
URL http://journals.cambridge.org/abstract{_}S0022112097007891 30, 31, 33, 34, 51, 52

[53] K.-C. Lin, M. Ryan, C. Carter, M. Gruber, C. Raffoul, Raman Scattering Measurements of Gaseous Ethylene Jets in a Mach 2 Supersonic Crossflow, Journal of Propulsion and Power 26 (3) (2010) 503–513. doi:10.2514/1.43757. 32

[54] M. Ihme, Y. C. See, Prediction of autoignition in a lifted methane/air flame using an unsteady flamelet/progress variable model, Combustion and Flame 157 (10) (2010) 1850–1862.

doi:10.1016/j.combustflame.2010.07.015.
URL http://dx.doi.org/10.1016/j.combustflame.2010.07.015http://linkinghub.elsevier.com/retrieve/pii/S0010218010002038 33

[55] N. Peters, Laminar diffusion flamelet models in non-premixed turbulent combustion, Progress in Energy and Combustion Science 10 (3) (1984) 319–339. arXiv:arXiv:1011.1669v3, doi:10.1016/0360-1285(84)90114-X. 33

[56] H. Pitsch, FLAMEMASTER V3.1: a C++ computer program for 0D combustion and 1D laminar flame calculations. <http://www.stanford.edu/group/pitsch/> (1998). 33

[57] C. J. Jachimowski, An Analytical Study of the Hydrogen-Air Reaction Mechanism with Application to Scramjet Combustion, NASA TP-2791. 33, 38

[58] D. Allison, C. Morris, J. Schetz, R. Kapania, C. Sultan, J. Deaton, R. Grandhi, A Multidisciplinary Design Optimization Framework for Design Studies of an Efficient Supersonic Air Vehicle, in: 12th AIAA Aviation Technology, Integration, and Operations (ATIO) Conference and 14th AIAA/ISSMO Multidisciplinary Analysis and Optimization Conference, no. September, American Institute of Aeronautics and Astronautics, Reston, Virigina, 2012, pp. 1–22. doi:10.2514/6.2012-5492.
URL http://arc.aiaa.org/doi/abs/10.2514/6.2012-5492 51

[59] J. A. C. Falcão de Campos, P. J. A. Ferreira de Sousa, J. Bosschers, A verification study on low-order three-dimensional potential-based panel codes, Computers and Fluids 35 (1) (2006) 61–73. doi:10.1016/j.compfluid.2004.08.002.
URL http://linkinghub.elsevier.com/retrieve/pii/S0045793004001197 51

[60] K. Bowcutt, G. Kuruvila, T. Grandine, E. Cramer, Advancements in Multidisciplinary Design Optimization Applied to Hypersonic Vehicles to Achieve Performance Closure, in: 15th AIAA

International Space Planes and Hypersonic Systems and Technologies Conference, no. May, American Institute of Aeronautics and Astronautics, Reston, Virigina, 2008, pp. 1–12. doi:10.2514/6.2008-2591.
URL http://arc.aiaa.org/doi/10.2514/6.2008-2591 55, 56, 72

[61] K. G. Bowcutt, Hypersonic Gliders and Air-Breathing Vehicles: Vehicle Design and Flight Testing Challenges and Requirements, NATO / OTAN report STO-AVT-234.

[62] T. R. Smith, K. G. Bowcutt, J. R. Selmon, L. Miranda, B. Northrop, R. Mairs, R. Unger, T. B. Company, H. Beach, K. Y. Lau, T. Silvester, H. Alesi, A. Paull, R. Paull, D. Science, D. J. Dolvin, T. Hypersonic, I. Flight, A. D. Science, A. T. Fellow, P. P. Technology, S. T. Fellow, V. Management, S. Technology, T. Fellow, F. Controls, S. A. Engineer, A. H. Branch, A. V. Division, P. A. Engineer, P. S. Engineer, HIFiRE 4: A Low-Cost Aerodynamics, Stability, and Control Hypersonic Flight Experiment, AIAA International Space Planes and Hypersonic Systems and Technologies Conference (April) (2011) 1–32. arXiv:9809069v1, doi:10.2514/6.2011-2275.

[63] D. W. Riggins, J. A. Camberos, M. Wolff, K. Bowcutt, Mission-Integrated Exergy Analysis for Hypersonic Vehicles: Methodology and Application, Journal of Propulsion and Power 29 (3) (2013) 610–620. doi:10.2514/1.B34733. 55, 56, 72

[64] J. T. Parker, A. Serrani, S. Yurkovich, M. a. Bolender, D. B. Doman, Control-Oriented Modeling of an Air-Breathing Hypersonic Vehicle, Journal of Guidance, Control, and Dynamics 30 (3) (2007) 856–869. doi:10.2514/1.27830. 55

[65] T. Vick, J. Muse, M. A. Bolender, A Hypersonic Vehicle Model Generator for MASIV, AIAA Modeling and Simulation Technologies Conference (August) (2012) 1–39. doi:doi:10.2514/6.2012-4563.
URL http://dx.doi.org/10.2514/6.2012-4563

[66] T. Skujins, C. E. Cesnik, M. W. Oppenheimer, D. B. Doman, Canard-Elevon Interactions on a Hypersonic Vehicle, Journal of Spacecraft and Rockets 47 (1) (2010) 90–100. doi:10.2514/1.44743. 56

[67] D. J. Dalle, M. a. Bolender, S. M. Torrez, J. F. Driscoll, Flight Envelope Calculation of a Hypersonic Vehicle Using a First Principles-Derived Model, 17th AIAA International Space Planes and Hypersonic Systems and Technologies Conference (April) (2011) 1–22. doi:10.2514/6.2011-2368. 57

[68] D. J. Dalle, S. M. Torrez, J. F. Driscoll, Rapid Analysis of Scramjet and Linear Plug Nozzles, Journal of Propulsion and Power 28 (3) (2012) 545–555. doi:10.2514/1.B34391.

[69] D. Dalle, S. Torrez, J. Driscoll, Sensitivity of Flight Dynamics of Hypersonic Vehicles to Design Parameters, in: 18th AIAA/3AF International Space Planes and Hypersonic Systems and Technologies Conference, no. September, American Institute of Aeronautics and Astronautics, Reston, Virigina, 2012, pp. 1–20. doi:10.2514/6.2012-5909.
URL http://dx.doi.org/10.2514/6.2012-5909http://arc.aiaa.org/doi/10.2514/6.2012-5909 57

[70] R. P. Starkey, M. J. Lewis, Critical Design Issues for Airbreathing Hypersonic Waverider Missiles, Journal of Spacecraft and Rockets 38 (4) (2001) 510–519. doi:10.2514/2.3734. 58

[71] R. Starkey, F. Rankins, D. Pines, Coupled Waverider/Trajectory Optimization for Hypersonic Cruise, in: 43rd AIAA Aerospace Sciences Meeting and Exhibit, no. January, American Institute of Aeronautics and Astronautics, Reston, Virigina, 2005, pp. 7345–7360. doi:10.2514/6.2005-530.
URL http://arc.aiaa.org/doi/10.2514/6.2005-530

[72] R. P. Starkey, Off-Design Performance Characterization of a Variable Geometry Scramjet, 41st AIAA/ASME/SAE/ASEE Joint Propulsion Conference & Exhibit (July) (2005) 1–12. doi:10.

2514/6.2005-3711.
URL http://arc.aiaa.org/doi/abs/10.2514/6.2005-3711

[73] R. P. Starkey, Design Sensitivities of Scramjets Using Finite Rate Chemistry, 42nd AIAA/ASME/SAE/ASEE Joint Propulsion Conference & Exhibit (July) (2006) 1–8. doi:doi:10.2514/6.2006-4612.

[74] M. K. L. O'Neill, M. J. Lewis, Optimized Scramjet Integration on a Waverider, Journal of Aircraft 29 (6) (1992) 1114–1121. doi:10.2514/3.56866.
URL http://doi.aiaa.org/10.2514/3.56866

[75] C. J. Doolan, Hypersonic Missile Performance and Sensitivity Analysis, Journal of Spacecraft and Rockets 44 (1) (2007) 81–87. doi:10.2514/1.23160.
URL http://arc.aiaa.org/doi/10.2514/1.23160

[76] J. Dickeson, A. Rodriguez, S. Sridharan, D. Soloway, A. Korad, J. Khatri, J. Benavides, A. Kelkar, J. Vogel, Control-Relevant Modeling, Analysis, and Design for Scramjet-Powered Hypersonic Vehicles, in: 16th AIAA/DLR/DGLR International Space Planes and Hypersonic Systems and Technologies Conference, American Institute of Aeronautics and Astronautics, Reston, Virigina, 2009, pp. 1–45. doi:10.2514/6.2009-7287.
URL http://arc.aiaa.org/doi/10.2514/6.2009-7287

[77] D. Akihisa, T. Kanda, K. Tani, K. Kudo, G. Masuya, Effect of Integration of Scramjet into Airframe on Engine Performance and Payload, Journal of Propulsion and Power 18 (5) (2002) 1026–1032. doi:10.2514/2.6051.

[78] H. IKAWA, Rapid methodology for design and performance prediction of integrated supersonic combustion ramjet engine, Journal of Propulsion and Power 7 (3) (1991) 437–444. doi:10.2514/3.23345.
URL http://dx.doi.org/10.2514/3.23345

[79] H. Li, P. Lin, D. Xu, Control-oriented modeling for air-breathing hypersonic vehicle using parameterized configuration approach,

Chinese Journal of Aeronautics 24 (1) (2011) 81–89. doi:10.1016/S1000-9361(11)60010-1.
URL http://dx.doi.org/10.1016/S1000-9361(11)60010-1

[80] J. Che, S. Tang, Research on integrated optimization design of hypersonic cruise vehicle, Aerospace Science and Technology 12 (7) (2008) 567–572. doi:10.1016/j.ast.2008.01.008.

[81] K. H. Javaid, V. C. Serghides, Thrust-Matching Requirements for the Conceptual Design of Hypersonic Waverider Vehicles, Journal of Aircraft 42 (4) (2005) 1055–1064. doi:10.2514/1.8729.
URL http://arc.aiaa.org/doi/10.2514/1.8729

[82] K. H. Javaid, V. C. Serghides, Airframe-Propulsion Integration Methodology for Waverider-Derived Hypersonic Cruise Aircraft Design Concepts, Journal of Spacecraft and Rockets 42 (4) (2005) 663–671. doi:10.2514/1.8782. 58

[83] F. S. BILLIG, Combustion processes in supersonic flow, Journal of Propulsion and Power 4 (3) (1988) 209–216. doi:10.2514/3.23050.
URL http://arc.aiaa.org/doi/10.2514/3.23050 58, 64, 68

[84] F. S. Billig, Research on supersonic combustion, Journal of Propulsion and Power 9 (4) (1993) 499–514. doi:10.2514/3.23652. 67, 68

[85] F. S. Billig, P. J. Waltrup, H. E. Gilreath, M. E. White, D. M. Van Wie, P. P. Pandolfini, Propulsion System Management Plan, Johns Hopkins University Report JHU/APL-NASP-86-1. 64, 68

[86] P. J. WALTRUP, F. S. BILLIG, M. C. EVANS, Critical considerations in the design of supersonic combustion ramjet /scramjet/ engines, Journal of Spacecraft and Rockets 18 (4) (1981) 350–356. doi:10.2514/3.28060.
URL http://arc.aiaa.org/doi/10.2514/3.28060

[87] P. Waltrup, F. Billig, R. Stockbridge, A Procedure for Optimizing the Design of Scrainjet Engines, Journal of Spacecraft and Rockets

16 (3) (1979) 163–171. doi:10.2514/3.57637.
URL http://arc.aiaa.org/doi/10.2514/3.57637 58

[88] J. D. Anderson, Modern Compressible Flow: with Historical Perspective, third edit Edition, McGraw-Hill, New York, NY, 1990. 60

[89] H. Schlichting, Aerodynamics of the Airplane, McGraw-Hill, New York, NY, 1979. 60

[90] F. M. White, Viscous Fluid Flow, third edit Edition, McGraw-Hill, New York, NY, 2006. 60

[91] D. Kuchemann, The aerodynamic design of aircraft, Progress in aeronautical sciences, Pergamon, London, 1978. 61

[92] P. G. Hill, C. R. Peterson, Mechanics and thermodynamics of propulsion, Addison-Wesley Publishing Co., Reading, MA, 1992. 66

[93] K. BOWCUTT, Hypersonic aircraft optimization including aerodynamic, propulsion, and trim effects, 4th Symposium on Multidisciplinary Analysis and Optimization (December). doi:10.2514/6.1992-5055.
URL http://arc.aiaa.org/doi/10.2514/6.1992-5055 72